이학박사학위논문

The QBO impacts on the MJO and its prediction

성층권 준 2 년주기진동이 매든-줄리안 진동에 미치는 영향

2020 년 2 월

서울대학교 대학원
지구환경과학부
임 유 나

The QBO impacts on the MJO and its prediction

성층권 준2년주기진동이
매든-줄리안 진동에 미치는 영향

지도교수 손 석 우

이 논문을 이학박사 학위논문으로 제출함

2020년 1월

서울대학교 대학원

지구환경과학부

임 유 나

임유나의 이학박사 학위논문을 인준함

2019년 12월

위 원 장 허 창 회 (인)

부위원장 손 석 우 (인)

위 원 서 경 환 (인)

위 원 유 창 현 (인)

위 원 김 혜 미 (인)

Abstract

Lim, Yu-Na
School of Earth Environmental Sciences
The Graduate School
Seoul National University

Recent studies have shown that the Quasi-Biennial Oscillation (QBO) affects the boreal winter Madden-Julian Oscillation (MJO). During the easterly phase of QBO (EQBO) winters, the MJO activity is amplified, and the opposite is shown during the westerly phase of QBO (WQBO) winters. Since this relationship is very recently reported with simple correlation analysis, it should be confirmed and understood in detail. This thesis is to investigate the QBO-MJO connection using a variety of datasets, such as the observations, dynamical core model, climate models, and subseasonal-to-seasonal (S2S) prediction models. Their possible mechanism(s) and the impacts on the MJO prediction are also evaluated and discussed.

In the observational study, it is shown that the overall MJO characteristics are closely linked with the stratospheric QBO. The MJO activity around the Maritime Continent becomes stronger and more organized during EQBO than during WQBO winters. The QBO-related MJO change explains up to 40% of the interannual variation of the boreal winter MJO amplitude. During EQBO winters, the MJO convections propagate further eastward with a slower propagation, and more enhanced MJO teleconnection

is also presented. These systematic changes in MJO activity confirm the QBO-MJO connection, emphasizing the stratospheric impact on the MJO.

Due to the short analysis period of the observational data, the model outputs are helpful for a better understanding of this phenomenon. In the climate models, however, a weak hint of the QBO-MJO link is found only in the medium-resolution Max Planck Institute Earth System Model (MPI-ESM-MR) among four CMIP5 models that internally generate the QBO. In this model, the MJO anomalies become slightly stronger and more organized during EQBO than during WQBO winters. Overall differences, however, are still much weaker and less organized than the observation. When daily MJO-index amplitude is compared, their differences are not robust. The reasons for weak QBO-MJO connection might result from the weak QBO and MJO amplitudes, and weak static stability change in response to the QBO in the model.

To better simulate the QBO structure and to examine the dynamical process, the QBO-MJO connection is tested in an idealized experiment using a dynamical core model. It is found that the QBO can directly change the MJO-related vertical structure. The MJO-induced cold anomaly near the tropopause becomes colder, especially over the western Pacific in the EQBO-like experiment, which promotes the MJO activity. This result seems to be related to the Doppler shift effect by the QBO-related zonal wind, suggesting the potential impact of the dynamical process on the QBO-MJO connection.

Considering both of dynamical and physical processes with a better QBO simulation, the capability of the QBO-MJO connection is evaluated in the S2S prediction models. Their relationship is also applied in the MJO prediction skill. Ten operational models participated in the S2S prediction project show a higher MJO prediction skill during EQBO winters than during WQBO winters, based on the QBO-MJO link. For the bivariate anomaly correlation coefficient of 0.5, the MJO prediction skill during EQBO winters is enhanced by up to 10 days. This enhancement is insensitive to the initial MJO amplitude, indicating that the improved MJO prediction skill is not simply the result of a stronger MJO. Instead, a longer persistence of the MJO during EQBO winters likely induces a higher prediction skill by having a higher prediction limit.

Even though the QBO modulates the MJO prediction skill, the QBO-MJO connection is not fully captured even in the S2S prediction models. To improve the simulation of the QBO-MJO connection in these models, the relationship of MJO prediction skill with model biases in the mean moisture fields and the longwave cloud–radiation feedbacks are investigated, based on understanding the MJO processes. In most models, a notable dry bias develops within a few days of forecast lead time in the deep tropics, especially across the Maritime Continent. The dry bias weakens the horizontal moisture gradient over the Indian Ocean and western Pacific, likely dampening the organization and propagation of the MJO. Most S2S models also

underestimate the longwave cloud–radiation feedbacks in the tropics, which may affect the maintenance of the MJO convective envelope. In the S2S prediction project, the operational models with smaller bias in the mean horizontal moisture gradient and the longwave cloud–radiation feedbacks show higher MJO prediction skills, suggesting that improving those biases would enhance MJO prediction skill and the simulation of the QBO-MJO connection.

Keywords: Quasi-Biennial Oscillation, Madden-Julian Oscillation, stratosphere-troposphere coupling, subseasonal-to-seasonal prediction

Student number: 2015-30111

Table of Contents

List of Tables

List of Figures

Chapter 1. Introduction

The Madden–Julian Oscillation (MJO) is a planetary scale, equatorially trapped convective disturbance that propagates eastward with a period of 30–60 days (e.g., Madden and Julian 1971, 1972; Zhang 2005). The MJO significantly modulates not only precipitation but also large-scale atmospheric circulation in the tropics (Zhang 2013). For example, MJO-related circulation anomalies affect the Indian and Australian monsoons, as well as the African monsoon (Yasunari 1979; Hendon and Liebmann 1990; Lavender and Matthews 2009). The MJO-related circulation anomalies also affect the genesis of tropical cyclones over all ocean basins (e.g., Hall et al. 2001).

The impact of the MJO is not limited to the tropics. The MJO's influence is also evident in the extratropics. The upper-level divergence, induced by the MJO-related large-scale vertical motion, often excites the Rossby wave packet that propagates into the subtropical North Pacific, western North America, and North Atlantic region (Matthews et al. 2004; Lin et al. 2009; Seo and Son 2012). Through this teleconnection, the MJO significantly modulates surface weather and climate systems in East Asia, North America, and Europe (Jeong et al. 2005; Cassou 2008).

Given its wide influence, a variety of mechanisms have been suggested to better simulate the MJO. It can be largely divided into convectively coupled Kelvin-Rossby wave theory, moisture mode theory, and

multiscale interaction theory. In the convectively coupled Kelvin-Rossby wave theory, the MJO activity is explained by the interaction between the convective heating, planetary-scale equatorial waves, and the boundary layer moisture convergence (Wang 1988; Wang and Li 1994; Kang et al. 2013; Wang and Chen 2017). Secondly, moisture mode theory is based on the tight coupling between moisture and convection and the smallness of buoyancy perturbations in the tropics (Charney 1963; Sobel et al. 2001), the evolution of large-scale, low-frequency convective anomalies associated with the MJO is explained by those of moisture anomalies (Neelin and Yu 1994; Sobel and Maloney 2012; 2013, Adames and Kim 2016). Lastly, the multiscale interaction theory is that the mesoscale and synoptic scale motions influence the MJO dynamics (Majda and Stechmann, 2009), considering the fact that the MJO convection consists of multiscale convective system (Nakazawa, 1988). In addition to these processes, the atmosphere-ocean interaction (Flatau et al. 1997; Wang and Xie 1998) and the cloud-radiation feedback (Kim et al. 2015) are also known as important MJO processes. These current MJO theories, however, mostly have focused on the tropospheric processes.

Based on these understanding, the MJO prediction skill in operational models has been extensively developed over the past decade. Among others, it has been reported that the MJO prediction skills of the National Centers for Environmental Prediction (NCEP) and the European Centre for Medium-Range Weather Forecasts (ECMWF) model are approximately 20 days (Wang

et al. 2014; Kim et al. 2014) and 31 days (Vitart et al. 2014), respectively. Rashid et al. (2011) documented that the MJO prediction skill of the Australian Bureau of Meteorology (BoM) model is approximately 21 days. The Japan Meteorological Agency (JMA) and China Meteorological Administration (CMA) coupled models, respectively, showed limits of approximately 25 days (Neena et al. 2014) and 16 days (Liu et al. 2017). Overall, these studies suggest that the MJO prediction skill in recent operational models is approximately 16 to 31 days.

Changing the point of view about the Quasi-Biennial Oscillation (QBO), the QBO is a phenomenon that equatorial stratospheric zonal winds alternate from easterlies to westerlies with a period of about 28 months, propagating downward into the lower stratosphere from 100 to 10 hPa (Baldwin et al. 2001). It has been known that the QBO can directly influence the tropical deep convection in the seasonal mean time scale. Firstly, the QBO-induced zonal wind changes in the lower stratosphere can modulate the absolute vertical wind shear, which disrupts the enhancement of tropical deep convection (Gray et al. 1992). Due to the secondary circulation associated with QBO wind anomalies, the lower stratosphere becomes colder than normal during easterly QBO winters. The colder tropopause and the resulting destabilization in the UTLS could promote organized deep convection. (Gray et al. 1992; Giorgetta et al. 1999; Collimore et al. 2003). Both observational and modeling studies have shown the evidence of QBO-related seasonal-

mean convection and precipitation changes (Giorgetta et al. 1999; Collimore et al. 2003; Liess and Geller 2012), with an enhanced deep convection over the western Pacific during boreal winter in the easterly phase of the QBO (Collimore et al. 2003; Liess and Geller 2012).

Recent studies suggest that the QBO can influence the tropical deep convection in the subseasonal time scale (e.g., MJO). Liu et al. (2014) has shown that the boreal winter MJO becomes more active when the QBO winds are easterly in the lower stratosphere (EQBO) than when the winds are westerly (WQBO). Yoo and Son (2016) has presented that the boreal winter MJO is highly correlated with the QBO and suggested that the QBO-related static stability and vertical wind shear changes modulate the MJO convection.

The QBO–MJO connection opens a new route for improving the MJO prediction. By analyzing reforecasts of the S2S prediction model of the BoM, the boreal winter MJO is better predicted during EQBO winters. The MJO prediction skill during EQBO winters is enhanced by up to 8 days based on the bivariate correlation of 0.5 for RMM indices (Marshall et al. 2017). This enhancement represents over 20% of the overall MJO prediction skill in this model. A possible impact of the QBO on the MJO-induced atmospheric river and its prediction skill is also explored (Baggett et al., 2017; Wang et al., 2018), highlighting the crucial role of the QBO on the subseasonal climate variability from the tropics to extratropics.

Due to a short observational record from the satellite era, climate

model analyses are necessary to better quantify the QBO-MJO connection. The QBO-MJO connection, however, is rarely examined with a long-term climate model simulation. As an initial attempt, Lee and Klingaman (2018) investigated the QBO-MJO relationship in the Global Ocean Mixed Layer configuration of the Met Office Unified Model (MetUM-GOML1). However, this model failed to reproduce the observed QBO-MJO relationship. This failure might be simply caused by the deficiency of the model itself. Although the MetUM-GOML1 well captures the QBO wind, the QBO-related temperature anomalies are substantially underestimated (Lee and Klingaman 2018).

Since the QBO-MJO connection has recently suggested, the QBO impacts on the MJO activity and its related teleconnection have not been well documented (Liu et al. 2014; Yoo and Son 2016; Marshall et al. 2017; Nishimoto and Yoden 2017). The possible mechanisms have been suggested (Yoo and Son 2016; Son et al. 2017; Hendon and Abhik 2018; Zhang and Zhang 2018), but it is not fully understood in detail. In this regard, the main purpose of this thesis is to understand the QBO-MJO relationship. The key questions are as follows:

1) Which MJO characteristics are modulated by the QBO?

2) How does the QBO affect the MJO and its prediction?

3) How can we better simulate the QBO-MJO connection?

Firstly, the QBO-related MJO and its teleconnection are examined in Chap.

2. To better understand the QBO-MJO relationship, a variety of model outputs are used in this thesis partly due to their difficulty in simulating the QBO-MJO connection. Motivated by Lee and Klingaman (2018), the QBO-MJO link is revisited in multiple climate model simulations. The CMIP5 models that simulate realistic QBO are quantitatively evaluated in Chap. 3. Using a dynamical core model, the possible impact of the dynamical process on the QBO-MJO connection is tested (Chap. 4). Extending the result of Marshall et al. (2017), which used only one operational model, the QBO impact on the MJO is further evaluated in all available S2S project data to examine the QBO-MJO connection and its application to the MJO prediction skill (Chap. 5). To better simulate the QBO-MJO connection in the S2S models, the role of the mean biases in MJO prediction skill is further investigated (Chap. 6).

The contents in Chap. 2 are published in Son et al. (2017). Chapter 3 is based on Lim and Son (2020), which is under review. The contents in Chap. 5 and Chap. 6 are published in Lim et al. (2019) and Lim et al. (2018), respectively.

Chapter 2. QBO-MJO connection: observational features

This chapter demonstrates that while the spatial pattern of the seasonal-mean convection and the MJO-related subseasonal convective activity is primarily controlled by the ENSO, the year-to-year variation of overall level of subseasonal convective activity over the central Indian Ocean to the western Pacific, including the MJO, is significantly modulated by the QBO. These different roles of the ENSO and QBO are quantified by performing composite and correlation analyses. After briefly evaluating their relative importance on the seasonal-mean convection (Sect. 2.2), their impacts on the MJO-related subseasonal convective activity are analyzed in detail in Sect. 2.3. Extending Yoo and Son (2016), particular attention is paid to the impact of the QBO on the MJO and the related teleconnections during boreal winter. The seasonality and possible mechanism(s) of the QBO–MJO link are also discussed.

2.1. Data and methods

This study is mostly based on observational data analyses. The only exception is the reanalysis data from the European Center for Medium-Range Weather Forecasts (ECMWF), that is, ERA-Interim (Dee et al. 2011), from 1979 to 2015. These data are used to define the QBO and to examine the QBO-related atmospheric circulation changes. The QBO-related wind and temperature profile changes are examined using radiosonde observations

from the Integrated Global Radiosonde Archive (IGRA; Durre et al. 2006). Only six stations around the Maritime Continent are considered. In terms of station number and geographical location, they are stations 96163 (0.88°S, 100.35°E), 96237 (2.17°S, 106.13°E), 97072 (0.68°S, 119.73°E), 97180 (5.07°S, 119.55°E), 97560 (1.18°S, 136.12°E), and 97724 (3.70°S, 128.08°E). For the easterly QBO (EQBO) and westerly QBO (WQBO) winters, a total of 2176 and 3241 soundings, respectively, are used from 1979 to 2013 (see below for the definition of EQBO and WQBO winters). The high-resolution temperature profiles and the tropopause temperature distributions are also examined by using the global positioning system (GPS) radio occultation (RO) measurements from the Constellation Observing System for Meteorology, Ionosphere and Climate (COSMIC) mission (Anthes et al. 2008) from 2006 to 2015.

Various satellite observations are also used. They include the National Oceanic and Atmospheric Administration (NOAA) Extended Reconstructed Sea Surface Temperature data (ERSST.v4; Huang et al. 2016) from 1979 to 2013, the NOAA interpolated outgoing longwave radiation (OLR) data from 1979 to 2013 (Liebmann and Smith 1996), and the Tropical Rainfall Measuring Mission (TRMM) precipitation data from 1998 to 2013 (Liu et al. 2012). The latter two datasets are used to infer variations in organized tropical convection. To examine cloud distribution near the tropopause, Cloud–Aerosol Lidar with Orthogonal Polarization (CALIOP)

level-2 products (Winker et al. 2007) are also used from 2006 to 2015. Note that each dataset covers different time periods. Most analyses are performed until 2013 because NOAA OLR data are unavailable after 2014. However, for the COSMIC and CALIOP datasets, all available data are used to increase the sample size.

The ENSO is simply defined by the Niño-3.4 (5°S–5°N, 170°–120°W) SST anomaly. When the DJF-mean Niño-3.4 SST anomaly is greater than 0.5 standard deviation, it is set to the El Niño winter. The opposite (i.e., SST anomaly smaller than 20.5 standard deviation) is set to the La Niña winter. For the analysis period of 1979–2013, a total of 10 and 12 years are identified as El Niño and La Niña winters, respectively. Strong ENSO years, addressed below, are also defined with plus or minus one standard deviation.

The QBO is typically characterized by the downward propagation of zonal-mean zonal wind in the equatorial stratosphere (Baldwin et al. 2001). As such, several indices with varying vertical levels have been used in the literature. In this study, the QBO is defined by zonal-mean zonal wind at 50 hPa averaged over 10°S–10°N (U50) from ERA-Interim data, unless otherwise specified. When the seasonal-mean U50 is easterly and smaller than -0.5 standard deviation, it is set to the EQBO. Likewise, the opposite (i.e., westerly and greater than 0.5 standard deviation) is set to the WQBO. Note that the QBO has been often defined by using long-term rawinsonde observations in the tropics (e.g., Naujokat 1986). Although station datasets

are always preferable, one or two stations may not effectively represent the QBO-related zonal-mean circulation change as they could be influenced by local circulation. The fact that the QBO oscillates approximately every 28 months (Baldwin et al. 2001) implies that the number of EQBO and WQBO years can be different. For the analysis period of 1979–2013, a total of 10 and 15 years are identified as EQBO and WQBO winters, respectively. When strong ENSO years are excluded, they become more evenly distributed with eight EQBO and nine WQBO winters. Here it should be emphasized that although the QBO is driven by equatorial waves, which systematically break in the stratosphere, those waves are only partly (not all) excited by large-scale tropical convection. As such, the QBO is only weakly
correlated with the ENSO. The maximum correlation between the Niño-3.4 index and various QBO indices at different levels is only 0.21, and this value is not statistically significant.

The MJO phase and amplitude are defined by the OLR-based MJO index (OMI; Kiladis et al. 2014). Unlike the real-time MJO index (Wheeler and Hendon 2004), this index is solely based on the satellite-derived OLR and more directly discriminates convective signature of the MJO. The OMI consists of the leading pair of empirical orthogonal functions of bandpass-filtered OLR over 20°S–20°N. The two leading principal components (i.e., PC1 and PC2, which are directly obtained online from the NOAA/Earth System Research Laboratory website (http://www.esrl.noaa.gov/psd/mjo/

mjoindex), are then used to define the MJO phase and amplitude. Following the convention of Wheeler and Hendon (2004), the MJO phase is determined in the PC1–PC2 space. Likewise, the MJO amplitude (more precisely, the OMI amplitude) is defined by the square root of the sum of the squared daily values of the two leading PCs [i.e., $(PC1^2+PC2^2)^{1/2}$]. Although not shown, other MJO indices are also tested (Yoo and Son 2016). It turns out that overall results are not sensitive to the choice of the MJO index.

2.2. Interannual variation of seasonal-mean tropical convection by the ENSO

We first examine the relative importance of the ENSO and the QBO on the seasonal-mean and subseasonal tropical convection (Fig. 2.1). Figure 2.1a presents the climatological distribution of the DJF-mean convection in terms of OLR. Three hot spots are evident across the intertropical convergence zone. On interannual time scale, these convective centers, especially those over the western to central Pacific, undergo a significant variation in response to the ENSO (e.g., Martin et al. 2004). Between El Niño and La Niña winters, seasonal-mean OLR exhibits statistically significant differences across the Pacific. Here, statistical significance is tested with Welch's t test (Inoue et al. 2011). Quantitatively, ENSO-related seasonal-mean OLR change is up to 10% of the climatological OLR, with mean convection shifted eastward to the date line and weakened around the Maritime Continent during El Niño winters (cf. Figs. 2.1a,b). The opposite is

true during La Niña winters. These changes reflect a weakened (strengthened) Walker circulation during El Niño (La Niña) winters. Not surprisingly, correlations between DJF-mean OLR, averaged across the Maritime Continents (110°–140°E), and various ENSO indices are very high and statistically significant (see the first OLR column in Table 2.1). In contrast, the QBO-related change in seasonal-mean OLR is rather minor (Fig. 2.1c). As reported in the previous studies, an enhanced convection over the western Pacific and a weakened convection over the eastern Pacific are observed during EQBO winters (e.g., Collimore et al. 2003; Liess and Geller 2012). However, these changes are much smaller than ENSO related changes and not statistically significant. As such, no meaningful correlations are observed between the DJF-mean OLR, averaged across the Maritime Continent, and various QBO indices (Table 2.1).

The above result (i.e., regulation of the DJF-mean convection by the ENSO with a minor contribution of the QBO) is largely insensitive to the season (Table 2.1). In all seasons, seasonal-mean OLR anomalies around the Maritime Continent–western Pacific are highly correlated with ENSO. Although correlations are relatively weak during boreal summer, they are still statistically significant. In contrast, in all seasons, no significant correlations are found for the QBO. These results confirm that the interannual variation of the seasonal-mean tropical convection is predominantly controlled by the ENSO.

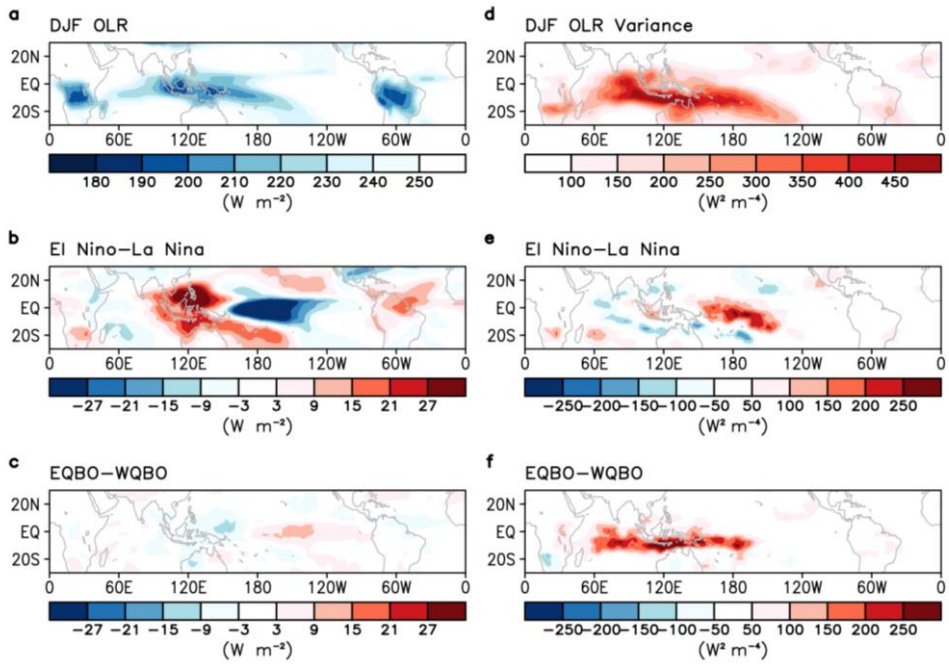

Figure 2.1. DJF-mean OLR and band-pass (20-100 days) filtered OLR variance: (top) long-term climatology, (middle) interannual difference between El Niño and La Niña winters, and (bottom) difference between EQBO and WQBO winters.

Table 2.1. Correlations of seasonal-mean OLR, averaged over the Maritime Continents (15°S-5°N, 110°E-140°E), and MJO amplitude against various ENSO and QBO indices from 1979/1980 winter to 2012/2013 winter. For ENSO indices, Niño3, Niño3.4 and Niño4 indices are used. Likewise, for QBO indices, zonal-mean zonal wind, averaged over 10°N-10°S, at 10 hPa (U10), 20 hPa (U20), 30 hPa (U30), and 50 hPa (U50) are used. Statistically significant values at the 95% confidence levels are denoted with asterisk.

		OLR (Maritime continent)				MJO amplitude			
		DJF	MAM	JJA	SON	DJF	MAM	JJA	SON
ENSO	Niño 3	0.84*	0.47*	0.70*	0.83*	-0.08	-0.19	0.04	-0.14
	Niño 3.4	0.85*	0.64*	0.83*	0.86*	-0.01	0.00	0.20	-0.15
	Niño 4	0.74*	0.69*	0.79*	0.81*	0.11	0.26	0.24	-0.08
QBO	U10	0.02	0.15	0.11	-0.03	0.63*	0.20	-0.01	-0.18
	U20	-0.04	0.09	0.20	0.23	0.33	0.22	-0.17	-0.18
	U30	0.04	0.02	0.10	0.32	-0.16	0.19	-0.23	-0.03
	U50	0.18	-0.04	-0.05	0.18	-0.57*	-0.09	-0.09	0.10

2.3. Interannual modulation of subseasonal tropical convective activity by the QBO

On subseasonal time scale, tropical convection exhibits substantial variability. Figure 2.1d presents the spatial distribution of bandpass-filtered (20–100 days) OLR variance during boreal winter. Strong variability is observed mostly in the Indo-Pacific warm pool region, largely representing the MJO. This localized OLR variance resembles the regional pattern of seasonal-mean convection (cf. Fig. 2.1a). However, there is a subtle difference over the Maritime Continent (e.g., Sobel et al. 2010). While the maximum seasonal mean convection is found at the island (Fig. 2.1a), the maximum variance is observed over the ocean around 5°S (Fig. 2.1d). This may suggest that the detailed processes that determine seasonal-mean convection and subseasonal convective variability are somewhat different.

As in seasonal-mean convection, the subseasonal convective activity varies significantly from year to year (e.g., Hendon et al. 1999). Figure 2.1e presents the ENSO related OLR variance change in DJF. A significant change appears around the date line, with an enhanced variance during El Niño winters. This change is consistent with an eastward extension of mean convection during El Niño winters as depicted in Fig. 2.1b. However, across the Maritime Continent, the ENSO-related OLR variance change is almost negligible. This result indicates that although subseasonal convective activity, including the MJO, tends to extend farther eastward during El Niño winters

(Gualdi et al.1999; Hendon et al. 1999, 2007; Gushchina and Bewitte 2012), its intensity around the Maritime Continent is not strongly regulated by the ENSO. The same result is also found in other seasons (Table 2.1).

It should be noted that the above result, which is based on linear correlation and composite analyses, does not necessarily indicate that ENSO has no impacts on MJO amplitude. In fact, recent studies reported a significant ENSO–MJO link during boreal winter (Feng et al. 2015; Pang et al. 2016). Such a relationship, however, is nonlinear and highly dependent on the characteristics of ENSO itself. For example, it is shown that the MJO becomes stronger than normal during the central Pacific El Niño winters whereas it becomes weaker during the eastern Pacific El Niño winters (Feng et al. 2015; Pang et al. 2016). The sum of these contrasting responses likely results in no systematic changes in MJO amplitude during all El Niño winters. As such, the above result, summarized in Fig. 2.1 and Table 2.1, should be taken as a first-order linear relationship.

Apart from nonlinear impacts of the ENSO, what determines the interannual variation of MJO-related subseasonal convective activity? Figure 2.1f suggests that it is likely the QBO. Near-equatorial OLR variances, across the central Indian Ocean and western Pacific, are typically stronger during EQBO winters (i.e., when DJF U50 is easterly) than WQBO winters. Their differences reach up to 40%–50% of the climatological OLR variance around the Maritime Continents (cf. Figs. 2.1d,f). More importantly, unlike the

ENSO-related OLR variance change (Fig. 2.1e), the QBO-related change is centered at 5°S and almost exclusively present in the Indo-Pacific region, from 60°E to 180°, where MJO is active during boreal winter [see also Yoo and Son (2016)].

The ENSO–MJO and QBO–MJO relationships are further evaluated by correlation analyses. Linear correlations are computed for the DJF-mean MJO amplitude against various ENSO and QBO indices (see the MJO column in Table 2.1). No significant link is found between ENSO and MJO amplitude in all seasons, supporting previous studies (e.g., Hendon et al. 1999, 2007). In contrast, during boreal winter, statistically significant correlations with the QBO, which are greater than ±0.5, are observed from the upper stratosphere (i.e., 10 hPa) to the lower stratosphere (i.e., 50 hPa) with a switching sign. This height-dependent correlation represents a quasiperiodic downward propagation of zonal-mean zonal wind in association with the QBO (see also Fig. 2.6b, which is discussed later). Note that the correlation coefficient for the zonal-mean zonal wind at 10hPa (U10) is larger than the one at 50 hPa (U50). This is partly due to the internal variability of zonal-mean zonal wind in the lower stratosphere, which is introduced by the wave activities in the upper troposphere and lower stratosphere. Note also that the QBO–MJO link appears only in the boreal winter (Table 2.1). This seasonality is discussed in Sect. 2.3.4.

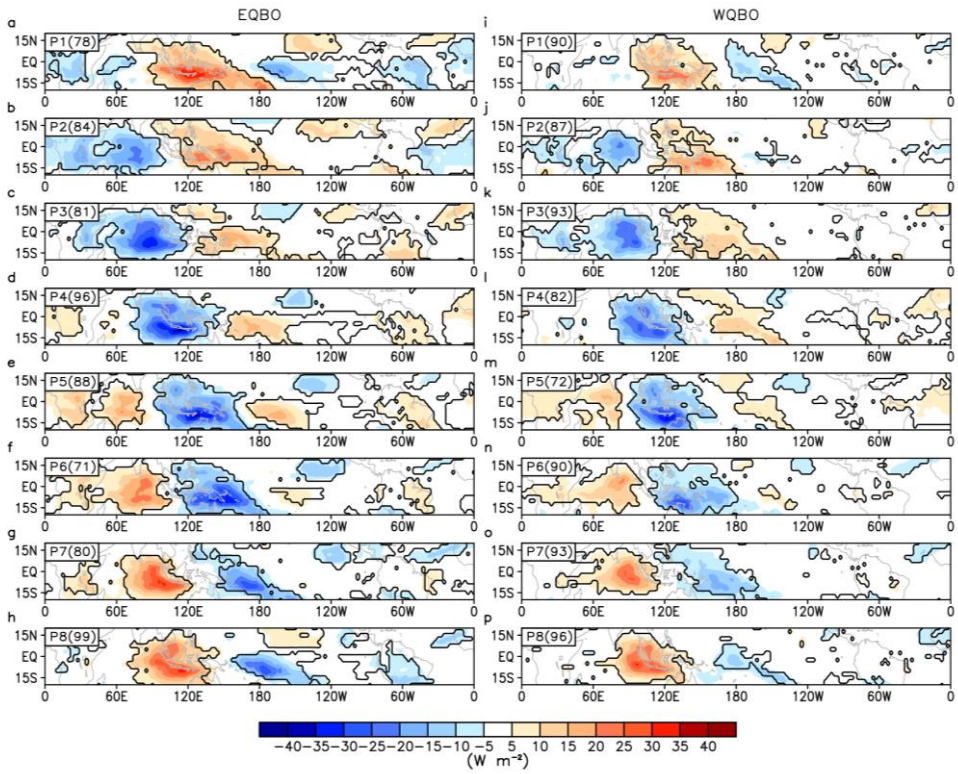

Figure 2.2. Composite of band-pass (20-100 days) filtered OLR anomaly for each MJO phase during (left) EQBO and (right) WQBO winters. Only days when OMI amplitude is greater than 1.0 are used, and seasonal-mean values in each year are subtracted to remove interannual variation of background flow. Sample size is denoted at top-left corner of each panel, and statistically significant values at the 95% confidence level are contoured.

2.3.1. MJO Characteristics with the QBO

To establish the QBO–MJO coupling more directly, composite OLR anomalies are presented for each MJO phase (Fig. 2.2). Here, a statistical significance test is performed using a Student's t test by counting the number of degrees of freedom only when each day in a given phase is separated by at least seven days (Garfinkel et al. 2012). It is evident from Fig. 2.2 that, for most MJO phases, the OLR anomalies, subject to bandpass filtering (20–100 days), are stronger during EQBO winters than WQBO winters. If only active MJOs are considered (i.e., when the MJO amplitude exceeds 1 and consistently propagates eastward in time), their differences become even larger and statistically significant for all MJO phases (Yoo and Son 2016). Although not shown, this result is not sensitive to the inclusion or exclusion of strong ENSO years.

Although OLR is widely used to quantify tropical deep convection, it does not necessarily represent precipitating clouds. In other words, the QBO–MJO relationship, illustrated in Fig. 2.2, may simply represent nonprecipitating cloud changes in the upper troposphere. To test such a possibility, the same analysis is repeated with high-resolution precipitation data (Fig. 2.3). The same result, with a much larger difference between EQBO and WQBO winters, is obtained. This result clearly indicates that, on interannual time scales, the MJO-related subseasonal convective activity is more sensitive to the stratospheric mean state change than the SST change

associated with ENSO.

The QBO–MJO link is evident not only in the MJO amplitude but also in the propagation speed and frequency of MJO. Eastward propagation of OLR anomalies and the associated lower-tropospheric circulations become more pronounced during EQBO winters (Fig. 2.4). Their propagation speed is also somewhat slower [see also Nishimoto and Yoden (2017)]. Most importantly, the period of MJO, estimated by the distance from the center of blue shading at negative lags to that at positive lags in Fig. 2.4, becomes longer during EQBO winters. Based on auto-lag correlation of PC1, it is found that the MJO period during EQBO winters is about 50 days. This is about 10 days longer than the estimated MJO period during WQBO winters.

A slower propagation and longer period of MJO during EQBO winters may be simply explained by the MJO amplitude change itself. A simple composite analysis has shown that strong MJO events, regardless of the QBO, tend to propagate more slowly across the Maritime Continent than weak MJO events (Seo and Kumar 2008). They also exhibit a longer period than the latter (Seo and Kumar 2008). Although the MJO propagation is not simply controlled by the equatorial waves, it is at least in part influenced by the phase speed of planetary-scale Kelvin waves. In a simple model, the Kelvin waves become slower when diabatic heating (or precipitation rate) increases [e.g., Chang (1977) or, more recently, Kang et al. (2013)]. This may imply a slower MJO propagation when the MJO-related convection becomes

stronger. If a new MJO over the Indian Ocean is initiated by the decaying MJO over the western Pacific (e.g., Zhao et al. 2013), a slower MJO propagation to the Pacific would then result in a delayed MJO initiation. This may lead to a longer period of MJO events. Based on these speculations, we argue that a key factor of the QBO–MJO coupling is the QBO-related MJO amplitude change.

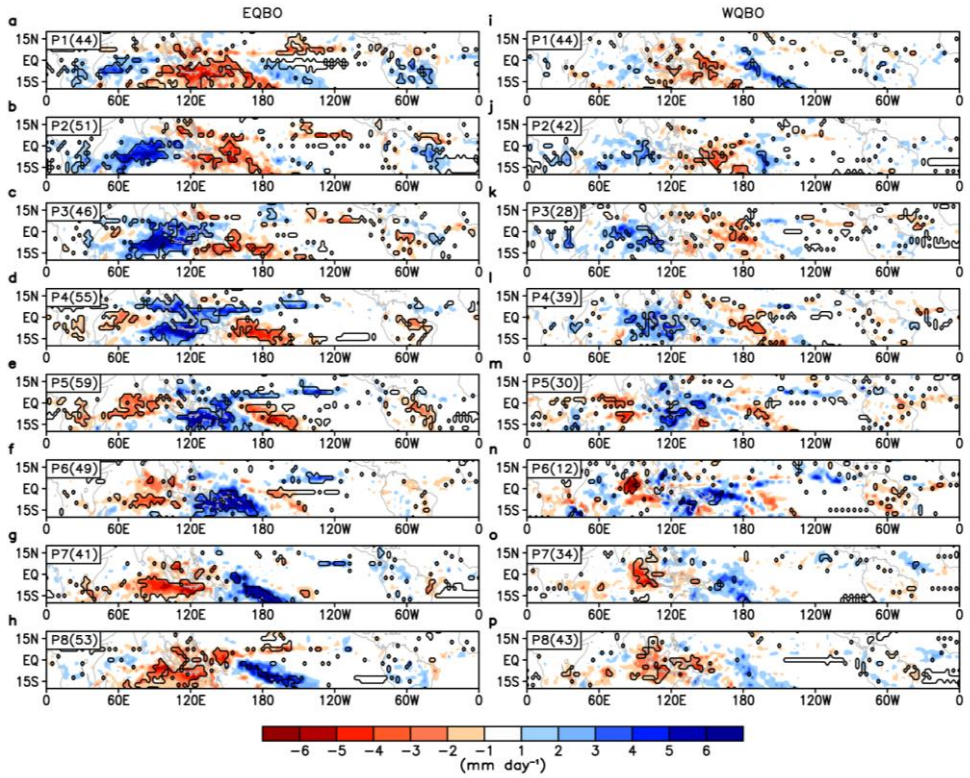

Figure 2.3. Same as Fig. 2.2 but for TRMM precipitation.

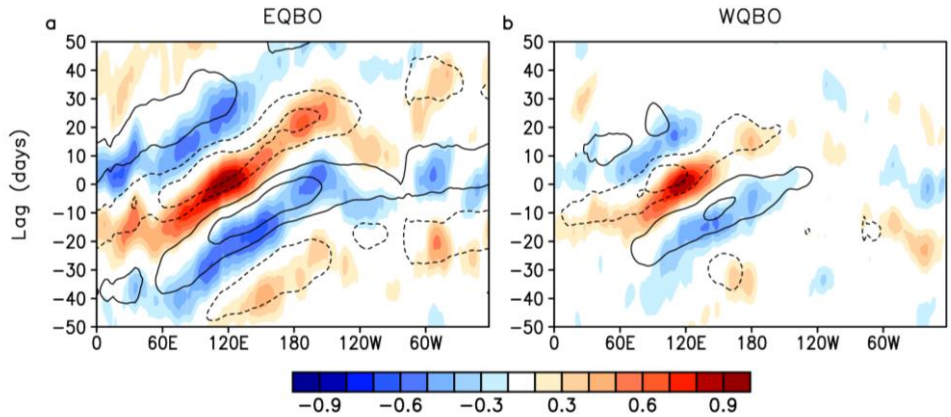

Figure 2.4. Correlation coefficient of OLR (shading) and 850-hPa zonal wind anomalies (contour), averaged over 15°S-5°N, against OLR anomaly over the Maritime continent (15°S-5°N, 100°E-130°E) during boreal winter. Shading and contour intervals are 0.3 and 0.1, respectively. Zero lines are omitted.

2.3.2. MJO teleconnection with the QBO

A stronger and more organized MJO during EQBO winters also implies an enhanced MJO-related tropical–extratropical teleconnection. This is indeed the case. Figure 2.5 presents the time-lagged composite of 300 hPa stream function anomalies for the MJO phases 2 and 3 when the MJO convection is located over the Indian Ocean. The MJO teleconnections [i.e., strong positive anomaly over South Asia and a wave train across the North Pacific (e.g., Lin et al. 2009)] is more pronounced during EQBO winters (Figs. 2.5a-b). In contrast, the overall pattern is less organized during WQBO winters especially at lag 10 days (Figs. 2.5c-d). Here it should be emphasized that the enhanced MJO teleconnections appear to be primarily driven by the strengthened convection itself. This contrasts with the ENSO modulation of the MJO teleconnections that is associated with background flow change (Moon et al. 2011). Although the QBO also accompanies a subtropical jet change (Baldwin et al. 2001; Garfinkel and Hartmann 2010), such a change is much weaker than the one for the ENSO and does not likely affect the MJO teleconnections. More details of QBO-induced MJO teleconnection changes will be documented in a future study.

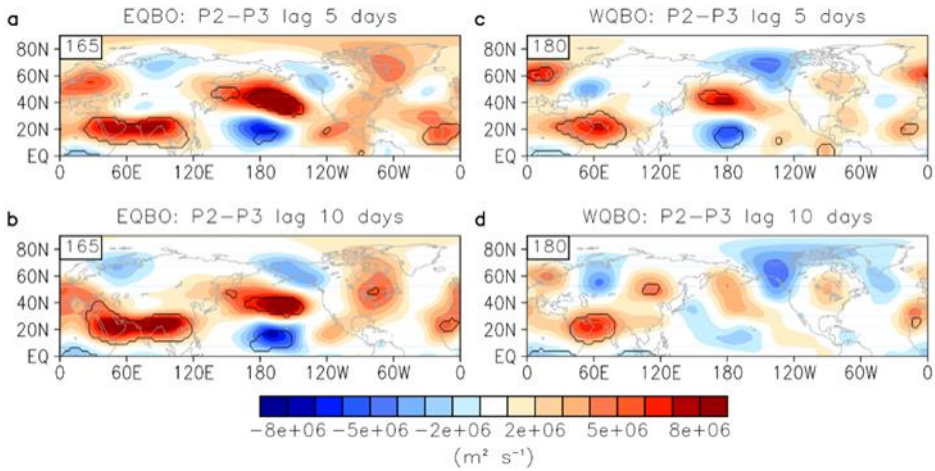

Figure 2.5. Lagged composite of 300-hPa stream function anomaly for MJO phase 2 and 3 when convections are located at the eastern Indian Ocean. (top) Lag 5 and (bottom) lag 10 days are shown for (left) EQBO and (right) WQBO winter, separately. Only days when OMI amplitude is greater than 1.0 are used, and seasonal-mean values in each year are subtracted to remove interannual variation of background flow. To reduce noises, 5-day running mean average is also applied. Statistically significant values at the 95% confidence level are contoured.

2.3.3. Lead-lag relationship

The above results do not necessarily reveal a causal relationship as time lags are not taken into account. That is, the QBO–MJO coupling may not result from the downward influence of the QBO. It could be instead caused by the upward influence of the MJO. In fact, it is well established that the QBO is influenced by the convectively coupled gravity waves (Baldwin et al. 2001) and is better simulated when a parameterization of convectively driven gravity waves is implemented in the model (Kim et al. 2013b). Figure 2.6a shows the lead–lag correlation of 3-month running-mean U50 against the DJF MJO amplitude. Negative lags indicate that the former leads the latter. Statistically significant correlations are observed from lag -6 (June–August) to lag 2 months (February–April). Although it is not distinguishable by eyes, the maximum negative correlation is found at lag -2, that is, U50 leading DJF MJO amplitude about two months [see also Marshall et al. (2017)]. To better understand this lead–lag relationship, the analysis is extended to the whole stratosphere (Fig. 2.6b). Unlike at 50 hPa, maximum correlation at 10 hPa appears at positive lags, possibly indicating a modulation of QBO by the MJO. However, even at 10 hPa, significant correlations start to appear at negative time lags. More importantly, they propagate downward in time, reflecting a quasi-periodic oscillation of the QBO, with a much longer time scale than the time scale of MJO itself. This result suggests that the QBO–MJO coupling is mostly downward from the stratosphere to the troposphere although the

upward influence is not negligible. A possible two-way interaction between the QBO and MJO deserves further analysis.

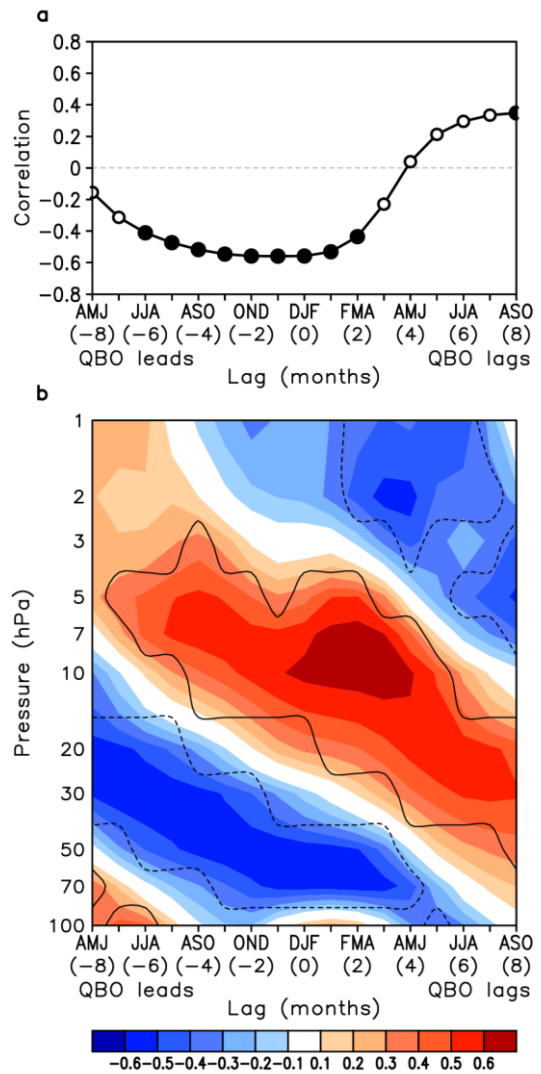

Figure 2.6. (a) Lead-lag correlation of U50 against the DJF MJO amplitude and (b) its extension to the whole stratosphere. Statistically significant values at the 95% confidence level are denoted with filled circles in (a) and are contoured in (b). Positive lag indicates that the DJF MJO amplitude leads QBO.

2.3.4. Seasonality

As highlighted in Yoo and Son (2016), the QBO–MJO coupling appears only in the boreal winter (see Table 2.1). No significant relationships are found in other seasons. Even in spring when MJO is still active, the QBO–MJO link is almost absent. This seasonal dependency may partly result from the seasonality of the QBO phase transition. The QBO tends to change its phase approximately every 14 months. During the analysis period (1979–2013), it primarily occurred in spring with a minimum variance of U50 (not shown). In other words, the QBO-related mean state is relatively weak in spring compared to other seasons, possibly explaining a rather weak influence of the QBO on springtime MJO. Other possible factor is a seasonal cycle of tropopause. The tropical tropopause is highest during boreal winter (Kim and Son 2012). This observation suggests that the QBO changes tropopause properties most effectively during boreal winter. If the MJO is influenced by the dynamical processes near the tropopause, this suggests more effective modulation of the MJO by the QBO during boreal winter than during boreal spring. During summer and fall, the MJO itself is weak and not well organized (Zhang 2013). In particular, the summertime MJO tends to propagate northward, away from the equator where the QBO is active. These conditions may explain a negligible QBO–MJO connection in these seasons (Yoo and Son 2016). To confirm these speculations, further studies are needed.

2.3.5. Possible mechanism(s) of the QBO-MJO connection

It is unclear how the QBO affects the MJO. One of the possible mechanisms is the static stability change in the upper troposphere (Reid and Gage 1985; Gray et al. 1992; Giorgetta et al. 1999; Garfinkel and Hartmann 2011; Yoo and Son 2016). The downward propagation of zonal-mean zonal wind accompanies the secondary circulation in the subtropical stratosphere as a result of the thermal wind balance (Baldwin et al. 2001). The net result is a vertical pair of adiabatic cooling and warming at the equatorial stratosphere (Figs. 2.7a,b). Although less organized, a hint of adiabatic warming and cooling also appears in the Northern Hemisphere subtropics, reflecting returning flow of the secondary circulation. The zonal wind and temperature anomalies also appear in the polar stratosphere (Figs. 2.7a,b). This is caused by planetary-scale wave and zonal mean flow interaction in the extratropical stratosphere (Holton and Tan 1980) and not directly relevant to the QBO–MJO link.

The observed zonal wind and temperature profiles are further illustrated in Figs. 2.7c and 2.7d from long-term radiosonde observations. In spite of large interannual variability, QBO-related temperature anomalies that are greater than ±1 K are evident in the lower stratosphere. More importantly, these temperature anomalies, centered at 70 hPa, are not confined within the stratosphere but extend to the upper troposphere below 100 hPa (Note that the DJF-mean tropopause in this region is located at 100 hPa). The static stability

changes, which are proportional to the vertical gradient of temperature profiles, are observed even at 150 hPa (Fig. 2.7e). A qualitatively similar result is also found in the high-resolution temperature profiles derived from the COSMIC GPS RO measurements (not shown).

Figure 2.7e indicates that the near-tropopause static stability is relatively weaker during EQBO winters. If the MJO, which is well organized in the vertical, is influenced by the static stability near the tropical tropopause, such a destabilization could enhance the MJO. This possibility is supported by the recent modeling study (Nie and Sobel 2015). On the other hand, since the QBO may regulate only organized high-top clouds (Collimore et al. 2003), its influence on seasonal-mean convection, which consists of various clouds such as low-, mid-, and high-top clouds, would be rather minor (Fig. 2.1c).

The near-tropopause static stability change, caused by adiabatic heating associated with the QBO-induced secondary circulation, may be further enhanced by the diabatic process resulting from cirrus clouds. As shown in Fig. 7d, tropopause temperature is much colder during EQBO winters than WQBO winters. This may allow more frequent formation of cirrus clouds near the tropopause. Figures 2.8a and 2.8b illustrate the spatial distribution of the DJF-mean temperature at the cold-point tropopause as derived from COSMIC GPS RO measurements. Because the longitudinal distribution of the tropical tropopause temperature is largely determined by the underlying convection (Kim and Son 2012), its spatial pattern follows the

DJF-mean OLR distribution very well (cf. Fig. 2.1a and Figs. 2.8a,b). However, the QBO-related tropopause temperature change, up to -2 K, is largely homogeneous in the deep tropics.

Figures 2.8d–f show that the fraction of cirrus clouds, estimated from CALIOP measurements, is sensitive to the tropopause temperature. For colder tropopause temperature during EQBO winter, cirrus clouds form more frequently especially across the Maritime Continent and central Pacific (Fig. 2.8f). Because near-tropopause cirrus clouds result in a net radiative cooling in the lower stratosphere and warming in the troposphere (Hartmann et al. 2001; Yang et al. 2010; Hong et al. 2016), this may destabilize the tropical upper troposphere, especially near the tropopause, helping a development of the organized deep convection. Note that even without cirrus clouds, the cold tropopause itself could provide a favorable environment for organized deep convection (e.g., Emanuel et al. 2013).

The adiabatic and diabatic processes described above may not be the sole potential mechanism that affects the MJO. Other mechanisms, which may include vertical wind shear (Gray et al. 1992; Collimore et al. 2003; Ho et al. 2009), absolute vorticity (Collimore et al. 2003), and tropopause changes (Reid and Gage 1985; Gray et al. 1992), are not exclusive. Presumably, the QBO–MJO link is associated with multiple factors. To identify the exact mechanism(s), further studies, using both observations and numerical models, are needed. In this regard, a cloud-resolving model

experiment (e.g., Nie and Sobel 2015) would be very useful.

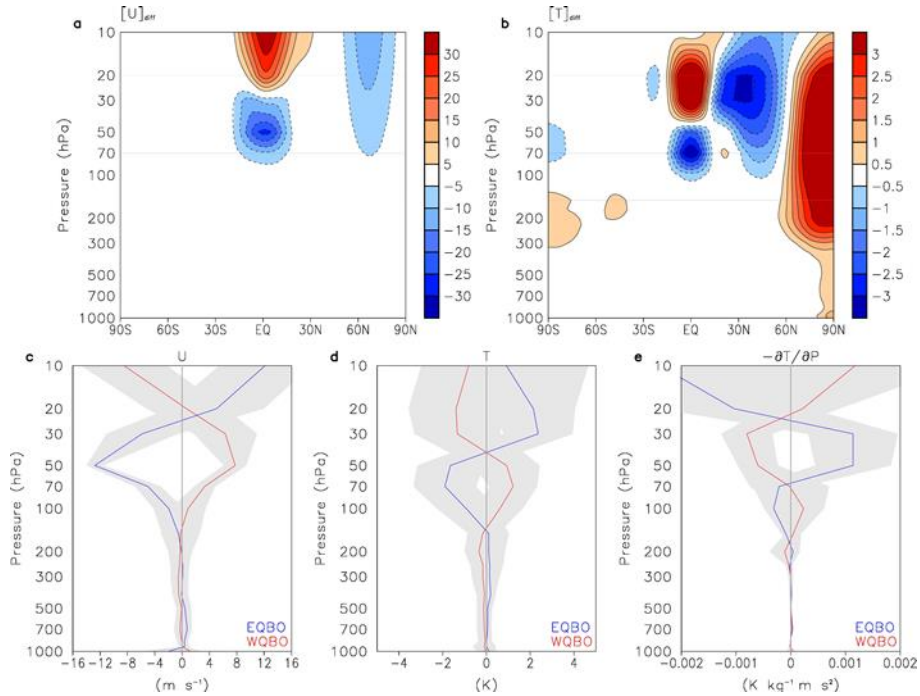

Figure 2.7. Difference in zonal-mean (a) zonal wind (m s^{-1}) and (b) temperature (K) between EQBO and WQBO winters from the ERA-Interim. (c) Observed zonal wind, (d) temperature, and (e) vertical temperature gradient anomalies averaged over six IGRA stations around the Maritime Continent, during EQBO (blue) and WQBO (red) winters. The 0.5 standard deviation range is shown in gray.

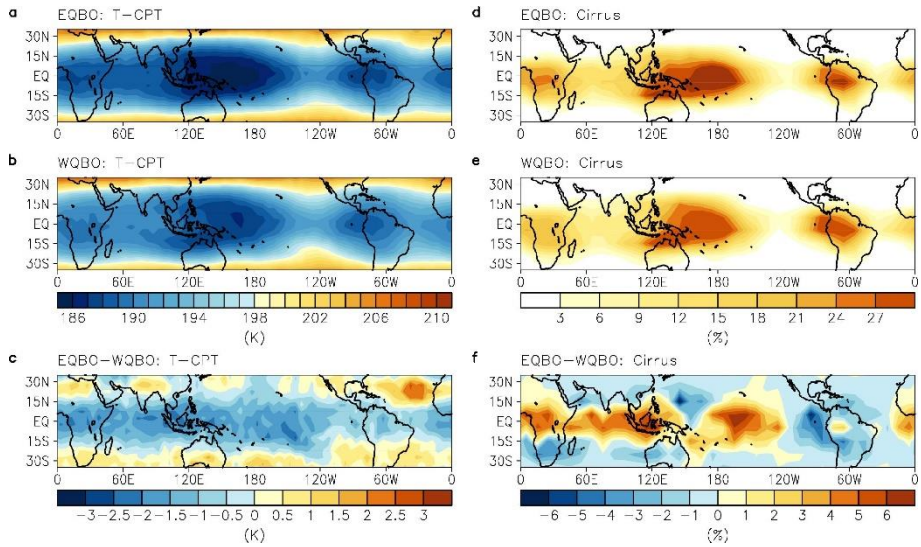

Figure 2.8. Spatial distribution of DJF-mean temperature at the cold-point tropopause (K), derived from the COSMIC GPS RO measurements, for (a) EQBO and (b) WQBO winters and (c) their difference. (d)–(f) As in (a)–(c), but for the near-tropopause cirrus frequency (%) from the CALIOP measurements.

Chapter 3. QBO-MJO connection in current climate models

In Chap. 3, the QBO-MJO relationship is quantitatively evaluated using CMIP5 models (Taylor et al. 2013) that simulate realistic QBO. The QBO and MJO simulations in the four CMIP5 models are presented in Sect. 3.2. The MPI-ESM-MR simulations, which show a weak QBO-MJO connection, are further discussed in Sect. 3.3.

3.1. Data and methods

The four CMIP5 models that internally generate the QBO [see Fig. 1 of Butchart et al. (2018)] are analyzed. They are MIROC-ESM, MIROC-ESM-CHEM, HadGEM2-CC, and MPI-ESM-MR as listed in Table 3.1. We use only historical runs from 1950's to 2005. To increase a sample size, all available ensemble members are used. Except for MIROC-ESM-CHEM that has only one ensemble member, all models have three ensemble members.

The model output is verified against ERA-Interim reanalysis data from the ECMWF (Dee et al. 2011) and OLR (Liebmann and Smith 1996) and Extended Reconstructed Sea Surface Temperature v5 (Huang et al. 2017) from the NOAA for the period of 1979-2017. These reference datasets are simply referred to as the observations in this chapter. The one-to-one comparison is then performed by interpolating both the model simulations and the observations onto a common resolution of 2.5°×2.5°. Note that the analysis period differs between the model simulations and the observation.

This difference is not an issue in this study because only composite analyses (not time series) are conducted below.

To exclude the ENSO influence on the MJO, all analyses are conducted for the ENSO-neutral winters. The ENSO indices are derived from monthly SST data in the observation and in the model simulations, respectively. The SST anomalies are simply averaged over the Niño 3.4 region (170°W-120°W, 5°S-5°N) to compute the ENSO index. The El Niño or La Niña winters are defined in each model when the DJF-mean ENSO index is greater than 1.0 standard deviation or smaller than -1.0 standard deviation.

The QBO index is defined by 50-hPa zonal-mean zonal wind anomalies over the tropics (10°S-10°N), same with Chap. 2. When the DJF-mean QBO index is smaller than -0.5 standard deviation in each model, it is defined as EQBO winter. The opposite is true for WQBO winter. By excluding ENSO winters, a total of 9 and 12 winters are identified as EQBO and WQBO winters in the observation. In the model simulations, EQBO and WQBO winters are at least 17 and 16 years as summarized in Table 3.1 (rightmost column). If MIROC-ESM-CHEM is excluded, EQBO and WQBO winters are more than 27 and 40 years.

Table 3.1. A list of four models used in Sect. 3.2

Model	Model resolution (Model top)	Period	Ensemble size	EQBO/WQBO years
HadGEM2-CC	1.25°x1.875° L60 (85 km)	1959.12 -2005.11	3	35/40
MIROC-ESM	T42 (~2.8°) L80 (0.0036 hPa)	1950.01 -2005.12	3	27/47
MIROC-ESM-CHEM	T42 (~2.8°) L80 (0.0036 hPa)	1950.01 -2005.12	1	17/16
MPI-ESM-MR	T63 (~1.9°) L95 (0.01 hPa)	1950.01 -2005.12	3	37/49

The real-time multivariate MJO (RMM) indices (Wheeler and Hendon 2004) are computed to quantify MJO activities. Following Henderson et al. (2016), equatorially averaged (15°S-15°N) 250-zonal wind (U250), 850-hPa zonal wind (U850), and OLR anomalies are projected onto the Combined Empirical Orthogonal Functions (CEOFs) from Wheeler and Hendon (2004). More specifically, the RMM indices are calculated as follows: the averaged values of the previous 120 days are removed from each variable to reduce the influence of interannual variability, and then the first three harmonics of the daily climatology are removed to reduce the seasonal cycle. By using the standard deviation of each variable from the observation, the three variables are normalized and projected onto the CEOFs to obtain the RMM1 and RMM2. Unlike in Wheeler and Hendon (2004) who used 200-hPa zonal wind, 250-hPa zonal wind is used here since 200-hPa data is not available in the model. The daily RMM amplitude is then defined by $\sqrt{\mathrm{RMM1}^2 + \mathrm{RMM2}^2}$. Only active MJO days when the MJO amplitude is greater than 1.0 are considered in the composite analyses.

The OMI indices are also used in this study for the sensitivity test. The OMI indices are generated as follows: first, the OLR between 20°S and 20°N is 20-96 day bandpass filtered, and then is projected onto the time-varying spatial Empirical Orthogonal Functions downloaded from website (https://www.esrl.noaa.gov/psd/mjo/mjoindex/) to obtain OMI1 and OMI2. Following Kiladis et al. (2014), we normalize OMI1 to have a standard

deviation of one, and the same scaling with OMI1 is used to normalize OMI2 to consider its relative weighting with respect to OMI1.

3.2. QBO and MJO simulations in CMIP5 models

Figure 3.1 displays the time series of equatorially averaged (10°S-10°N) zonal-mean zonal wind anomalies in the lower stratosphere from the ERA-Interim reanalysis and four CMIP5 models. Only the first ensemble member is used in Figs. 3.1b-e for a common analysis period of 1979-2005. Except for this figure in this study, all other figures are based on all available datasets (39 years for observations and at least 46 years for model simulations; Table 1) excluding strong ENSO years.

An alteration of zonal wind from easterly to westerly and its downward propagation are evident in Fig. 3.1a. The period of wind change is approximately 28 months, and its downward propagation is limited to the tropopause level. These characteristics are reasonably well captured by the climate models (Figs. 3.1b-e), although the QBO amplitude below 30 hPa is slightly weaker, and the descent rate is somewhat slower than the observations (e.g., Schenzinger et al. 2017). Consistent with the observations, the westerly winds at 70 hPa remain for a longer time with a slower descent rate than the easterly winds. The mean periods of zonal wind are also similar to the observation, ranging from about 26 months to 30 months. Most importantly, the downward propagation of QBO anomalies is well reproduced near the

tropopause level. Based on Table 3 of Schenzinger et al. (2017), the lowest levels of the QBO activity in HadGEM2-CC and MPI-ESM-MR simulations, which are defined as the level of 10% of the maximum amplitude, are only 3 hPa and 2 hPa higher than that of observation (i.e., 86 hPa; Table 3 of Schenzinger et al. 2017). Although not shown, essentially the same results are also found in the other ensemble members.

A subtle difference between the models is also evident in Figs. 3.1b-e. For instance, MIROC-ESM exhibits the weakest QBO amplitude among the four models. The MIROC-ESM-CHEM, which is a coupled version of MIROC-ESM, has a relatively weak QBO downward propagation, with its lowest level at about 10 hPa higher than the observation (Table 3 of Schenzinger et al. 2017). As the MJO convection depends on both the amplitude and the height of the QBO-related temperature anomalies (Martin et al. 2019), these differences in the simulated QBO could affect the QBO-MJO connection in the model.

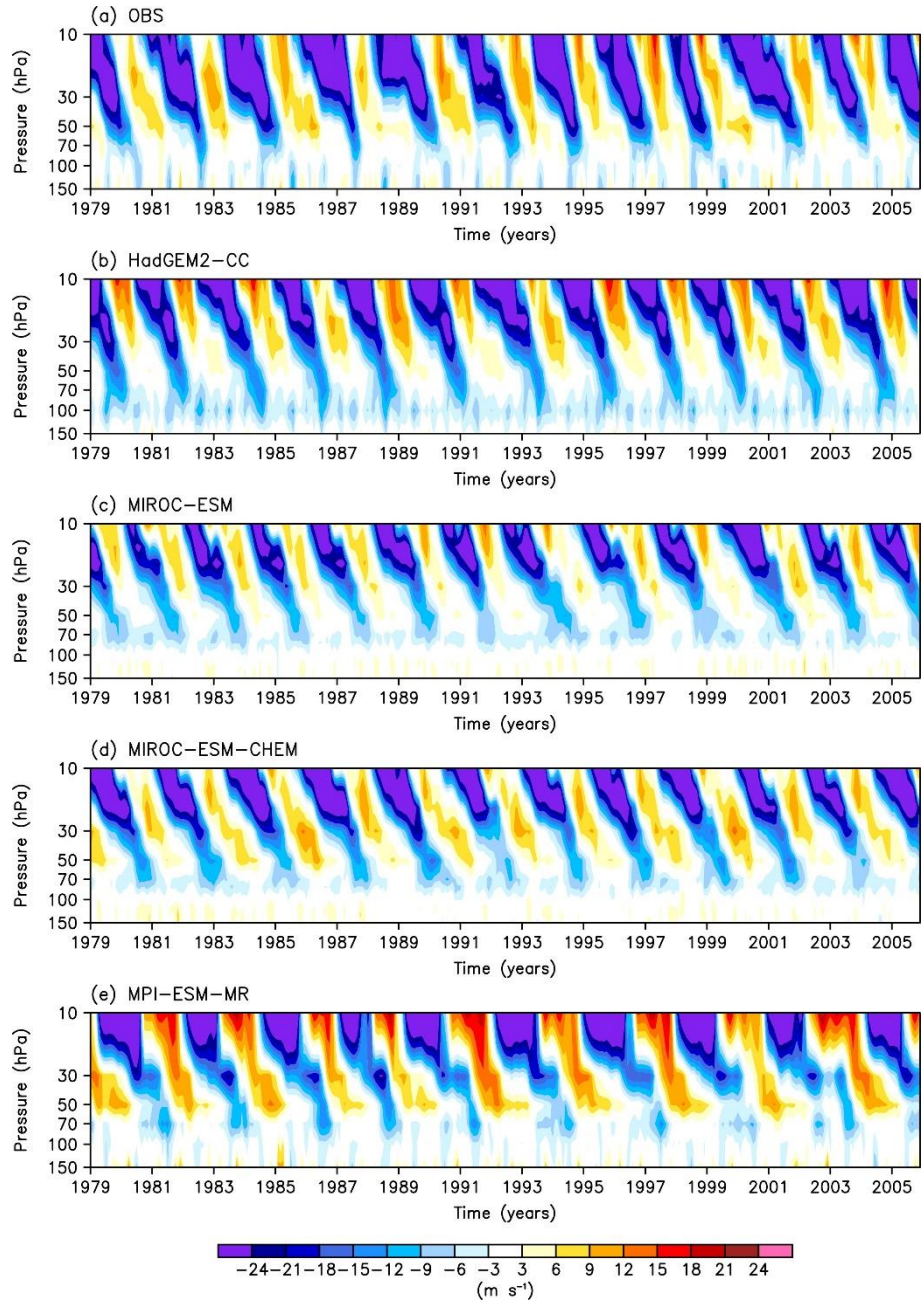

Figure 3.1. Time-height cross section of equatorially averaged (10°S-10°N) zonal-mean zonal winds in (a) the observation and (b-e) model simulations.

The MJO simulations in the four CMIP5 models are also briefly evaluated in Fig. 3.2 (left column). A 20-100 day bandpass filter is applied to OLR anomalies and its standard deviation is computed for December-February in each year. The standard deviation in each year is then averaged for all winters using all ensemble members.

In the observation (Fig. 3.2a), the MJO-related OLR variability is maximized near 120°E. The second maxima are also found over the eastern Indian Ocean and the western Pacific where sea surface temperature is warm. This spatial structure is not well reproduced by climate models (see also Ahn et al. 2017). The HadGEM2-CC shows the maximum MJO activity over the Indian Ocean and western Pacific but not over the Maritime Continents (Fig. 3.2c). The overall amplitude is also weaker than the observation. Both MIROC-ESM and MIROC-ESM-CHEM fail to capture the MJO-related OLR variability (Figs. 3.2e,g). Ahn et al. (2017) reported that these models have a weak OLR variance and negligible MJO eastward propagation. In contrast, MPI-ESM-MR exhibits a stronger OLR standard deviation than the observation with a maximum value over the Maritime Continents (Fig. 3.2i). As illustrated later, this model also simulates an eastward propagation of MJO anomalies.

The above analyses suggest that MPI-ESM-MR has the most realistic QBO and MJO. However, a successful simulation of both the QBO and MJO does not guarantee a realistic representation of the QBO-MJO connection

(e.g., Lee and Klingaman 2018). In Fig. 3.2 (right column), the QBO-MJO connection is tested by computing the difference in bandpass filtered OLR standard deviation between EQBO and WQBO winters. Consistent with the previous studies (Yoo and Son, 2016; Son et al. 2017), MJO activities become stronger during EQBO winters than during WQBO winters in the observation (Fig. 3.2b). The largest difference is observed over the Maritime Continents and extended eastward into the Pacific Ocean.

The observed QBO-MJO connection is not well reproduced in most models (Figs. 3.2d,f,h,j). The HadGEM2-CC exhibits no significant difference in MJO-filtered OLR standard deviation. Although not shown, HadGEM2-CC has positive OLR biases, indicating that the cloud top height is lower than the observation. The lower cloud top is unlikely influenced by the QBO. Both MIROC-ESM-CHEM and MIROC-ESM also show negligible differences. This result is anticipated because the MJO variability itself is not realistic in these two models (Figs. 3.2e,g). In contrast to these three models, the MPI-ESM-MR exhibits a weak hint of the QBO-MJO connection especially over the western Pacific (Fig. 3.2j). The MJO activity is enhanced over 150°E-160°W during EQBO winters as in the observation (compare Figs. 3.2j and 3.2b), and this enhancement is statistically significant in some regions. This model, however, fails to capture the QBO-MJO connection over the Indian Ocean and Maritime Continents. Based on this finding, below we focus on the QBO-MJO connection in MPI-ESM-MR

simulations.

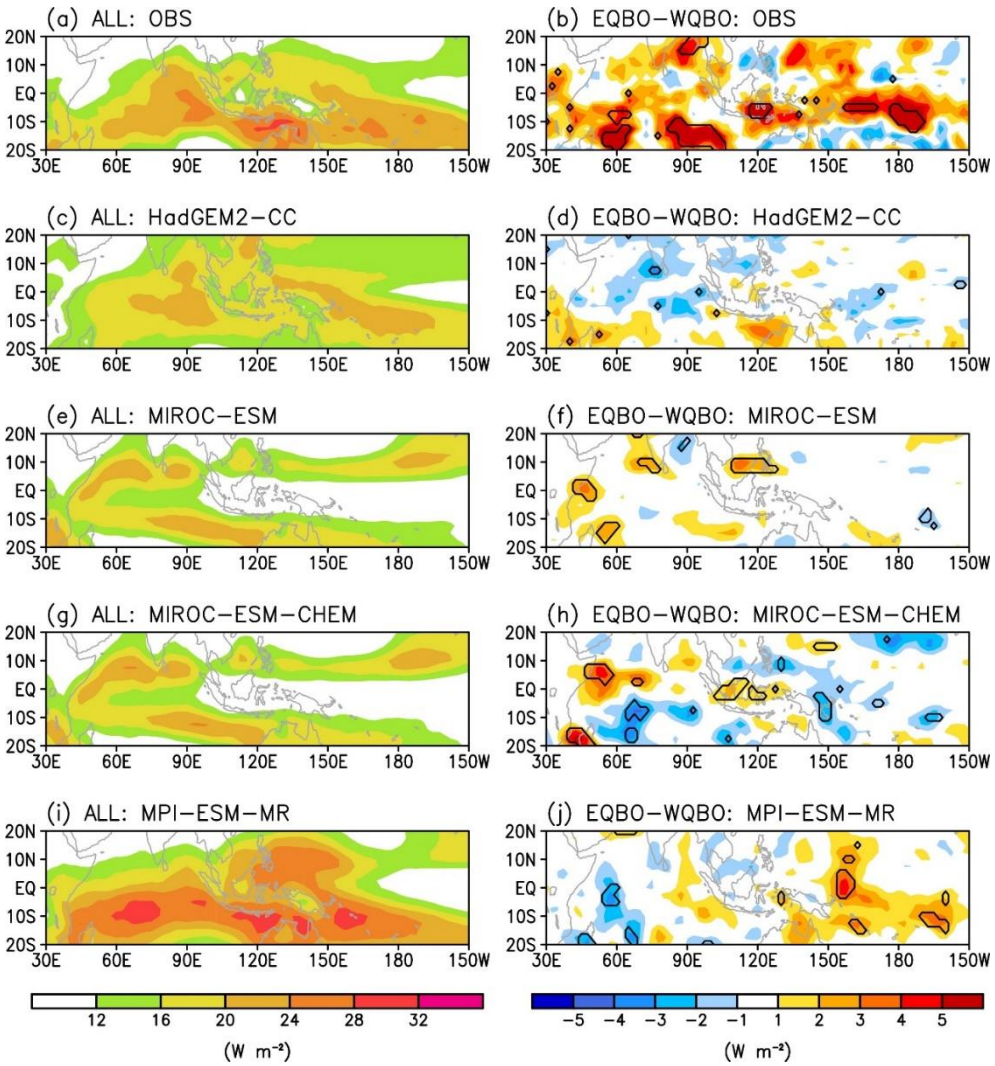

Figure 3.2. (a) Standard deviation of 20-100 day bandpass filtered OLR anomalies in DJF and (b) the difference between EQBO and WQBO winters in the observation. (c-j) Same with (a-b) but in the four CMIP5 models. The values that are statistically significant at the 95% confidence level are contoured in the right column.

3.3. QBO-MJO connection in MPI-ESM-MR simulations

Figure 3.3a presents the eastward propagation of MJO wind and OLR anomalies in the observations. The 20-100 day filtered OLR anomalies are averaged over 10°S-10°N and regressed onto the OLR anomalies over the Maritime Continents (110°-130°E, 10°S-10°N). The regression coefficients are calculated in each winter and then averaged over all winters as in Fig. 3.2a. The resulting OLR anomalies are multiplied by -1, representing negative anomalies the enhanced convection. The same analyses are also performed with the MPI-ESM-MR simulations (Fig. 3.3d). As addressed earlier, all available datasets (i.e., three ensemble members for 55-year long MPI-ESM-MR simulations) excluding strong ENSO years are considered.

Both the observation and model simulations show the enhanced convection over the eastern Indian Ocean at lag -10, which propagates eastward across the western Pacific at about lag 10. The suppressed convection is accompanied by the enhanced convection. The MJO period, which is qualitatively estimated by the time distance between the two red shadings near 120°E, is also similar between the two datasets (Figs. 3.3a,d). However, the modeled MJO amplitude is significantly weaker than the observation. The traveling distance of the MJO anomalies is also much shorter than the observation. These are well-known biases of CMIP5 models, possibly caused by the lack of convection-circulation coupling and the lack of physical parameterizations (e.g., Ahn et al. 2017; Gonzalez and Jiang 2017).

Next, we evaluate the temporal evolution of the QBO-MJO connection in this model. Figures 3.3b and c show the regression maps of the observed OLR and U850 anomalies during EQBO and WQBO winters as in Fig. 3.3a. Consistent with previous studies (e.g., Nishimoto and Yoden 2017; Son et al. 2017), the MJO convective anomalies during EQBO winters propagate further eastward than those during WQBO winters with a slightly slower propagation speed (5.5 m s^{-1} for EQBO and 6.9 m s^{-1} for WQBO winters). The formers also remain for a longer time than the latters. Based on the auto-lag correlation of RMM1 (not shown), the MJO period during EQBO winters is approximately 10 days longer than that during WQBO winters.

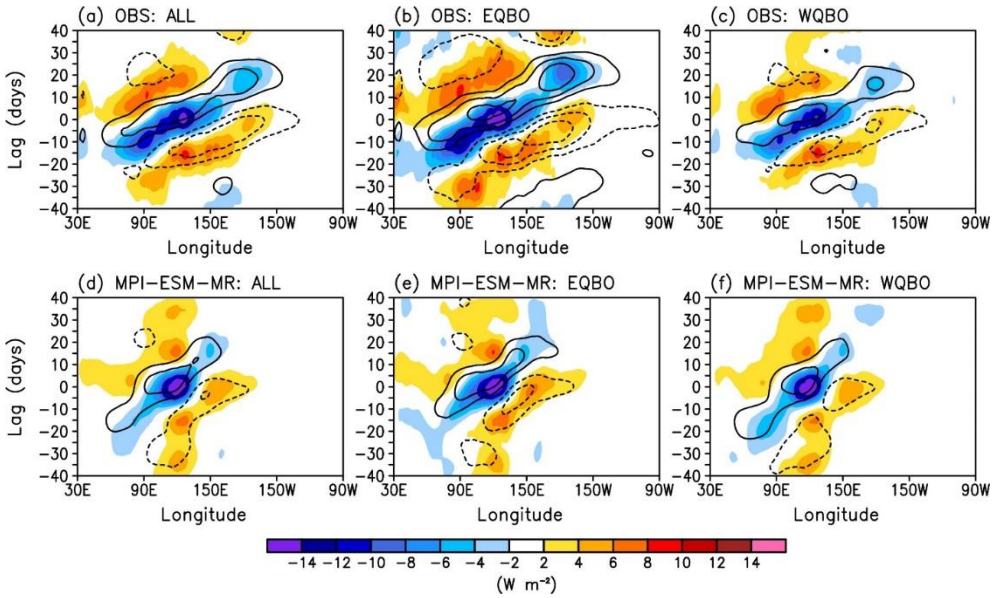

Figure 3.3. Time-lagged-regression of 20-100 day bandpass filtered OLR anomalies (shaded) and 850-hPa zonal wind anomalies (contour interval of 0.4 m s^{-2}) during (left) ALL, (middle) EQBO, and (right) WQBO winters in (a-c) the observation and (d-f) MPI-ESM-MR simulations. OLR and zonal wind anomalies are averaged over 10°S-10°N and regressed onto OLR anomalies averaged over the eastern Indian Ocean (110°-130°E, 10°S-10°N). The regression coefficients are then multiplied by negative one standard deviation of the eastern Indian Ocean OLR anomalies.

Figure 3.4 further illustrates two-dimensional structure of MJO convection and lower-tropospheric wind anomalies. The composites of 20-100 day filtered OLR (shading) and U850 anomalies (contours) are shown for each MJO and QBO phase. Their differences between EQBO and WQBO winters are also shown in the rightmost column where significantly enhanced or suppressed OLR anomalies at the 95% confidence level are contoured. Following Garfinkel et al. (2012), Student's t test is used to test the significance by counting the number of degrees of freedom only when each day in a given phase is separated by at least seven days. It is evident that both OLR and U850 anomalies are stronger during EQBO winters (left) than during WQBO winters (middle). Their differences are statistically significant over the Maritime Continents to western Pacific (contours in the rightmost column). This result confirms an enhanced MJO activity during EQBO winters (e.g., Yoo and Son 2016) even with excluding strong ENSO years.

The same analyses are repeated with the model output as shown in Figs. 3.3d-f and 5. Although weak and not well organized, MJO activities during EQBO winters are slightly stronger than those during WQBO winters (Figs. 3.3e,f). These results are qualitatively similar to the observations, although the EQBO-WQBO differences are much weaker than those in the observations (compare Figs. 3.3a-c with Figs. 3.3d-f).

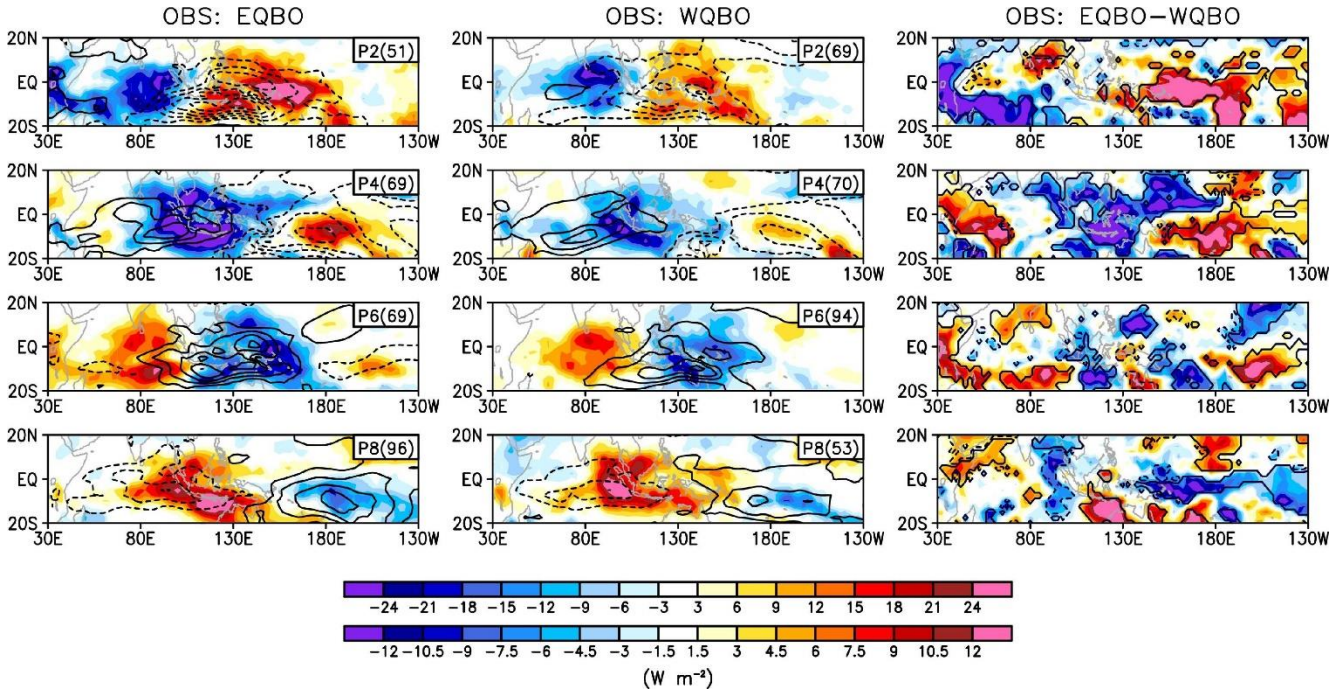

Figure 3.4. Composite of 20-100 day bandpass filtered OLR (shaded) and 850-hPa zonal wind anomalies (contour interval of 1 m s^{-1}; the left two columns) for each MJO phase during (left) EQBO and during (middle) WQBO winters and (right) their difference in the observation. Only days when the MJO amplitude is greater than 1.0 are used, and the number of analyzed days is denoted at the top-right corner of each panel in parenthesis. The values that are statistically significant at the 95% confidence level are contoured in the right column; black for stronger MJO anomalies during EQBO winters, and purple for WQBO winters.

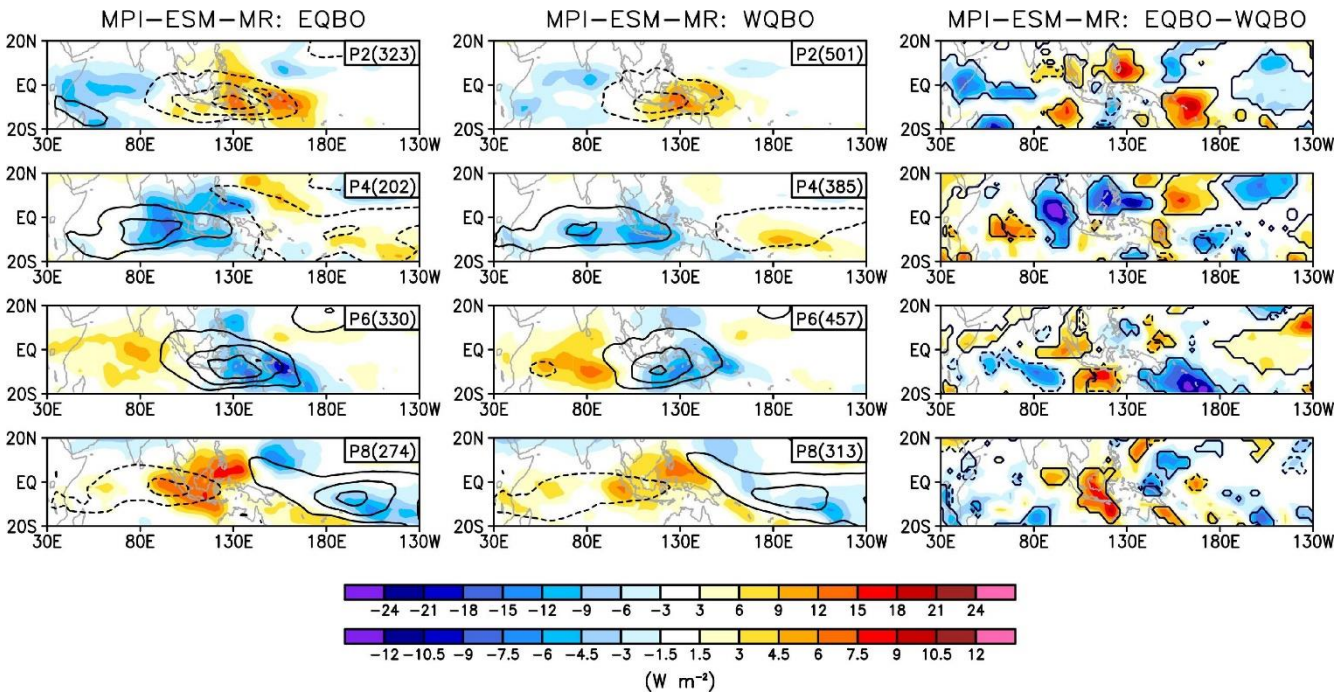

Figure 3.5. Same with Fig. 3.4, but for the MPI-ESM-MR simulations.

A similar result is also found from Fig. 3.5. For most MJO phases, OLR anomalies are slightly stronger during EQBO winters than during WQBO winters (Fig. 3.5). The enhanced negative anomalies are found over the eastern Indian Ocean and the western Pacific during MJO phases 4 and 6. The strengthened positive anomalies are also found from Maritime Continents to the western Pacific (see MJO phases 2 and 8). Consistent with OLR anomalies, U850 anomalies are also slightly stronger during EQBO winters, compared to those during WQBO winters. However, the overall EQBO-WQBO difference in the model is again much smaller than the observation (compare Figs. 3.4 and 3.5).

Figure 3.6 presents the composite RMM amplitudes for each MJO phase. Same with Fig. 3.5, only active MJO days are used. The observation shows that EQBO favors stronger amplitudes over the Maritime Continents and western Pacific (MJO phases 4-7 in Fig. 3.6a) as shown in Zhang and Zhang (2018). In the Indian Ocean (MJO phases 1-3) and central Pacific (MJO phase 8), the RMM amplitude during EQBO winters is stronger or weaker than during WQBO winters but not statistically significant.

The MPI-ESM-MR simulations also show a hint of RMM amplitude difference between EQBO and WQBO winters, but it differs from the observation (Fig. 3.6b). A stronger RMM amplitude is found in MJO phases 7-8 and 1 during EQBO winters. However, RMM amplitude becomes weaker in MJO phases 2-6. This nonsystematic or even opposite result in MJO phases

2-6 indicates that the model simulations do not fully reproduce the observed QBO-MJO connection. This result is partly consistent with Lee and Klingaman (2018).

Note that the RMM amplitude differences are smaller than the OLR and U850 differences (Figs. 3.5 and 3.6). To understand this inconsistency, the RMM amplitude is compared for each variable, as in Kim et al. (2014) (not shown). In general, the RMM amplitude of zonal wind components is distinctively larger than that of OLR, reflecting that the large-scale zonal winds dominate the RMM indices (Straub 2013). It turns out that stronger RMM amplitude in MJO phases 2, 3 and 5 during WQBO winters (Fig. 3.6b) mainly results from U250 anomalies.

The RMM indices do not use the time-filter for the subseasonal timescale and largely depend on the circulation fields. In this regard, the OMI indices, which are only based on the 20-96 day filtered OLR data, are tested for the sensitivity test (Figs. 3.6c-d). In all MJO phases, the OMI amplitude is stronger during EQBO winters not only in the observation but also in the model simulations. The EQBO-WQBO OMI amplitude is still smaller in the model simulations than the observation.

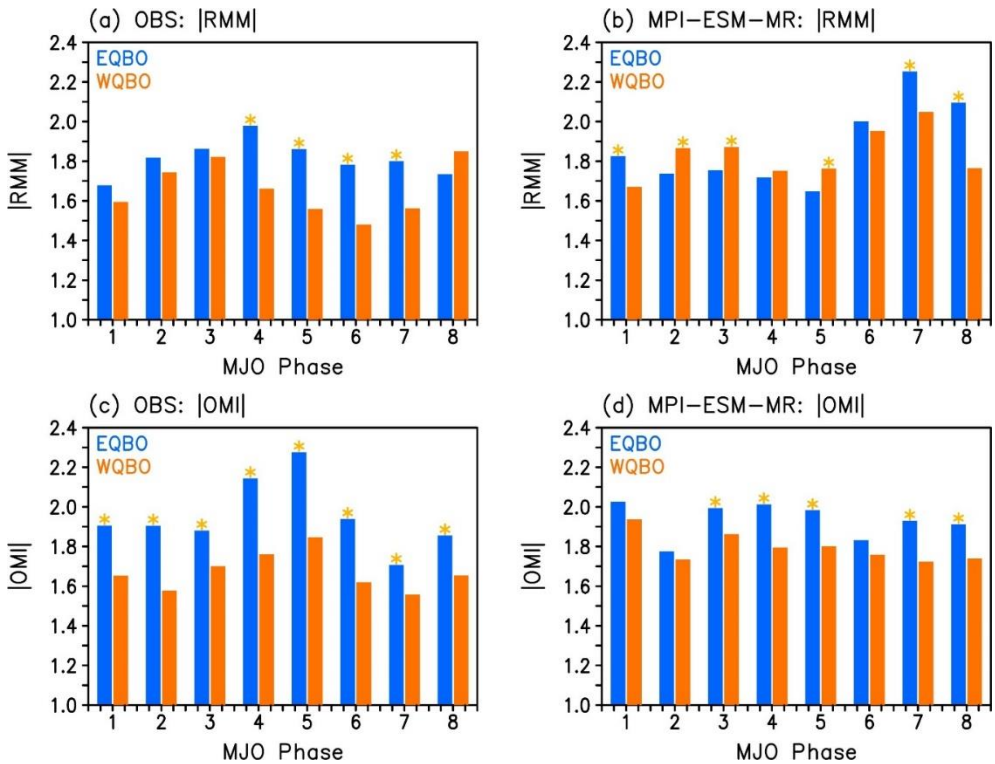

Figure 3.6. RMM amplitude in (a) the observation and (b) MPI-ESM-MR simulations during (blue) EQBO and (red) WQBO winters. The values that are significantly larger in one phase than the other phase are denoted with an asterisk.

The above result suggests that the QBO-MJO connection shown in Figs. 3.3d-f and 3.5 is only marginally significant. This is consistent with Lee and Klingaman (2018). Why does the model have a weak QBO-MJO connection? Collimore et al. (2003) and Yoo and Son (2016) proposed that QBO-induced tropical convection changes are likely mediated by the static stability and vertical wind shear changes in the upper troposphere-lower stratosphere (UTLS; between 200 and 50 hPa). Due to the secondary circulation associated with QBO wind anomalies, the lower stratosphere becomes colder than normal during EQBO winters. The colder (and higher) tropopause and the resulting destabilization in the UTLS could promote organized deep convection. These are pronounced over the active MJO regions and have been proposed to be one of the key factors for the enhanced MJO convection during EQBO winters (Yoo and Son 2016; Son et al. 2017; Hendon and Abhik 2018; Martin et al. 2019; also in Sect. 2.3.5). Additionally, Hendon and Abhik (2018) focuses on the cold cap above the enhanced MJO convection, which is associated with a vertically propagating Kelvin wave (e.g., Kiladis et al. 2005; Ryu et al. 2008). Hendon and Abhik (2018) suggests that the stronger and more stretched cold cap during EQBO winters may further enhance the MJO convection and slow down the MJO propagation.

Figure 3.7a shows the difference in zonal-mean zonal wind and temperature anomalies between EQBO and WQBO winters in the observation. The maximum difference in zonal-mean zonal wind is located at 50 hPa. Due

to the thermal wind balance, the anomalous adiabatic cooling and warming are shown below and above 50 hPa, respectively. A similar structure also appears in the model simulations (Fig. 3.7d). However, overall magnitudes are much weaker than the observation. Considering the fact that the QBO-MJO connection may depend on the magnitude of the QBO temperature anomaly (Martin et al. 2019), a weaker temperature anomaly in the model may result in an underestimation of the QBO-MJO connection.

Figures 3.7b-c and e-f further illustrate the zonal wind and temperature profile averaged over the active MJO region (60°-180°E, 5°S-5°N) in the observation and the model simulations. It turns out that the EQBO-WQBO temperature difference in the model, which is approximately -1.6 K at 70 hPa, is much weaker than in the observation (approximately -3 K). For the zonal wind, the EQBO-WQBO differences are 25 m s^{-1} and 18 m s^{-1} at 50 hPa in the observation and the model simulations. The temperature and zonal wind responses are underestimated by 50% and 25% than the observation, respectively. In terms of relative change, this result indicates that the QBO-related temperature change is weaker than the zonal wind change in the model.

A larger underestimation in the temperature, compared to the zonal wind, gives a hint for why the QBO-MJO connection is underestimated in the model. It is well documented that the QBO-induced temperature anomalies are determined not only by the adiabatic process but also by the diabatic

process associated with the water vapor and ozone changes. Among others, QBO-induced ozone change can effectively modulate the shortwave radiation in the lower stratosphere. When the easterly shear zone with upward motion is dominant, the vertical advection of ozone-poor air from the upper troposphere to the lower stratosphere results in the anomalously cold region in the tropical lower stratosphere. Due to the feedback process, the ozone-induced temperature changes further affect the QBO secondary circulation. This indicates that weaker temperature response than zonal wind response, shown in Figs. 3.7e-f, could be partly attributed to ozone transport, which is absent in the model. In fact, it is shown that the diabatic heating related to the ozone QBO in the coupled chemistry models enhanced their modeled temperature QBO by 25~35%, relative to the uncoupled chemistry models (Li et al. 1995; Butchart et al. 2003; Tian et al. 2006).

It was also suggested that QBO-induced cirrus change could affect the QBO-MJO connection (Son et al. 2017). During EQBO winters, cirrus clouds in the tropical tropopause layer become broader, possibly resulting in the radiative warming in the upper troposphere (Hartmann et al. 2001; Yang et al., 2010; Hong et al. 2016). This may help the UTLS destabilization. However, the longwave radiation in the model does not change much during the QBO winters. The rather weak negative temperature anomalies during EQBO winters appear below 150 hPa. This result may indicate that not only dynamical processes but also diabatic processes in the UTLS are not well

represented in the model.

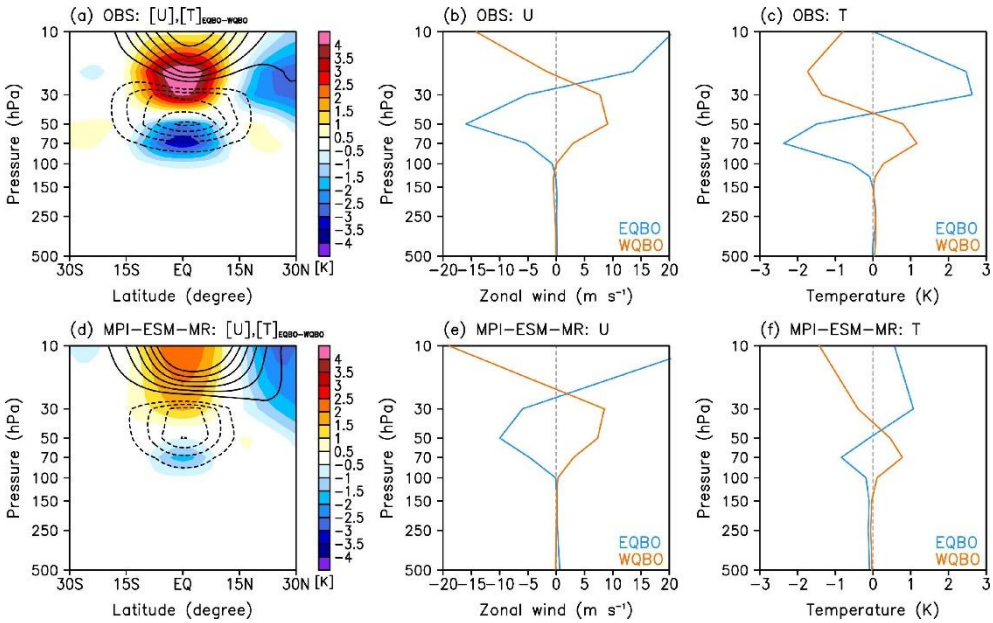

Figure 3.7. (a, d) Difference in zonal-mean zonal wind (contoured) and temperature (shaded) anomalies between EQBO and WQBO winters in the observation and MPI-ESM-MR simulations. The contour intervals are 5 m s^{-1}. (b, e) Zonal wind and (c, f) temperature anomalies averaged over the MJO active region (60°-180°E, 5°S-5°N) during EQBO (blue) and WQBO (orange) winters.

Hendon and Abhik (2018) argued that zonally asymmetric temperature change is more important than zonal-mean temperature change. Figures 3.8a-b present the 20-100 day bandpass filtered temperature anomalies over the tropics (10°S-10°N) as a function of longitude and pressure. The anomalies in MJO phase 4 for each QBO phase are representatively shown for the observation. A stronger diabatic warming in the troposphere and a stronger cold cap near the tropopause are found during EQBO winters than during WQBO winters, consistent with Hendon and Abhik (2018).

The model simulations qualitatively capture a dipolar temperature change (Figs. 3.8c-d). However, due to the weaker MJO convection in the model simulations (i.e., Figs. 3.3d-f, 3.5, and 3.6), the diabatic heating in the troposphere is generally weaker than the observation especially during EQBO winters. This causes relatively small differences in the overriding cold cap between EQBO and WQBO winters (Figs. 3.8c-d) than in the observation (Figs. 3.8a-b). Considering the fact that the cold cap can be strengthened by the enhanced static stability near the tropopause (Ryu et al. 2008), smaller cold cap differences could be also attributed to the weak QBO-related static stability change in the model simulations (Fig. 3.7). A weak cold cap change may reduce its impact on the MJO convection, although the feedback process requires to be further understood by a modeling study.

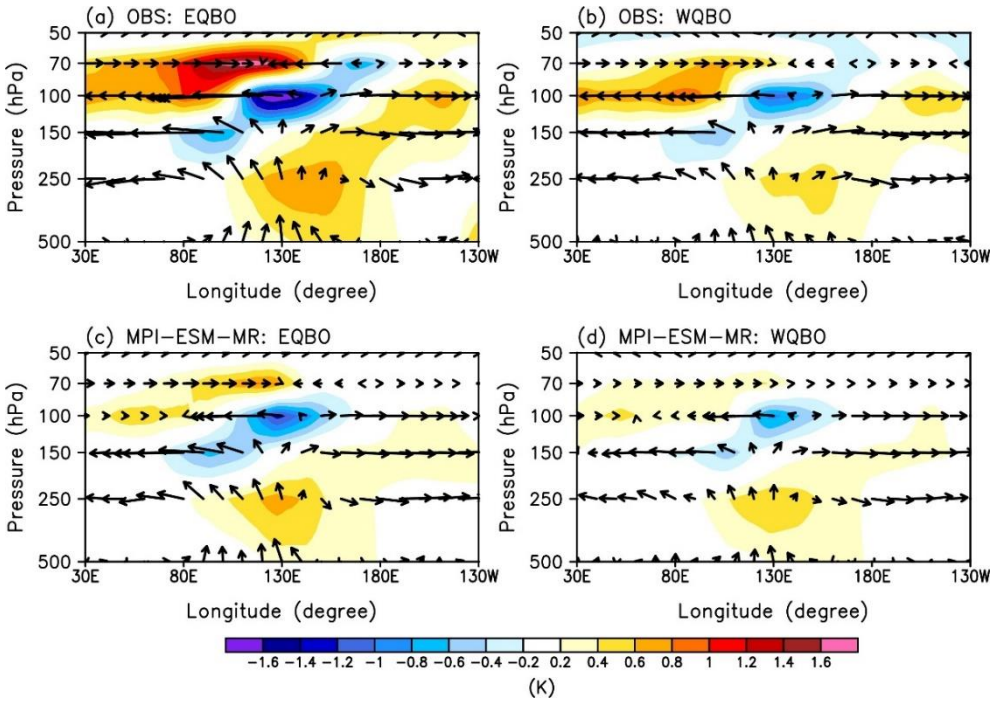

Figure 3.8. Composite of 20-100 day bandpass filtered temperature (shaded) and zonal-vertical wind anomalies (vectors) for MJO phase 4 during (left) EQBO and during (right) WQBO winters in (top) the observation and (bottom) the model simulations. Only days when the MJO amplitude is greater than 1.0 are used.

Chapter 4. Dynamical mechanism of the QBO on the MJO

This chapter examines whether the QBO can dynamically influence the MJO structure, based on a primitive equation model. The model description and experiment design are described in Sect. 4.1. The results and possible mechanism are discussed in Sect. 4.2.

4.1. Model description and experiment design

The numerical model used in this study is the primitive equation model based on the dry dynamical core of the Geophyical Fluid Dynamics Laboratory general circulation model (Feldstein 1994; Kim and Lee 2001; Son et al. 2005; Ryu et al. 2008). Rhomboidal 30 resolution is used and there is no topography. The vertical levels are defined in sigma coordinates. There are 75 levels, starting from 0.975 near the surface up to 0.0001. To accurately resolve upper-troposphere – lower stratosphere features, more fine vertical resolution is used from 500 hPa. The vertical resolution in the middle to upper troposphere is approximately 10 hPa, and that in the lower stratosphere is 5 hPa (marked in Fig. 4.1). Note that the weakly nonlinear solution is convergent if more than 15 vertical levels and a horizontal resolution greater than rhomboidal 30 is used (Feldstein 1994).

To evaluate the impact of the QBO-related background state, EQBO- and WQBO-like background state are defined as follows. The zonal wind, meridional wind, temperature, and surface pressure fields from ERA-Interim

are averaged for 10 EQBO years, defined in Chap. 2, and then used as EQBO-like background state. The WQBO-like background state is defined by calculating the departure of EQBO-like background state from the DJF-mean climatology and then excluding them from the climatology, to have a same amount but opposite forcing with EQBO-like background state. To focus on the impact of the upper troposphere and lower stratosphere, the background state above 250 hPa is only changed. Figure 4.1 shows the vertical profiles of zonal-mean zonal wind and temperature in EQBO and WQBO experiments, respectively.

Even though the background state is defined as the time-mean values, it is still not balanced. Following Franzke et al. (2004), a time-independent additional forcing is added to the model equations to obtain a balanced state. This additional forcing is calculated by initializing the model with the background state and then by integrating forward in time by a one-time step. Their residual term at the one-time step is used for the additional forcing and is added in all time steps.

For the MJO-like dipole heating, an elliptic horizontal distribution is used, which is similar to Seo and Son (2012). One is diabatic heating for mimicking the enhanced convection and the other is diabatic cooling for the suppressed convection. Similar to the MJO phase 3 heating, the enhanced heating field, which is centered at 100°E and the equator, is shown in Fig. 4.2. The zonal and meridional extents of the heating are 25° and 10° with the

maximum value of 5.0 K day-1 at $\sigma = 0.450$. The vertical profile of the heating takes the form of Yoo et al. (2012). Likewise, the suppressed convection like heating is centered at 160°E and the equator, and the minimum value of -5.0 K day^{-1} at $\sigma = 0.450$, shown in Fig. 4.2a.

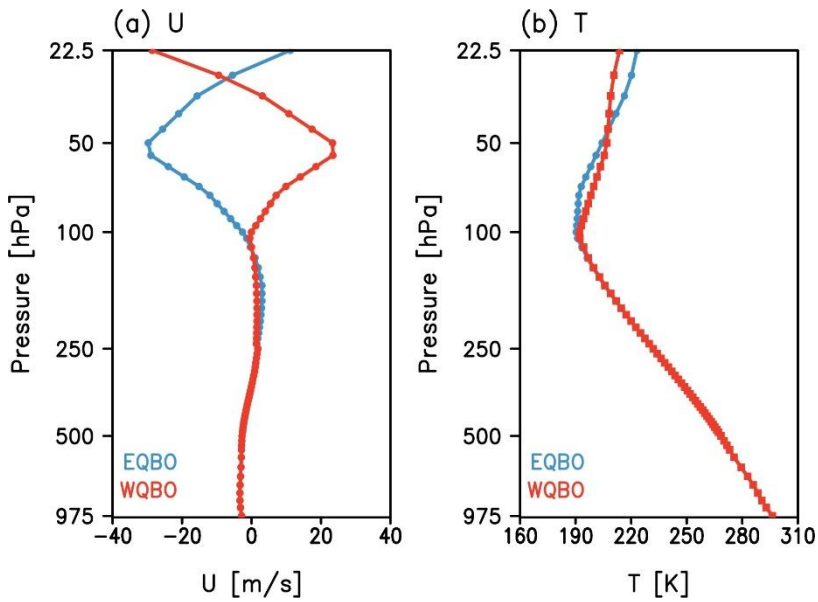

Figure 4.1. (a) The zonal-mean zonal wind and (b) temperature averaged over the tropics (10°S-10°N) used in EQBO (blue) and WQBO (red) experiments.

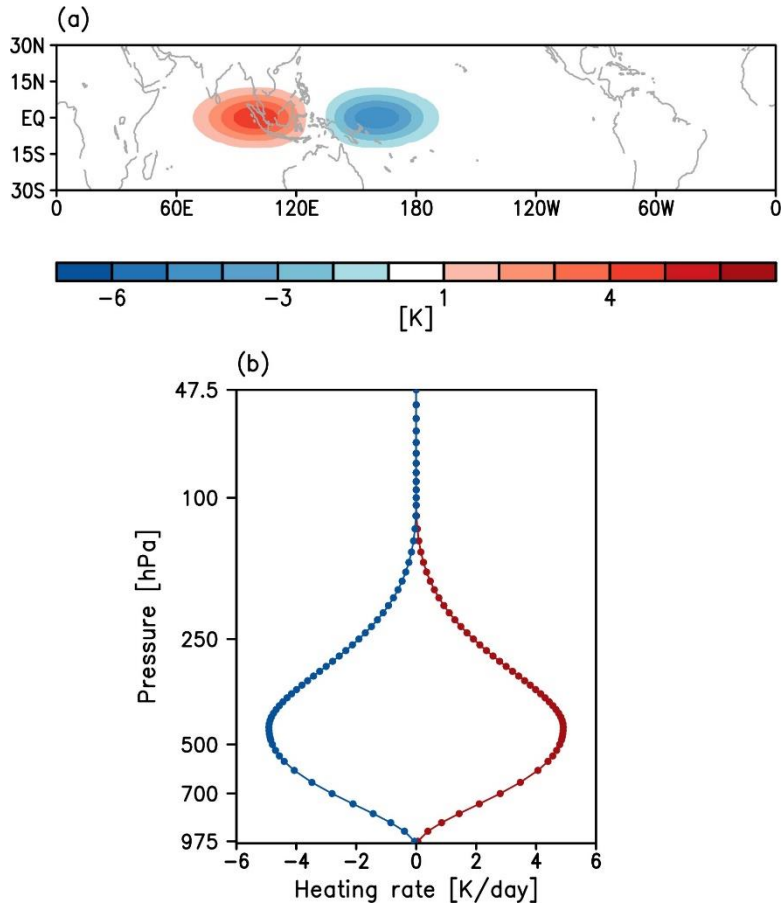

Figure 4.2. (a) The horizontal structure of the idealized heating and cooling at 450 hPa. (b) The vertical profile of the idealized heating at 100°E and cooling at 160°E, respectively. The closed circles indicate each vertical level defined in the model.

4.2. Model results

Figure 4.3 displays the temperature anomalies averaged over the tropics (10°S-10°N) at day 3, 6, and 9 in EQBO and WQBO experiments (left two columns in Fig. 4.3). The MJO-related temperature vertical structure is partly captured in the dynamical core model. The upper tropospheric heating induced by the thermal forcing is presented and is centered to the east of thermal forcing (see also Fig. 3.8). It results from the easterly winds in the background states. Above the tropospheric heating, the vertically eastward tilted cold anomaly is shown. The cold anomaly has been demonstrated by the result from the hydrostatic adjustment to maintain hydrostatic balance in response to the diabatic warming related to the tropical deep convection (Holloway and Neelin 2007; Hendon and Abhik 2018). With time integration, the warm anomaly is developed above the cold anomaly, which is known as the vertically propagating equatorial Kelvin wave (e.g., Kiladis et al. 2001). These cold regions above the tropospheric heating have been called for "cold cap" (e.g., Hendon and Abhik 2018).

Comparing the cold cap responses between EQBO and WQBO experiments, the cold cap in the EQBO experiment is more vertically stretched with a longer vertical scale. It is colder at near 100 hPa than that in the WQBO experiment, based on the -1.6 K value. More quantitatively, the rightmost column of Fig. 4.3 reveals the vertical temperature profile over the minimum cold region at near 100 hPa (110°-130°E, 10°S-10°N; solid lines).

The vertical profile over the maximum warm region (180°-160°W, 10°S-10°N) is indicated by dotted line. The EQBO-WQBO difference increases with time integration, and their difference is about -0.5 K on day 9. This result indicates that the cold cap response can be intensified up to 28 % only by dynamic process.

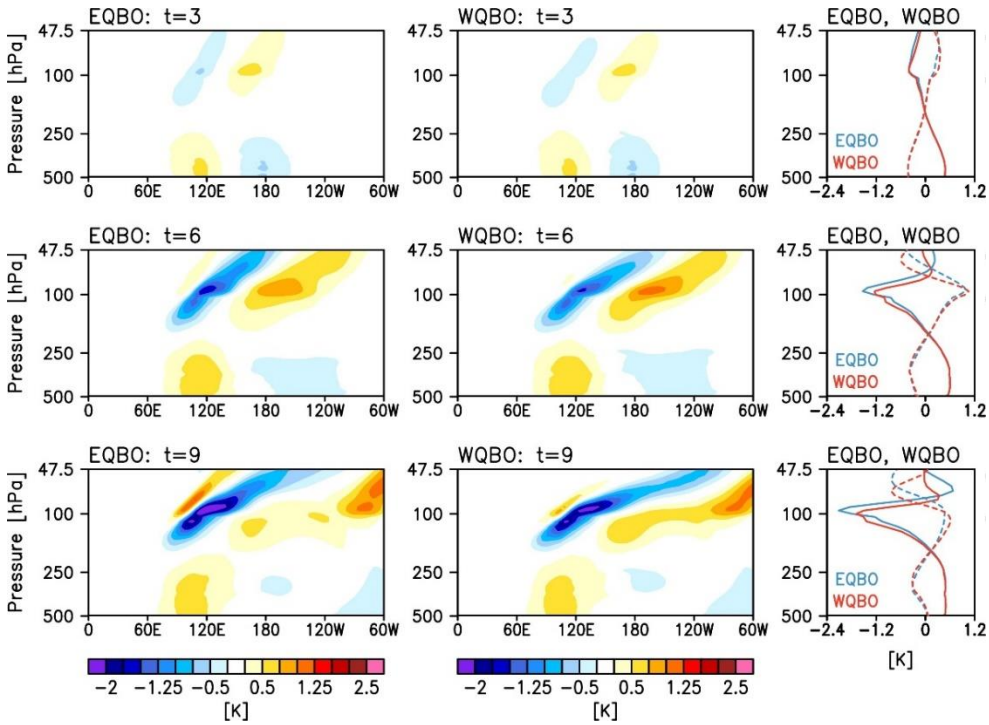

Figure 4.3. Longitude-height cross section of perturbed temperature, generated in (left) EQBO and (middle) WQBO experiments at (top to bottom) day 3, 6, and 9. The vertical profile of temperature averaged over two regions (110°-130°E, 10°S-10°N and 180°-160°W, 10°S-10°N) are denoted by solid and dotted lines, respectively in the rightmost column. The blue (red) lines indicate the results from EQBO (WQBO) experiment.

To further investigate the importance of the QBO-like background state in the cold cap changes, the dependency on the QBO amplitude is examined. Figure 4.4 shows the vertical temperature profile averaged over the cold cap region, which is the same with the rightmost column in Fig. 4.3, but the results are obtained in 2xEQBO, 3xEQBO, 2xWQBO, and 3xWQBO experiments. Regardless of the QBO amplitude, the cold cap responses in EQBO-like experiments are colder than those in WQBO-like experiments. In each QBO experiment, the cold cap responses to the QBO amplitude are slightly different. When the easterly winds become stronger in the EQBO-like experiments, the height of the minimum temperature moves upward and its magnitude becomes colder. On the contrary, when the westerly winds become stronger in the WQBO-like experiments, the height of the minimum temperature moves downward, but its magnitude is not changed.

The thermal response to the QBO background state is sensitive to the location of thermal forcing. The warm cap response overlying the tropospheric cooling in central Pacific is different from the cold cap. The magnitude of the temperature anomaly is distinctively weaker than that in the western Pacific. This result is consistent with the results from Ryu et al. (2008), which shows that the strongest Kelvin wave response occurs over the western Pacific. This result might provide a hint for how the QBO-MJO connection is well presented, especially in the western Pacific.

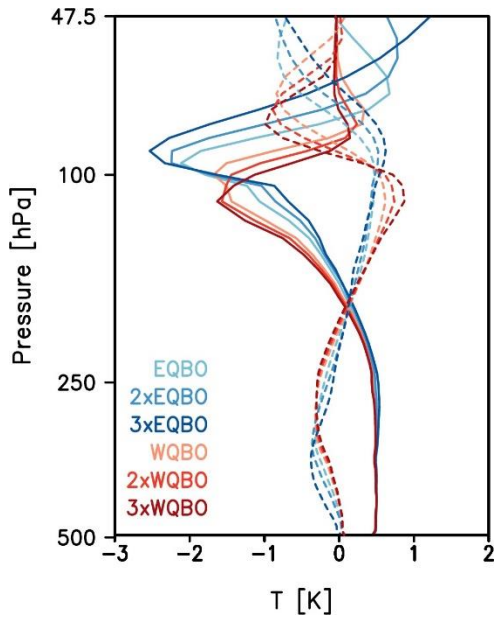

Figure 4.4. Same with the right bottom of Fig. 4.3. The results from EQBO, 2xEQBO, 3xEQBO, WQBO, 2xWQBO, and 3xWQBO experiments are additionally shown.

How does the QBO modulate the Kelvin wave? We try to understand the cold cap response, based on the characteristics of Kelvin wave in linear wave theory. The dispersion relation of Kelvin wave is written as below (Andrews et al. 1987).

$$\omega = \pm Nk/m \tag{4.1}$$

ω is absolute wave frequency, k and m are zonal and vertical wavenumber, respectively. N is background buoyancy frequency. The zonal and vertical group velocities of the Kelvin wave are as follows.

$$C_{gx} = \frac{\partial \omega}{\partial k} = \pm \frac{N}{m}, \tag{4.2}$$

$$C_{gz} = \frac{\partial \omega}{\partial m} = \mp \frac{Nk}{m^2} \tag{4.3}$$

For our convention, k is positive. The Kelvin wave propagates upward from the troposphere, and thus C_{gz} is positive. Therefore, the zonal and vertical group velocities are rewritten as $C_{gx} = -N/m$ and $C_{gz} = Nk/m^2$. As the Kelvin wave propagates eastward, m should be negative. Since the background zonal wind is nonzero and constant, the Doppler-shifted frequency is considered, and therefore the group velocities are $C_{gx} = U - N/m$ and $C_{gz} = Nk/m^2$. The group velocity is determined by the background state.

Based on the fact that more energy is transported when the group velocity is faster, we hypothesize that the weaker temperature perturbation is formed due to smaller energy. If the WQBO background state contributes to

the faster group velocity, it results in the weaker cold cap response. Figures 4.4 and 4.5 show the zonal and vertical group velocity in each QBO experiments, respectively. Following Ryu et al. (2008), the value of k is 1.57 x 10^{-7} m^{-1}, corresponding to zonal wavenumber 1 of Kelvin wave. Considering that the vertical scale of the Kelvin wave in EQBO experiment is larger, we calculate the group velocity with two vertical scales (i.e., 8 and 10 km). The structure of C_{gx} follows the distribution of zonal wind, and the structure of C_{gz} follows the distribution of buoyancy frequency, consistent with Ryu et al. (2008). The C_{gx} in the UTLS is slower in EQBO experiments regardless of the vertical scale. The C_{gz} is smaller in EQBO than WQBO experiments, but their difference is very small relative to that in C_{gx}. Based on the facts that the C_{gx} is distinctively larger than C_{gz} (cf. Figs. 4.5 and 4.6) and the C_{gx} in EQBO-like background state is weaker than that in WQBO-like background state, we can conclude that the stronger cold cap during EQBO is demonstrated by the Doppler-shift effect.

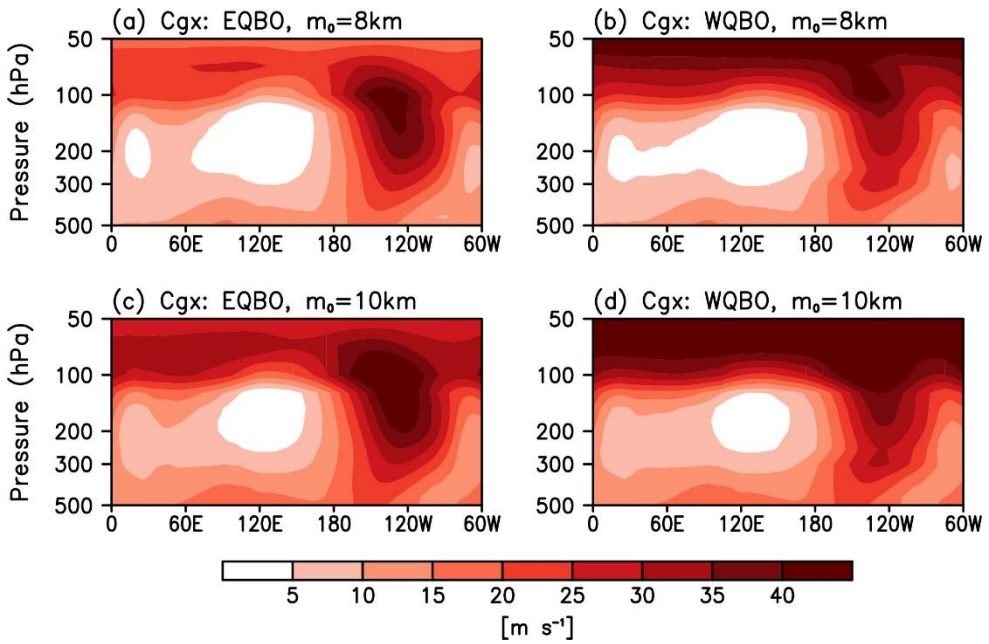

Figure 4.5. Longitude-height cross section of the zonal Kelvin wave group velocity in (a,c) EQBO and (b,d) WQBO experiments. The expected values with two different vertical scales (i.e., 8 and 10 km) are presented in top and bottom, respectively.

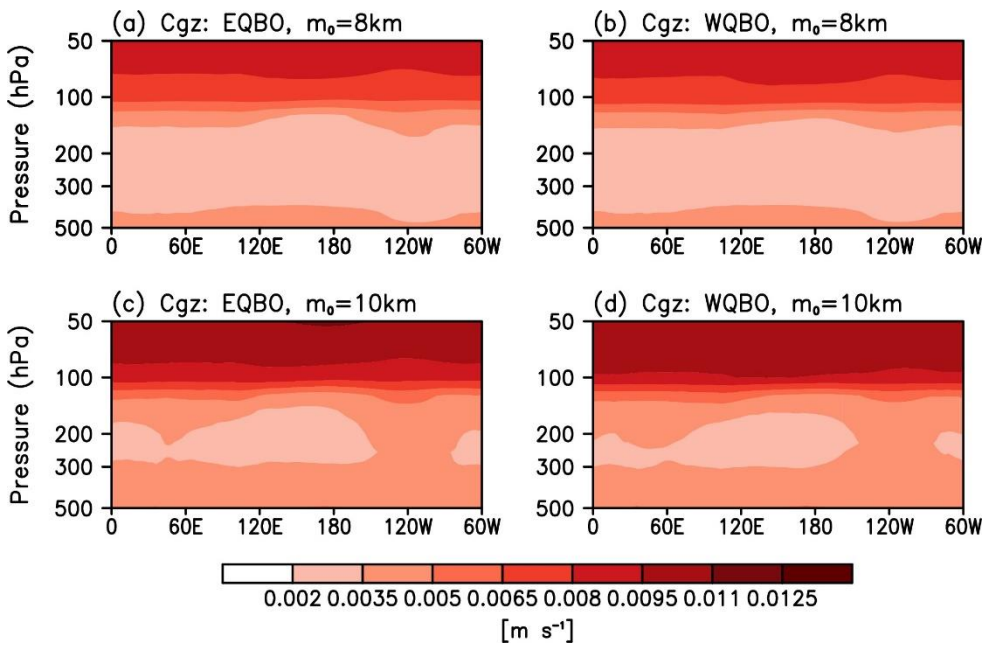

Figure 4.6. Same with Fig. 4.5, but for the vertical Kelvin wave group velocity.

Chapter 5. QBO-MJO connection in the S2S prediction models

This chapter is to examine the robustness of the QBO modulation of MJO prediction skill in a range of operational forecast models. The S2S models (Vitart et al. 2017), verification data, and methods are described in Sect. 5.1. After briefly evaluating the QBO prediction skill in Sect. 5.2, the QBO impact on MJO prediction skill is quantified by using various MJO evaluation metrics in Sect. 5.3. Potential causes of the different MJO prediction skills between EQBO and WQBO winters are also analyzed.

5.1. Data and methods

5.1.1. Data

As a reference, daily zonal wind from ERA-Interim reanalysis data (Dee et al. 2011) are used. These data are utilized to define the QBO phase and MJO index. NOAA OLR data (Liebmann and Smith 1996) are also used to describe tropical convective activity. Since NOAA OLR data are available only up to 2013 (as of February 2017), the maximum evaluation period is from 1981 to 2013. Based on the 2.5° × 2.5° resolution of NOAA OLR data, all datasets, including model output, are interpolated into a common horizontal resolution of 2.5° × 2.5°.

Almost all reforecasts during boreal winter months are considered. As of February 2017, reforecasts are available in the S2S archive from BoM,

CMA, Institute of Atmospheric Sciences and Climate of the National Research Council (CNR-ISAC), Météo-France/Centre National de Recherches Météorologiques (CNRM), Environment and Climate Change Canada (ECCC), ECMWF, Hydrometeorological Centre of Russia (HMCR), JMA, NCEP, and United Kingdom Met Office (UKMO) models (Table 5.1). As summarized in Table 5.1, each model has a different resolution. The reforecast frequency and length are also appreciably different among the models. Note that Table 5.1 is identical to the data used in Chap. 6, except that MJO events initialized only in December–February (DJF) are considered. These three months are chosen because the QBO–MJO link is stronger in DJF than in the extended winter (Yoo and Son 2016). Because of the unavailability of OLR data since 2014, the reforecasts initialized in December 2013 are not examined.

All available reforecasts are used. Exceptions are the CMA and NCEP models, which are initialized every day. Due to a storage issue, the reforecasts of these two models are subsampled six times per month (initialized on the 1st, 6th, 11th, 16th, 21st, and 26th), similar to the reforecast frequency of the BoM model. Since each reforecast is integrated for at least 31 days, MJO activity in March is included in the MJO events initialized in February.

In Table 5.1, it is important to note that not all models resolve the stratosphere. Based on the model top at and above 1 hPa, only six models (i.e.,

CMA, CNRM, ECMWF, JMA, NCEP, and UKMO models) have a reasonable vertical resolution in the stratosphere. These six models are referred to as high-top models, while the other four models (i.e., BoM, CNR-ISAC, ECCC, and HMCR models) are referred to as low-top models (Table 5.2). However, even low-top models have a realistic initial condition in the stratosphere because all models are initialized with reanalysis data.

The QBO index is defined by 50-hPa zonal-mean zonal wind anomalies over the tropics (10°S–10°N), following previous studies (e.g., Yoo and Son 2016; Marshall et al. 2017; Son et al. 2017; Same with Chap. 2-4). When the DJF QBO index is above 0.5 standard deviation (approximately 5 m s^{-1}), it is defined as WQBO winter. Similarly, EQBO winter is defined when the index is less than -0.5 standard deviation. The selected QBO years are denoted by a triangle in Fig. 5.1. For the analysis period from January 1981 to February 2013, a total of 9 and 15 years are defined as EQBO and WQBO winters, respectively. Each S2S model has a different number of QBO winters due to the different reforecast periods (third column in Table 5.1). For instance, the number of WQBO winters ranges from 5 years in the NCEP model to 15 years in the BoM model. Likewise, the number of EQBO winters ranges from 5 years in the NCEP model to 9 years in the BoM model. Due to this sampling issue, the detailed comparisons between EQBO and WQBO winters are primarily conducted using only seven models that have large samples (indicated by a superscript "+" in Table 5.1).

Properties of the MJO, such as amplitude and phase, can be quantified by the RMM indices (Wheeler and Hendon 2004). The RMM indices are calculated in reforecasts and observations following previous studies (e.g., Gottschalck et al. 2010; Vitart 2017; Lim et al. 2018). Briefly, the RMM indices are derived from observed and forecasted OLR, 200 hPa (U200), and 850 hPa zonal winds (U850) averaged over the deep tropics (15°S–15°N). The seasonal cycle is removed using the daily climatology from observations and from the lead-time dependent climatology of the reforecasts. The previous 120-day averaged data are also removed to isolate intraseasonal variability, and each field is normalized by the square root of the area-mean variance. The first two empirical orthogonal functions (EOFs) are then obtained from a combined EOF analysis of the OLR, U200 and U850 using the observations. The observed and predicted RMM indices are computed by projecting the normalized observed and reforecast fields onto the first two observed EOFs.

For each model, the RMM indices are averaged across all available ensemble members that are initialized on the same day. As described in Lim et al. (2018) and Table 5.1, the ensemble size of each model substantially differs from 1 to 33. Since our goal is to examine the QBO-dependent MJO prediction skill, only the ensemble-mean MJO prediction skill is evaluated.

Table 5.1. Description of the S2S models used in Chap. 5. The models used in Sect. 5.3 are indicated by cross. The models used in Sect. 6.3 are denoted by pound. The CMA and NCEP models, denoted with asterisk, are sub-sampled to be compared with other models. Note that ECMWF's horizontal resolution is switched from Tl 639 to Tl 319 after forecast day 15.

Modeling center	Model resolution (Top of model)	Reforecast Period	Reforecast frequency	Total number of reforecasts (ALL/EQBO/WQBO)	Reforecast length	Ensemble size
BoM$^{+\#}$	T47 L17 (10 hPa)	1981-2013	six times/month	588/162/264	Days 1-62	33
CMA*$^{+\#}$	T106 L40 (0.5 hPa)	1994-2013	six times/month	354/126/156	Days 1-60	4
CNR-ISAC^{+}	0.75°x0.56° L54 (roughly 6.8 hPa)	1981-2010	every 5 days	540/144/242	Days 1-31	1
CNRM$^{\#}$	T255 L91 (0.01 hPa)	1993-2013	twice/month	124/42/54	Days 1-61	15
ECCC$^{+\#}$	0.45°x0.45° L40 (2 hPa)	1995-2013	weekly	242/91/104	Days 1-32	4
ECMWF$^{+\#}$	Tl639/319 L91 (0.01 hPa)	1996-2013	twice/week	424/168/184	Days 1-46	11
HMCR^{+}	1.1°x1.4° L28 (5 hPa)	1985-2010	weekly	338/99/156	Days 1-61	10
JMA$^{+\#}$	T319 L60 (0.1 hPa)	1981-2010	three times/month	270/72/123	Days 1-34	5
NCEP*$^{\#}$	T126 L64 (0.02 hPa)	1999-2010	six times/month	216/84/90	Days 1-44	4
UKMO	N216L85 (85 km)	1996-2009	four times/month	168/72/72	Days 1-60	3

5.1.2. Evaluation metrics

The MJO prediction skill is evaluated by computing the bivariate anomaly correlation coefficient (BCOR):

$$\mathrm{BCOR}(\tau) = \frac{\sum_{t=1}^{N}[O_1(t)M_1(t,\tau) + O_2(t)M_2(t,\tau)]}{\sqrt{\sum_{t=1}^{N}[O_1^2(t) + O_2^2(t)]}\sqrt{\sum_{t=1}^{N}[M_1^2(t,\tau) + M_2^2(t,\tau)]}} \quad (5.1)$$

Here, $O_1(t)$ and $O_2(t)$ are the verification of RMM1 and RMM2 at time t, and $M_1(t,\tau)$ and $M_2(t,\tau)$ are the respective ensemble-mean reforecasts for time t for a lead time of τ days. N is the number of reforecasts. Following previous studies (e.g., Lin et al. 2008; Rashid et al. 2011; Lim et al. 2018), MJO prediction is representatively judged to be skillful when BCOR ≥ 0.5. The values of 0.6, 0.7, and 0.8 are also used for the sensitivity tests. In all analyses, only organized MJO events with initial amplitude larger than 1.0 are considered.

In order to understand the relative importance of MJO amplitude and phase errors, the mean-squared amplitude errors ($\overline{\mathrm{AE}^2}$) and mean-squared phase errors ($\overline{\mathrm{PE}^2}$), which are closely related to BCOR skills (Lim et al. 2018), are also computed. The $\overline{\mathrm{AE}^2}$ and $\overline{\mathrm{PE}^2}$ are defined as below.

$$\overline{\mathrm{AE}^2}(\tau) = \frac{1}{N}\sum_{t=1}^{N}[A_M(t,\tau) - A_O(t)]^2, \quad (5.2)$$

$$\overline{\mathrm{PE}^2}(\tau) = \frac{1}{N}\sum_{t=1}^{N}[\phi_M(t,\tau) - \phi_O(t)]^2. \quad (5.3)$$

Here, A_O, A_M, ϕ_O, and ϕ_M are the observed and forecasted MJO amplitudes and phases in the RMM space, and are defined by

$$A_O(t) = \sqrt{O_1^2(t) + O_2^2(t)}, \qquad A_M(t,\tau) = \sqrt{M_1^2(t,\tau) + M_2^2(t,\tau)},$$

$$\phi_O(t) = tan^{-1}\left(\frac{O_2(t)}{O_1(t)}\right), \qquad \text{and} \qquad \phi_M(t,\tau) = tan^{-1}\left(\frac{M_2(t,\tau)}{M_1(t,\tau)}\right).$$

5.2. QBO prediction skill in S2S prediction models

The time series of the daily QBO indices from ERA-Interim and those from the reforecasts are illustrated in Fig. 5.1. Here, to smooth the times series, a 30-day average is applied. Long-term climatology is then removed. For instance, the observed or predicted QBO index on 1 January 1981 represents 50-hPa zonal-mean zonal wind anomalies averaged over 30 days from 1 to 30 January 1981.

All S2S models show a realistic alternation of 50-hPa zonal wind anomalies from easterlies to westerlies (Fig. 5.1). The correlation coefficient (COR) and root-mean-squared error (RMSE) with respect to ERA-Interim are reasonably small (Table 5.2). The low-top models generally underestimate the QBO in comparisons to the high-top models (Table 5.2). Among them, the BoM model exhibits the largest underestimation of the QBO amplitude in terms of the absolute value of the QBO index (Table 5.2). The low vertical resolution (i.e., 17 levels with only 4 levels above 100 hPa) and its low model top (i.e., 10 hPa) likely cause a rapid and significant reduction in stratospheric

wind anomalies during the forecast (Table 5.2; Marshall et al. 2017). The HMCR model has the second lowest vertical resolution (28 levels with 7 levels above 100 hPa), followed by the CMA and ECCC models. The QBO amplitude of this model is somewhat larger than the CMA and ECCC models, but its variation is less well correlated with the observation (Table 5.2). However, COR is still greater than 0.90. This good performance simply results from the fact that all models are initialized with reanalysis data.

The S2S models, except the BoM and HMCR models, can be largely divided into three groups according to QBO amplitude. The three European models (CNRM, ECMWF and UKMO models) show the largest QBO amplitude and closest agreement to ERA-Interim (RMSE < 2 m s^{-1} in Table 5.2), while the JMA and NCEP models show a moderate QBO amplitude (2 m s^{-1} < RMSE < 3 m s^{-1}). The remaining three models (CMA, CNR-ISAC and ECCC models) show a relatively weak QBO amplitude (RMSE > 4 m s^{-1}). The difference between the first two groups may not be physically meaningful because they used different initial conditions. The initial condition of the first group is ERA-Interim but that of the second group is either Japanese 55-year Reanalysis (JRA-55) or Climate Forecast System Reanalysis. The CMA model in the third group used the NCEP-NCAR Reanalysis as an initial condition.

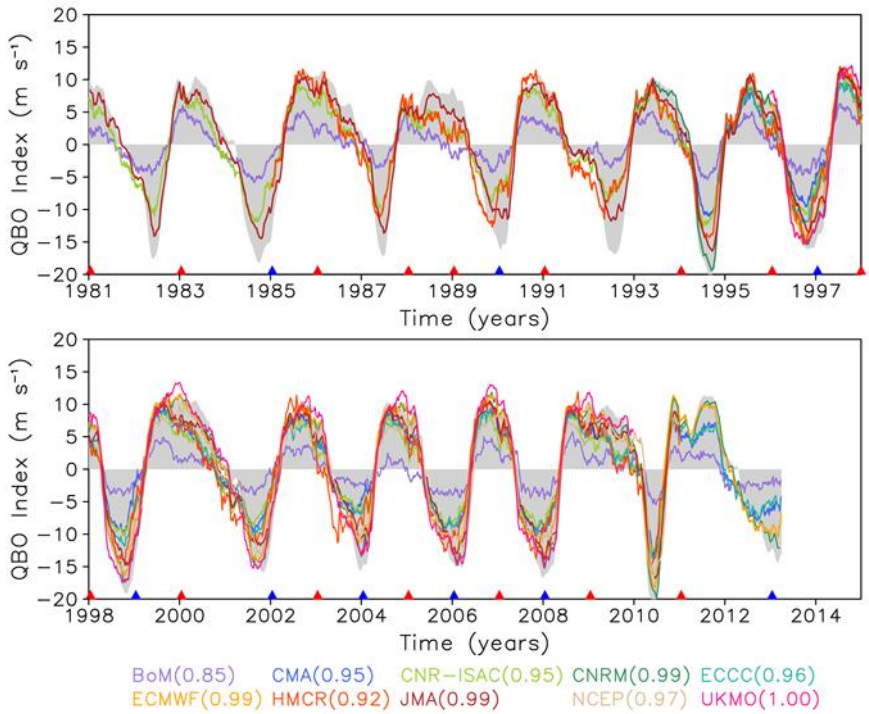

Figure 5.1. Time series of U50 QBO index from ERA-Interim (gray shading) and one-month predictions of each model (colored lines). Blue and red triangles indicate EQBO and WQBO winters, respectively. The correlation coefficient between ERA-Interim and each model (same with the second column in Table 5.2) is indicated in parenthesis.

Table 5.2. One-month QBO prediction skill of the S2S models. The high-top models are denoted with circumflex accent.

All	COR	RMSE
BoM	0.85	7.44
CMA^	0.95	4.63
CNR-ISAC	0.95	4.51
CNRM^	0.99	1.34
ECCC	0.96	3.99
ECMWF^	0.99	1.94
HMCR	0.92	4.07
JMA^	0.99	2.54
NCEP^	0.97	2.85
UKMO^	1.00	0.76

Although the CNR-ISAC and ECCC models use ERA-Interim as an initial condition, the QBO amplitudes are weaker than the others. The underestimation of the QBO amplitude seems to be related to their vertical resolution which is relatively coarse (Table 5.2). It is known that a fine vertical resolution (less than 1 km) is necessary to capture the gravity wave breaking and the associated momentum deposit in the stratosphere which drive the QBO (Kim et al. 2013a; Schmidt et al. 2013). Geller et al. (2016) also documented that sufficient vertical resolution is required for the downward propagation of QBO by influencing the simulation of wave-mean flow interaction.

The different initial conditions (seven models with ERA-Interim but three models with other reanalysis datasets) may introduce artificial inter-model differences when verifying against ERA-Interim. However, this does not affect the composite analyses. For instance, slightly different QBO amplitudes do not change the number of EQBO and WQBO winters in each model. Even for the MJO, its prediction skill evaluated against JRA-55 is comparable to that against ERA-Interim (Vitart 2017).

5.3. MJO prediction skill with QBO

The general prediction skill for the MJO using 10 S2S models has previously been evaluated for the boreal winter in Vitart (2017) and Lim et al. (2018). Figure 5.2a summarizes BCOR skill of each model. The S2S models exhibit a significant inter-model spread in MJO prediction skill, ranging from 13 to 35 days (see dotted line). Here, the MJO prediction skill is evaluated with BCOR=0.5 unless specified. This large inter-model spread has partly been explained by model mean biases (Gonzalez and Jiang 2017; Lim et al. 2018). Lim et al. (2018) showed that the models with smaller biases in the horizontal moisture gradient and cloud-longwave radiation feedback over the Maritime Continents produce a higher MJO prediction skill (see also Chap. 6).

Figures 5.2b and 5.2c, respectively, present BCORs for EQBO and WQBO winters. The decrease in BCORs over the first two weeks of the forecast is more abrupt during WQBO winters than during EQBO winters. This is particularly true for the CMA, CNR-ISAC, CNRM, ECCC, and NCEP models. Overall MJO prediction skills range from 17 to 36 days during EQBO winters, but only from 10 to 28 days during WQBO winters. Here we note that the results for the BoM model are very similar, but not identical, to those presented in Marshall et al. (2017). A slight difference is likely caused by 1) inclusion of weak MJO events in Marshall et al. (2017), 2) different reference

data for verification, 3) different analysis period, and 4) different definition of QBO phase.

This MJO prediction skill is concisely summarized in Fig. 5.3. On average, the MJO prediction skill is 21.2±7.2 days. This skill increases to 23.6±6.4 days during EQBO winters, but decreases to 17.9±6.2 days during WQBO winters. The EQBO-WQBO difference is on average 6.0±3.2 days. A similar difference is also found when BCOR=0.6 (i.e., 5.2±2.4 days; see medium shading in Fig. 6.3), 0.7 (i.e., 4.3±2.1 days; see medium-dark shading), or 0.8 (i.e., 2.4±1.6 days; see dark shading) is used. To test the robustness, the same analyses are repeated by using the real-time OLR-based MJO indices (Kiladis et al. 2014). Although not shown, essentially the same results are obtained. All models show a higher MJO prediction skill during EQBO winters than during WQBO winters.

These results suggest that the S2S models have a higher MJO prediction skill during EQBO winters than during WQBO winters regardless of the choice of BCOR thresholds and MJO indices. The EQBO-WQBO MJO skill difference, however, significantly varies from model to model. The CNRM model, for instance, shows a 10-day difference. However, the NCEP and UKMO models show only a one-day difference. To evaluate the significance of these skill differences, the bootstrap significance test is conducted. Specifically, the confidence intervals of MJO prediction skills are computed with 10,000 bootstrap sampling for EQBO and WQBO winters

(e.g., Vitart 2017). When their confidence intervals are not overlapped, the skill difference is determined to be statistically significant (Lin and Brunet 2011; Vitart 2017). It turns out that six models (i.e., BoM, CMA, CNR-ISAC, ECMWF, JMA, NCEP models) show statistically significant EQBO-WQBO skill differences at 90% confidence level for varying BCOR thresholds. But, only three models show significant differences at 95% confidence level, presumably due to small sample sizes.

This result, however, is still physically meaningful. When the same analyses are repeated with respect to the two ENSO phases, no systematic differences are obtained (not shown). Five models show an enhanced MJO prediction skill during El Niño winters, but the other five show an opposite result. More importantly, none of 10 S2S models exhibit statistically significant MJO prediction skill differences between El Niño and La Niña winters even at 90% confidence level. This finding supports that the QBO-MJO prediction skill relationship, shown in Figs. 5.2 and 5.3, does not likely occur by chance.

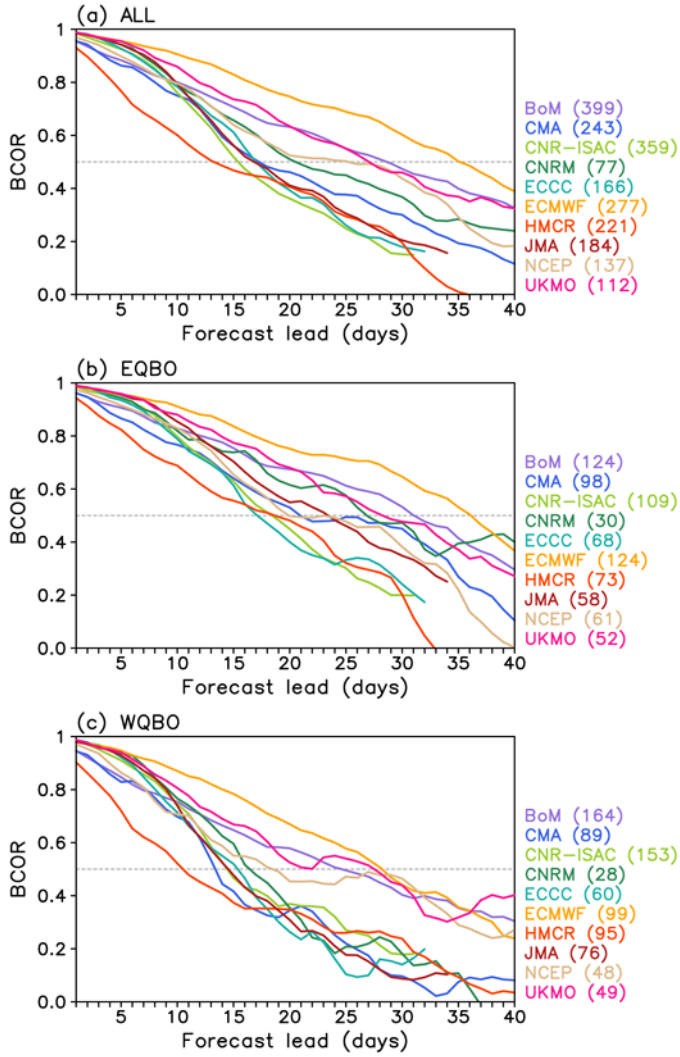

Figure 5.2. BCORs as a function of forecast days during (a) ALL, (b) EQBO, and (c) WQBO winters. As a reference, BCOR=0.5 is denoted with a dotted line. Only MJO events with initial MJO amplitude greater than 1.0 are considered here. The number of reforecasts used in each QBO phase is indicated in parenthesis.

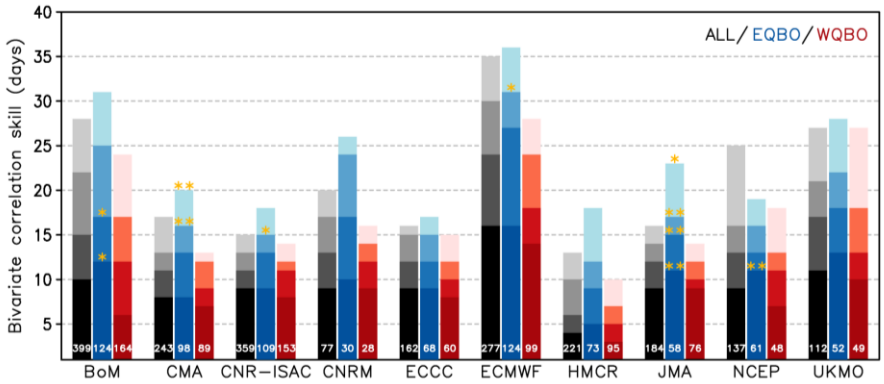

Figure 5.3. BCOR skills during ALL (black), EQBO (blue) and WQBO winters (red). The number of reforecasts used in each category is denoted in white at the bottom of each bar. Light, medium, medium-dark, and dark bars denote the prediction skills based on BCOR of 0.5, 0.6, 0.7 and 0.8, respectively. The yellow double (single) asterisks indicate that 95% (90%) confidence intervals of BCOR skill during EQBO winters are well separated from those during WQBO winters. A bootstrap method is used to determine the confidence interval.

Figures 5.1 and 5.3 also reveal that a higher QBO prediction skill does not necessarily translate to a larger EQBO-WQBO MJO skill difference. For example, the ECMWF model, which produces one of the best depictions of the QBO and has the best MJO prediction skill, shows an eight-day difference in MJO prediction skill. In contrast, the BoM model, which produces the lowest QBO prediction skill of all the models, shows a seven-day difference in MJO prediction skill. The same is also true for the CMA model. This result suggests that the QBO-related MJO prediction skill change may not be strongly sensitive to the model physics and dynamics in the stratosphere. Marshall et al. (2017) argued that the behavior of the MJO itself is more important than the mean state in the stratosphere.

To better understand the prediction errors during the two QBO phases, the mean-squared amplitude errors ($\overline{\mathrm{AE}^2}$) and the mean-squared phase errors ($\overline{\mathrm{PE}^2}$) are further examined. Lim et al. (2018) showed that both amplitude and phase errors are highly correlated with BCOR skills. Figure 5.4 presents $\overline{\mathrm{AE}^2}$ and $\overline{\mathrm{PE}^2}$ of all models and multi-model mean values in the week two forecast when the EQBO-WQBO MJO skill difference rapidly increases (Fig. 5.2). Here, the week two forecast is defined by averaging value over forecast days 8-14 as in Lim et al. (2018). Note that $\overline{\mathrm{AE}^2}$ are normalized by the MJO amplitude of the observation due to a larger amplitude during EQBO winters.

Both $\overline{\mathrm{AE}^2}$ and $\overline{\mathrm{PE}^2}$ are smaller during EQBO winters. Except for the ECMWF and HMCR models, $\overline{\mathrm{AE}^2}$ range from 0.10 to 0.23 in EQBO winters

but from 0.17 to 0.30 in WQBO winters. Likewise, $\overline{\mathrm{PE}^2}$ range from $3\,\pi/16$ to $4\pi/16$ in EQBO winters, whereas they range from $4\,\pi/16$ to $6\,\pi/16$ in WQBO winters. This result indicates that both MJO amplitude and phase errors contribute to the MJO prediction skill differences between EQBO and WQBO winters.

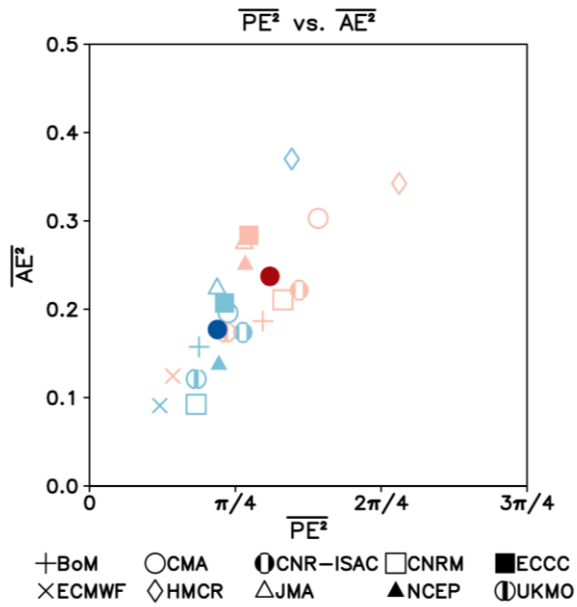

Figure 5.4. Relationship between $\overline{\mathbf{PE^2}}$ and $\overline{\mathbf{AE^2}}$ at the two-week forecast for each model during EQBO (light blue) and WQBO winters (light red). Blue and red closed circles denote the multi-model mean values.

Next we examine the relative roles of circulation and convection anomalies in MJO prediction errors (Fig. 5.5). Specifically, the pattern correlations of OLR, U850 and U200 anomalies are computed over the Indo-Pacific warm pool region (60°E -180°E, 15°S-15°N) at the two-week forecast and then averaged over all reforecasts. To focus on the intraseasonal variability, the previous 120-day averaged observation is removed from each variable before computing the pattern correlation. It turns out that the OLR correlations are typically smaller than the circulation correlations. The OLR pattern correlations range from 0.20 to 0.40, but U200 and U850 pattern correlations range from 0.30 to 0.60.

However, there is a noticeable difference between OLR and U850/U200 pattern correlations. While OLR pattern correlations do not differ much between EQBO and WQBO winters (red and blue circles in Fig. 5.5a), U850/U200 pattern correlations are reasonably well separated (Figs. 5.5b,c). This result indicates that an enhanced MJO prediction skill during EQBO winters is more closely related to a better prediction of zonal circulation than convection. It is known that MJO convection rapidly weakens within 10 days of model integration (e.g., Kim et al. 2014; Xiang et al. 2015; Kim 2017). Even though convection is weak, the associated circulations can be maintained for a while, resulting in a high MJO prediction skill. This behavior is reflected in the RMM index which is more weighted to zonal circulation

than to convection (Straub 2013; Kiladis et al. 2014; Kim et al. 2014; Kim 2017).

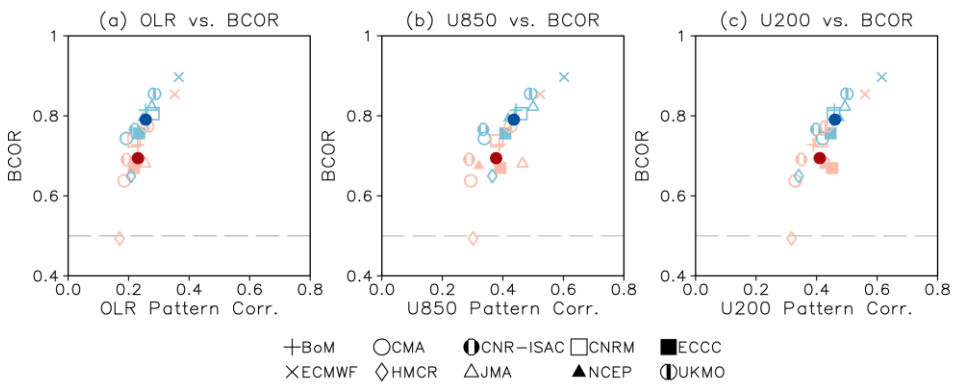

Figure 5.5. Relationships of the MJO pattern correlations of (a) OLR, (b) U850, and (c) U200 over the MJO active region (60-180°E, 15°S-15°N) against BCOR skills at the two-week forecast during EQBO (light blue) and WQBO winters (light red). Blue and red closed circles denote the multi-model mean values.

5.3.1. Sensitivity to initial MJO amplitude

One of the key factors that may determine an enhanced MJO prediction skill is MJO amplitude. The MJO is typically stronger than normal during EQBO winters (Yoo and Son 2016; Nishimoto and Yoden 2017; Son et al. 2017), and a stronger and well-organized MJO event can be better predicted than a weak MJO event (e.g., Rashid et al. 2011; Kim et al. 2014; Lim et al. 2018). Figure 5.6 shows that the MJO events with amplitudes larger than 1.5 are common during EQBO winters but not during WQBO winters. In terms of frequency, the most frequently occurring MJO events (13%) have an amplitude of 1.9 during EQBO winters. In contrast, WQBO winters show the most frequently occurring MJO events (15%) to have an amplitude of 1.1.

Marshall et al. (2017) already tested the above conjecture using the BoM model and found that the QBO-MJO prediction skill relationship is not simply determined by initial MJO amplitude. They showed that the MJO prediction skill during EQBO winters is higher than that during WQBO winters even when MJO events with a comparable initial amplitude are considered. Their analyses are extended in Fig. 5.7 for seven S2S models that have more than 50 MJO events in each QBO phase (cross marked in Table 5.1). Regardless of the initial MJO amplitude, most models show a higher MJO prediction skill in EQBO winters than in WQBO winters. The only exception is strong MJO events in the CNR-ISAC model (i.e., 1.9-2.5 and

2.0-2.6 bins of initial amplitude). This result clearly indicates that a higher MJO prediction skill is not simply due to a stronger initial MJO amplitude.

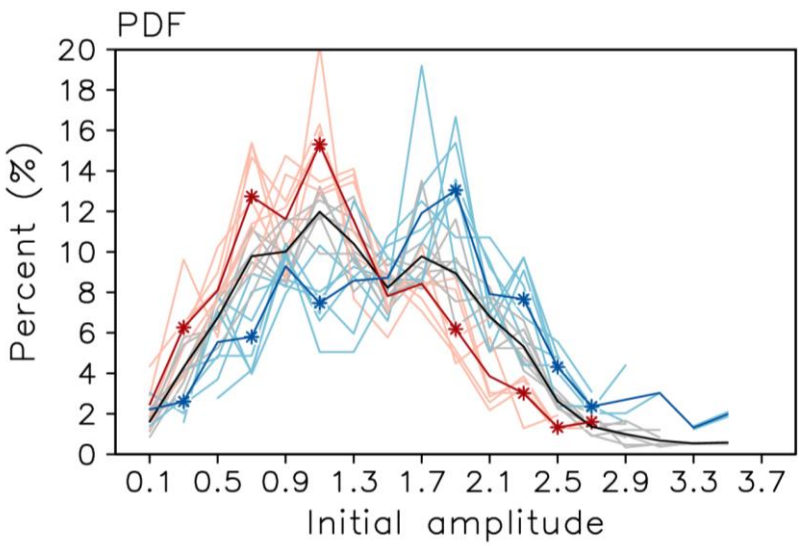

Figure 5.6. Probability distribution function of initial MJO amplitude during ALL (black), EQBO (blue), and WQBO winters (red). Shown value is the ratio of the number of events in each bin (at bin intervals of 0.2) to the total number of events in each category. Seven individual models that have enough number of reforecasts (Table 5.1) are denoted with light colored lines, and their multi-model mean values are denoted with dark colored lines. The bins, in which EQBO-WQBO differences are statistically significant at 95% confidence level, are marked in blue and red asterisks. A Student's t test is used for significance test.

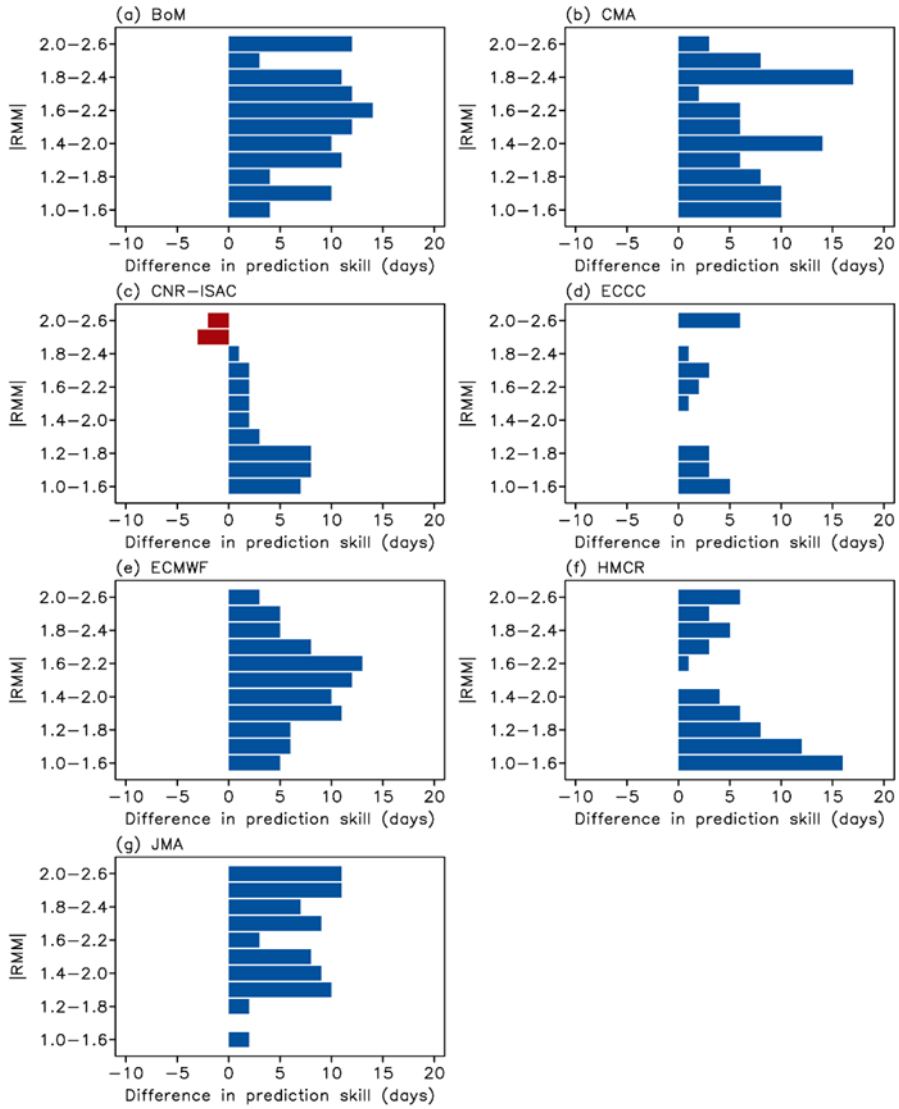

Figure 5.7. The differences in MJO prediction skills for BCOR=0.5 between EQBO and WQBO winters for each MJO amplitude (bin width is 0.6). As in Fig. 5.6, only seven models that have enough number of reforecasts are considered here.

5.3.2. Sensitivity to initial MJO phase

The sensitivity of MJO prediction skill to initial MJO phase is also tested in Fig. 5.8. The positive EQBO-WQBO MJO skill differences appear in most phases and in most models. All seven models particularly exhibit a higher MJO prediction skill during EQBO winters when initialized in MJO phases 4-5 and 6-7. The enhanced skills for phases 4-5 and 6-7 are relatively large in the high-top models (i.e., CMA, ECMWF, and JMA models) compared to the low-top models (e.g., CNR-ISAC, ECCC, and HMCR models).

A systematic skill difference, however, does not appear during MJO development and decaying phases (i.e., MJO phases 2-3 and 8-1 in Fig. 5.8). For example, the BoM and ECMWF models, which are the best two models in terms of the MJO prediction skill, show either no difference or a deficit in prediction skill during EQBO winters compared to WQBO winters when initialized in MJO phase 8-1. This is also the case for the BoM, CNR-ISAC and HMCR models for MJO phase 2-3. This result may suggest that QBO-MJO link is better captured when the model is initialized with well-organized MJO circulations. Note that a less systematic QBO-MJO prediction skill relationship in MJO phases 8-1 and 2-3 is not related to MJO amplitude. The initial MJO amplitudes in these MJO phases are robustly stronger during EQBO winters than during WQBO winters (not shown).

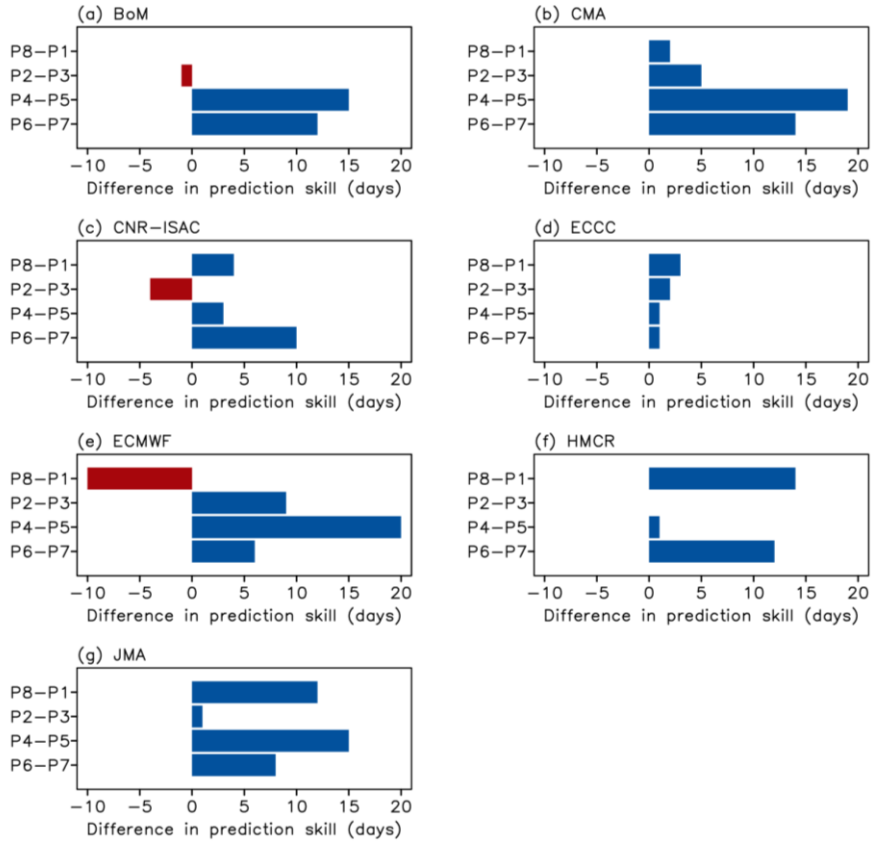

Figure 5.8. Same as Fig. 5.7 but for each MJO phase.

5.3.3. Limiting factors of MJO prediction skill

What is the cause of different MJO prediction skill between the two QBO phases? We speculate that it may partly result from varying persistence of MJO. If the observed MJO is maintained only for two weeks, the theoretical limit of MJO prediction skill would be just two weeks. After two weeks, unorganized or random perturbations in the observation, which are not necessarily associated with MJO, would have small correlation with the predicted MJO anomalies. The fact that MJO is less organized and less persistent during WQBO winters (Son et al. 2017; Nishimoto and Yoden 2017; Hendon and Abhik 2018; Zhang and Zhang 2018) then implies that the theoretical limit of MJO prediction is lower in WQBO winters than in EQBO winters.

Figure 5.9 presents U850 and OLR anomalies for MJO phase 4-5 in the observations (contour) and at forecast day 1 from the ECMWF model (shading). The model variables that are statistically significant at 95% confidence level are dotted. A Student's t test is used here. As in Fig. 5.5, the previous 120-day averaged observation is subtracted from the anomalies to obtain the MJO-related subseasonal circulation patterns. MJO convection, with negative OLR anomalies over the Maritime Continents and positive OLR anomalies over the central Pacific, is well organized during EQBO winters (Fig. 5.9c). Consistent with this, lower-level westerlies over the Indian Ocean and easterlies over the Pacific Ocean are well defined (Fig.

5.9a). A similar circulation pattern appears during WQBO winters (Fig. 5.9b). However, lower-level westerlies over the Indian Ocean and the easterlies over the central Pacific exhibit a large asymmetry. The resulting low-level convergence is weak and spatially quite broad.

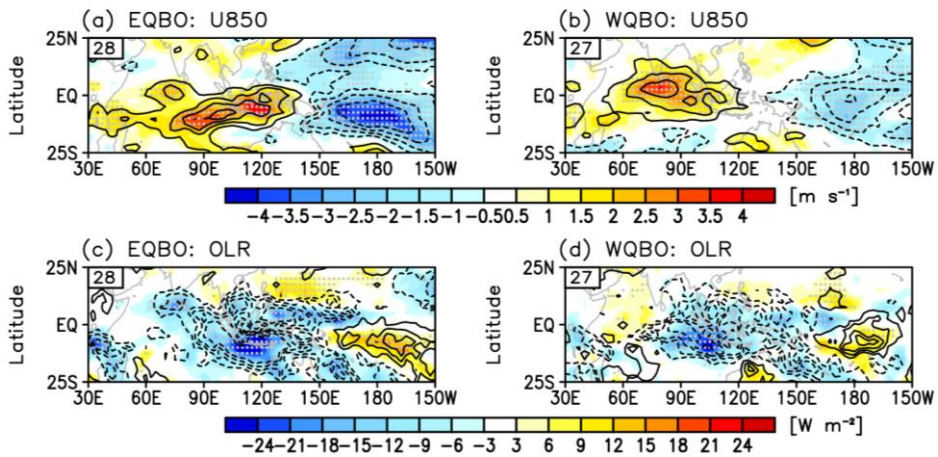

Figure 5.9. (Top) U850 and (bottom) OLR composite anomalies for MJO phase 4-5 during (left) EQBO and (right) WQBO winters at forecast day 1 from ECMWF model. The anomalies from reforecasts are shaded and that from the observations are contoured. Model anomalies, which are statistically significant at 95% confidence level, are dotted in gray. A Student's t test is used for significance test. The contour intervals of U850 and OLR anomalies are 1 m s^{-1} and 6 W m^{-2}, respectively. The sample size is denoted in the top-left corner.

Figures 5.10a,b present the longitude-time evolution of OLR and U850 anomalies beginning from MJO phase 4-5. All variables are averaged over 15°S-5°N and a five-day moving average is applied. It is evident that initial circulation and convection anomalies are strong and well organized during EQBO winters (Fig. 5.10a; see also Fig. 5.9). More importantly, the MJO persists quite long. Especially, U850 anomalies are statistically significant up to four weeks, propagating all the way to the date line (see dotted values in Fig. 5.10a). However, during WQBO winters, significant U850 anomalies are obtained for only two weeks (Fig. 5.10b). After two weeks, no organized convection or circulation anomalies are observed. This result implies that the theoretical limit of MJO prediction skill would be about four weeks in EQBO winters but only about two weeks in WQBO winters.

Figures 5.10c,d are same as Figs. 5.10a,b but for the ECMWF forecast. During EQBO winters, the model predicts both U850 (contour) and OLR anomalies (shading) remarkably well (compare Figs. 5.10a and 5.10c) although overall amplitude and eastward propagation speed are somewhat underestimated (see also Fig. 5.4). The model, however, exaggerates MJO propagation during WQBO winters (Fig. 5.10d), failing to reproduce the breakdown of MJO within two weeks. Instead, the predicted MJO, although weak, keeps propagating eastward as in EQBO winters. This result indicates that relatively low MJO prediction skill in WQBO winters is caused by an early breakdown of MJO that is not well predicted by the model.

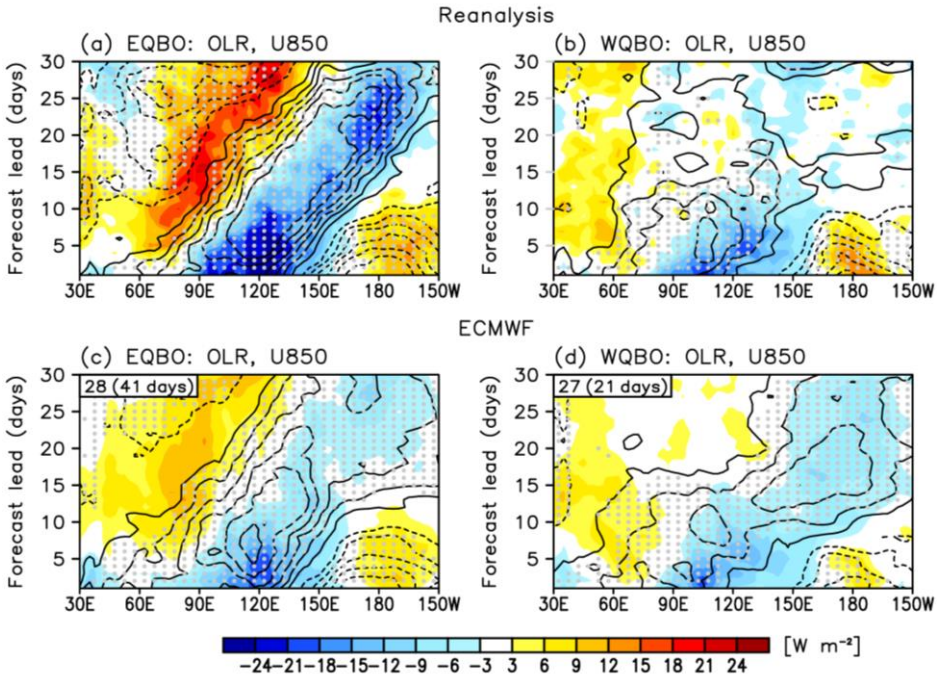

Figure 5.10. Longitude-time evolution of (top) NOAA OLR and ERA-Interim U850 anomalies and (bottom) ECMWF OLR and U850 anomalies averaged over 15°S-5°N for MJO phase 4-5 during (left) EQBO and (right) WQBO winters. Shading interval of OLR anomalies is 3 W m^{-2} and contour interval of U850 anomalies is 0.5 m s^{-1}. U850 anomalies, which are statistically significant at 95% confidence level, are dotted in gray. A Student's t test is used for significance test. The sample size is denoted in the top-left corner, and MJO prediction skill for BCOR=0.5 is indicated in the parenthesis.

The MJO evolutions are further examined for the BoM, CMA, and JMA models (Fig. 5.11). These models show large differences in MJO prediction skill for MJO phase 4-5 (Fig. 5.8). In all models, U850 anomalies are well maintained for about 30 days during EQBO winters (Figs. 5.11a,c,e). In the BoM model which is the second best model in terms of BCOR skill, not only U850 but also OLR anomalies are well captured up to four weeks.

These three models, however, predict somewhat different MJOs during WQBO winters. Unlike the ECMWF model, the BoM model shows a similar spatio-temporal structure to the observation with weakened eastward propagating lower-level wind and convection anomalies (Fig. 5.11b). However, it still exaggerates MJO propagation. Although the observed MJO is disorganized in two weeks (Fig. 5.10b), the predicted MJO is maintained up to three weeks. The CMA and JMA models also successfully captured the MJO anomalies in the first week. These anomalies are rapidly disorganized in the CMA model in the second week (Fig. 5.11d). In contrast, those in the JMA model are maintained for almost four weeks over the Indian Ocean without eastward propagation. These diverse MJO predictions, which are particularly evident when MJO becomes disorganized in the observations, are responsible for relatively low MJO prediction skills during WQBO winters.

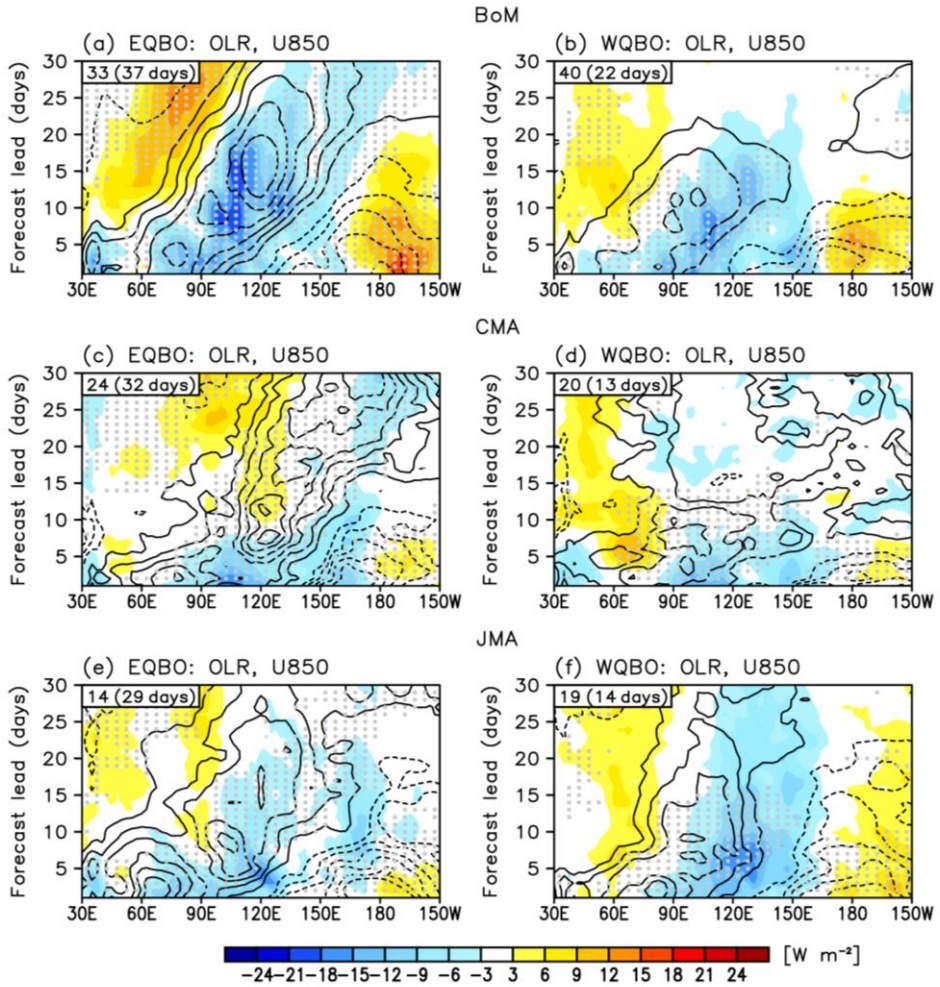

Figure 5.11. Same as Figs. 5.10c,d but for (top) BoM, (middle) CMA, and (bottom) JMA models.

Chapter 6. MJO prediction skill in the S2S prediction models: for improving the simulation of the QBO-MJO connection

This chapter is organized as follows. In Sect. 6.1, observations, S2S model datasets, and the metrics of MJO forecast skill are introduced. The MJO prediction skill in the S2S models and its characteristics are then described in Sect. 6.2. The possible cause(s) for the limited MJO prediction skill is discussed in Sect. 6.3.

6.1. Data and methods

6.1.1. Data

Daily averaged upper (200-hPa) and lower (850-hPa) tropospheric zonal winds for the period of 1980-2013 are obtained from the ERA-interim reanalysis data (Dee et al. 2011) for the model evaluation. The daily NOAA OLR data (Liebmann and Smith 1996) and precipitation product from the Global Precipitation Climatology Project (GPCP; Huffman et al. 2001) are used to characterize the tropical convective activity for the periods of 1980-2013 and 1996-2013, respectively. The moisture distribution is further quantified with column-integrated water vapor data that is derived from the combined precipitable water products from the Special Sensor Microwave Imager (SSM/I, Wentz et al. 2012) and the Tropical Rainfall Measurement Mission Microwave Imager (TMI, Hou et al. 2001) over 1998-2013.

The S2S data used in Chap. 6 are almost same with the datasets used in Chap. 5 (Table 5.1). Unless otherwise specified, all analyses are performed with ensemble-mean forecasts during NDJFM for all available years. While this approach does not allow a fair comparison between the models, it enables us to assess the best estimate of each model's prediction skill.

6.1.2. Evaluation metrics

Using the RMM indices, the observed and forecasted MJO amplitudes, A_O and A_M, and their co-variability, C_{OM}, are defined as below:

$$A_O(t) = \sqrt{O_1^2(t) + O_2^2(t)}, \tag{6.1}$$

$$A_M(t,\tau) = \sqrt{M_1^2(t,\tau) + M_2^2(t,\tau)}, \tag{6.2}$$

$$C_{OM}(t,\tau) = O_1(t)M_1(t,\tau) + O_2(t)M_2(t,\tau), \tag{6.3}$$

where $O_1(t)$ and $O_2(t)$ are the observed RMM1 and RMM2 indices at time t, and $M_1(t,\tau)$ and $M_2(t,\tau)$ are the respective reforecasts with the lead time of τ. Likewise, the observed and forecasted MJO phases in the RMM space, ϕ_O and ϕ_M, are defined as below:

$$\phi_O(t) = tan^{-1}\left(\frac{O_2(t)}{O_1(t)}\right), \tag{6.4}$$

$$\phi_M(t,\tau) = tan^{-1}\left(\frac{M_2(t,\tau)}{M_1(t,\tau)}\right). \tag{6.5}$$

Using these properties, several MJO skill metrics are calculated. One of the key metrics used in this study is the so-called bivariate anomaly correlation coefficient (BCOR) (e.g., Rashid et al. 2011; Same with Eq. 5.1):

$$\mathrm{BCOR}(\tau) = \frac{\sum_{t=1}^{N} C_{OM}(t,\tau)}{\sqrt{\sum_{t=1}^{N} A_O^2(t)}\sqrt{\sum_{t=1}^{N} A_M^2(t,\tau)}}, \quad (6.6)$$

where N is the number of reforecasts. Following previous studies, the MJO prediction skill of each model is determined as the forecast lead time when BCOR becomes lower than 0.5 (e.g., Rashid et al. 2011). Since the choice of this threshold value is somewhat arbitrary, other threshold value, such as 0.7, is also considered in the sensitivity test (e.g., Table 6.1).

In order to track the relative importance of MJO amplitude and phase errors to the total error, a bivariate mean squared error (BMSE) is defined in this study:

$$\mathrm{BMSE}(\tau) = \frac{1}{N}\sum_{t=1}^{N}\left[\left(M_1(t,\tau) - O_1(t)\right)^2 + \left(M_2(t,\tau) - O_2(t)\right)^2\right]. \quad (6.7)$$

This metric is the same as the square of root mean squared error (RMSE) in the literature (e.g., Rashid et al. 2011). As RMSE < $\sqrt{2}$ is generally used to determine the prediction skill, BMSE < 2.0 is set as an upper limit of the reliable MJO prediction in this study. BMSE can be decomposed into its amplitude-error component, BMSEa, and phase-error component, BMSEp, as below:

$$\mathrm{BMSE}(\tau) = \mathrm{BMSEa}(\tau) + \mathrm{BMSEp}(\tau), \quad (6.8)$$

where

$$\mathrm{BMSEa}(\tau) = \frac{1}{N}\sum_{t=1}^{N}[A_M(t,\tau) - A_O(t)]^2, \tag{6.9}$$

$$\mathrm{BMSEp}(\tau) = \frac{1}{N}\sum_{t=1}^{N} 2A_M(t,\tau)\,A_O(t)\{1 - cos(\phi_M(t,\tau) - \phi_O(t))\}. \tag{6.10}$$

As shown below, the BMSEa is essentially the same as the mean-squared amplitude error (Eq. 6.13). Note that the BMSEp is not only determined by the MJO phase error but also weighted by the observed and forecasted MJO amplitudes. As the MJO amplitude decreases with forecast lead times, an increasing BMSEp, which is the case for all reforecasts, is primarily explained by the MJO phase error (not shown). Although this decomposition does not clearly separate MJO amplitude and phase errors, it still allows us qualitatively to attribute the total model errors into amplitude-dependent and phase-dependent ones.

To understand the amplitude and phase errors more directly, other standard metrics of MJO amplitude and phase errors are also utilized. They include the mean amplitude error ($\overline{\mathrm{AE}}$) and mean phase error ($\overline{\mathrm{PE}}$).

$$\overline{\mathrm{AE}}(\tau) = \frac{1}{N}\sum_{t=1}^{N}[A_M(t,\tau) - A_O(t)], \tag{6.11}$$

$$\overline{\mathrm{PE}}(\tau) = \frac{1}{N}\sum_{t=1}^{N}[\phi_M(t,\tau) - \phi_O(t)]. \tag{6.12}$$

$\overline{\mathrm{PE}}$ typically ranges from $-\pi/2$ to $\pi/2$. In some cases, $\overline{\mathrm{PE}}$ can rapidly increase with forecast lead times, and eventually jump from $\pi/2$ to $-\pi/2$ when the MJO amplitude is small (Rashid et al. 2011). To prevent such an artificial jump, $\overline{\mathrm{PE}}$ is evaluated in units of degrees from 0° to 360°, and subsequently converted into radian.

Both $\overline{\mathrm{AE}}$ and $\overline{\mathrm{PE}}$ characterize the mean errors, rather than the absolute errors of individual reforecasts. If the model errors are positive in some cases but negative in others, the mean errors would become negligible. To prevent such cancellation and to quantify model error better, the mean-squared amplitude error ($\overline{\mathrm{AE}^2}$) and mean-squared phase error ($\overline{\mathrm{PE}^2}$) are also considered in this study. They are computed as below:

$$\overline{\mathrm{AE}^2}(\tau) = \frac{1}{N}\sum_{t=1}^{N}[A_M(t,\tau) - A_O(t)]^2, \tag{6.13}$$

$$\overline{\mathrm{PE}^2}(\tau) = \frac{1}{N}\sum_{t=1}^{N}[\phi_M(t,\tau) - \phi_O(t)]^2. \tag{6.14}$$

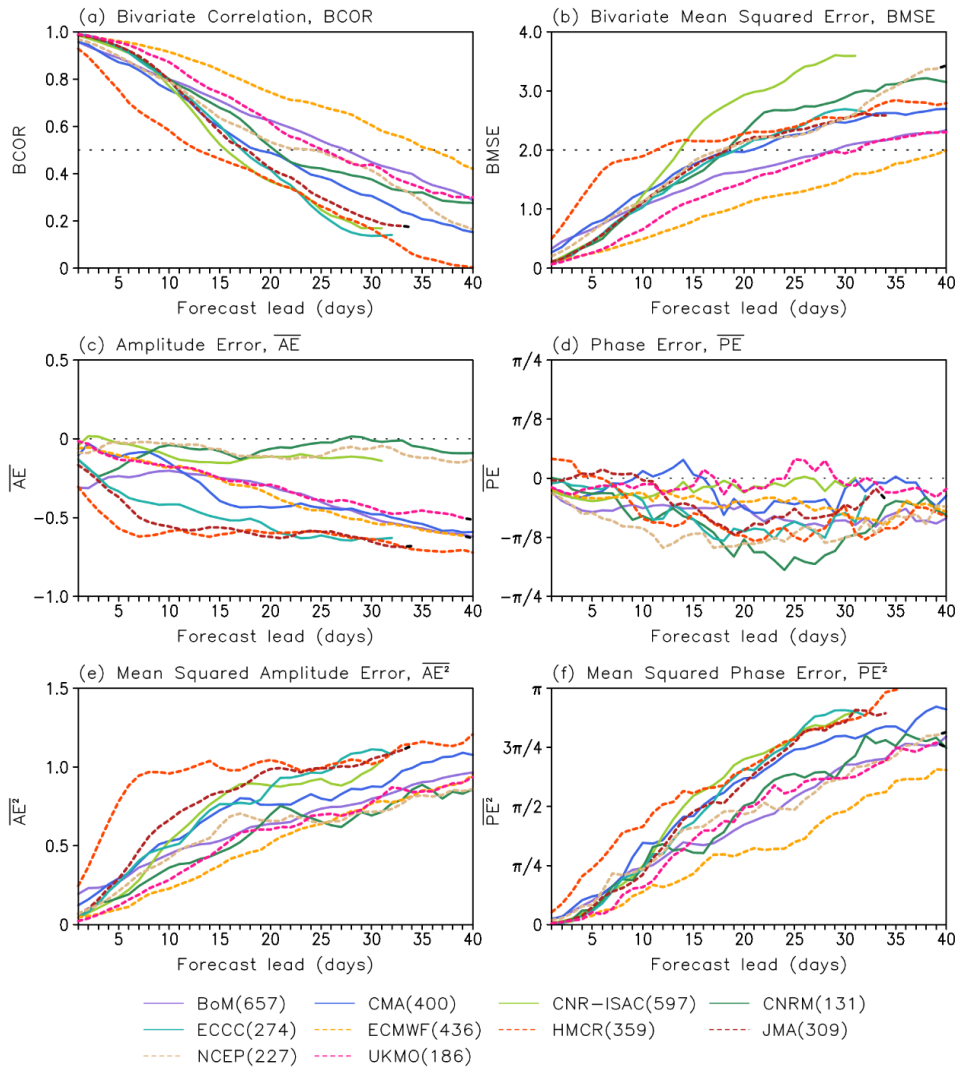

Figure 6.1. MJO prediction errors as a function of forecast lead times: (a) BCOR, (b) BMSE, (c) $\overline{AE}$, (d) $\overline{PE}$, (e) $\overline{AE^2}$, and (f) $\overline{PE^2}$. The MJO cases with an initial amplitude greater than 1.0 are used. The model name and its reforecast size are indicated at the bottom.

6.2. MJO prediction skill

Figure 6.1a presents the MJO prediction skill of all models in terms of the BCOR metric. Reforecasts with initial MJO amplitude smaller than one are excluded to ensure that the MJO signal is robust at least in the initial conditions. BCOR consistently decreases with forecast lead times and crosses the threshold of 0.5 in 12-36 days, which is consistent with the result of Vitart (2017). Among the 10 S2S models, the ECMWF model shows a relatively high prediction skill of 36 days, with the slowest decrease of BCOR. By contrast, the HMCR model shows a relatively rapid decrease of BCOR in the first two weeks which drops below 0.5 at the forecast lead time of 12 days. Except for these two models, others are clustered together in the first two-week forecasts.

The overall MJO prediction skill, shown in Fig. 6.1a, is summarized in Table 6.1 (see the first column). The multi-model mean MJO prediction skill is approximately three weeks. Even with a higher threshold value (e.g., BCOR > 0.7), the MJO is qualitatively well predicted for up to approximately two weeks (the numbers in parentheses). Quantitatively, the BoM, ECMWF, and UKMO models show relatively higher BCOR skills with retaining BCOR greater than 0.5 (0.7) up to more than 25 (15) days of forecast lead time. As discussed later, these three models also exhibit relatively higher BMSE skills, ranging from 28 to 40 days (see the third numbers in the first column).

Table 6.1. MJO prediction skills for all reforecasts (All) and the reforecasts initialized in different MJO phases. The MJO events with the initial MJO amplitude is greater than 1.0 are used. The first number, followed by parenthesis, denotes the BCOR skill. The number in parenthesis is also the BCOR skill, but based on a correlation coefficient greater than 0.7 instead of 0.5. The second number indicates the BMSE skill. The multi-model mean (MMM) value and one standard deviation are also shown at the bottom.

	All	Phase 8-1	Phase 2-3	Phase 4-5	Phase 6-7
BoM	27 (15), 28	31 (16), 28	24 (15), 28	28 (14), 28	25 (14), 31
CMA	18 (12), 20	15 (9), 17	18 (11), 19	18 (11), 17	21 (13), 19
CNR-ISAC	15 (11), 13	14 (10), 13	17 (12), 14	14 (11), 13	15 (11), 13
CNRM	20 (14), 18	21 (10), 17	20 (13), 16	18 (12), 18	21 (17), 19
ECCC	17 (12), 19	19 (13), 20	16 (11), 22	15 (12), 15	17 (13), 18
ECMWF	36 (23), 40	38 (20), 40	40 (26), 41	36 (25), 39	31 (22), 37
HMCR	12 (6), 11	13 (5), 13	13, (7), 10	9 (5), 5	15 (7), 19
JMA	17 (12), 18	18 (12), 18	17 (11), 15	15 (11), 17	18 (13), 19
NCEP	24 (12), 17	30 (12), 18	18 (14), 19	31 (13), 15	23 (12), 15
UKMO	25 (16), 31	22 (14), 24	22 (17), 27	27 (15), 30	28 (19), 32
MMM	21.1±7.0 (13.3±4.3), 21.5±8.9	22.1±8.3 (12.1±4.1), 20.8±8.1	20.5±7.5 (13.7±5.1), 21.1±9.0	21.1±8.8 (12.9±5.0), 19.7±9.8	21.4±5.4 (14.1±4.3), 22.2±8.1

It is worth mentioning that the above skill estimates, 12-36 days, are slightly different from that reported by Vitart (2017) who showed that the MJO prediction skill of the S2S models ranges from 13 to 32 days. Each model's performance in this result is also slightly different from that in Vitart (2017)'s result. For instance, the CNRM model is the second best in Vitart (2017) (see their Fig. 1b) but only the fifth best in this study (Fig. 6.1a and Table 6.1) although the model rank is not meaningful in this study. This difference is likely caused by multiple factors: the different sampling strategy, the different reforecast periods used, and the slightly different ways of defining the model climatology. In regarding the sampling strategy, unlike Vitart (2017) who used all reforecasts initialized, we exclude reforecasts that contains weak MJO ($A_O(1) < 1$) in their initial conditions. Also, we extend the initial months considered in Vitart (2017) (December-March) by including November. The constraint of minimum MJO amplitude and the inclusion of November make quantitatively different results (not shown). As mentioned in Sect. 6.1, the present study considers the entire reforecast period available instead of focusing on the common reforecast period (1999-2010). The quantitative results are somewhat sensitive to the choice of reforecast period (not shown). Due to the difference in the reforecast period, the model climatology is also slightly different.

Many previous studies have shown that MJO prediction skill is dependent on the initial MJO amplitude. In general, models are more skillful when the initial MJO amplitude is stronger (Lin et al. 2008; Rashid et al. 2011; Kim et al. 2014; Neena et al. 2014; Xiang et al. 2015). This relationship is evaluated using the S2S models in Fig. 6.2. Following Kim et al. (2016), for each model, all reforecasts are grouped into three categories: i.e., strong ($A_O(1) \geq 1.5$), moderate ($0.7 \leq A_O(1) < 1.5$), and weak ($A_O(1) < 0.7$) MJO amplitude in the initial conditions. Note that Fig. 6.2 is the only case where we analyze the reforecasts with initial MJO amplitudes weaker than 1. On average, the S2S models show 21.7±7.2, 19.2±7.6, and 15.8±7.5 days of prediction skills for initially strong, moderate and weak MJO events, respectively (Fig. 6.2), confirming the previous findings (Rashid et al. 2011; Neena et al. 2014; Xiang et al. 2015). It is noteworthy that the CNR-ISAC and UKMO models do not show strong sensitivity of their MJO prediction skill to initial MJO amplitude.

Figure 6.2 also reveals a large difference in the BCORs among the three groups, especially at early period in the reforecast. That is, the BCORs of the initially weak MJO events are considerably lower than those of the initially moderate and strong MJO events. For the initially moderate and strong MJO events, the BCORs also tend to decay rather slowly with forecast lead times than that of the initially weak MJO events. Due to these differences, the sensitivity of MJO prediction skill to initial MJO amplitude becomes

larger if a higher threshold value of BCOR is used. For example, when MJO prediction skill is evaluated with BCOR > 0.7, the S2S models show MJO prediction skills of 14.3±4.4, 9.7±4.8, and 7.5±6.3 days for the initially strong, moderate, and weak MJO events, respectively. For weak MJO events, more than half of the models (i.e., BoM, CMA, CNR-ISAC, CNRM, HMCR, and NCEP models) either exhibit only a one-day prediction skill or none with BCOR > 0.8. This result again confirms that models predict the MJO better when initial MJO amplitude is strong.

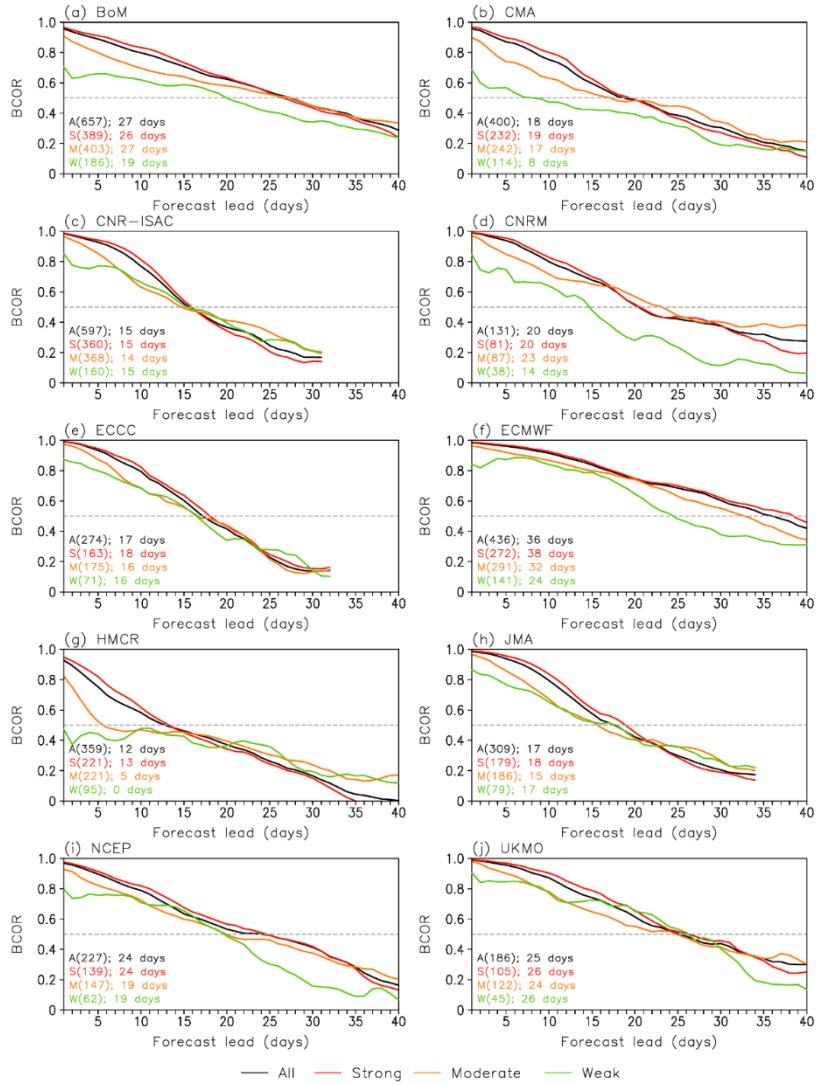

Figure 6.2. BCOR of each model as a function of forecast lead times for all reforecasts (A; black), and those initialized during strong (S; red), medium (M; orange), and weak MJO events (W; green). See the text for the definition of strong to weak MJO events. The number of reforecasts used in each category and their prediction skill are indicated at the bottom-left corner. Note that for each model the black lines are identical to the colored lines in Fig. 6.1a.

Several studies have documented that MJO prediction skill is sensitive to the initial MJO phase. In particular, models show relatively lower skill when initial MJO phase is 2 or 3, indicating that the models have difficulty in representing the MJO's propagation across the Maritime Continents (Vitart and Molteni 2010; Wang et al. 2014). This relatively poor MJO prediction skill with initial MJO phase 2-3 is often referred to as the Maritime Continent prediction barrier. However, more recent studies have reported that in the latest operational models the Maritime Continent prediction barrier is not as pronounced as in the old models (Kim et al. 2014; Neena et al. 2014; Xiang et al. 2015). Therefore, it is of a great interest to see whether the Maritime Continent prediction barrier is present in the S2S models.

Figure 6.3 illustrates the sensitivity of MJO prediction skill to initial MJO phase. Most models show some sensitivity to initial MJO phase, though the sensitivity differs among the models. In other words, the S2S models show no systematic sensitivity of their MJO prediction skill to initial MJO phase. These results also suggest that the Maritime Continent prediction barrier is not a common symptom of operational models. The only model that shows a hint of the Maritime Continent prediction barrier is the NCEP model (Fig. 6.3i), the descendant of the model used in Wang et al. (2014). In terms of BCOR skill, MJO prediction skills of the NCEP model are 30, 18, 31, and 23 days for initial MJO phases 8-1, 2-3, 4-5, and 6-7, respectively (Table 6.1). On the other hand, the ECMWF model shows the highest prediction skill in

initial MJO phase 2-3 (38, 40, 36, and 31 days of the MJO prediction skills in each initial MJO phase group).

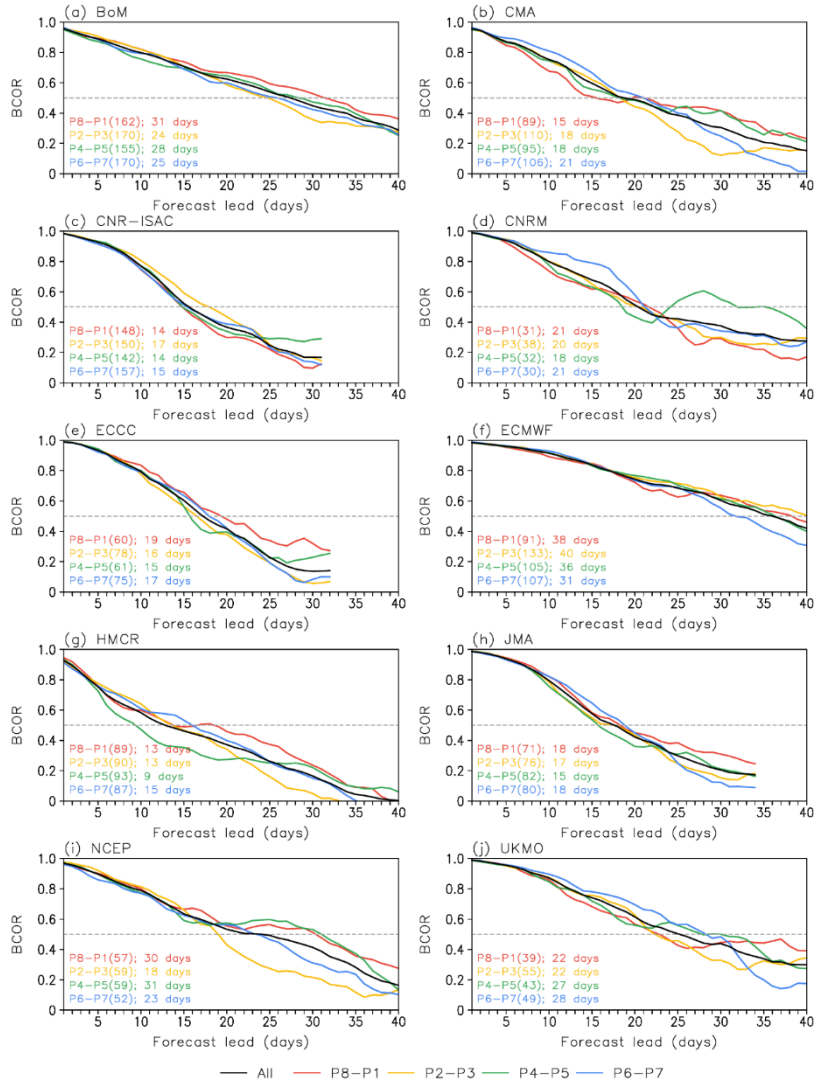

Figure 6.3. Same as Fig. 6.2 but for the reforecasts initialized in different MJO phases.

Figure 6.1b presents the BMSE time series of each model. Not surprisingly, BMSE steadily increases with forecast lead times and crosses the threshold value (2.0, gray dotted line in Fig. 6.1b) on forecast lead times of about 11-40 days. When averaged across all models, the MJO prediction skill evaluated with BMSE < 2.0 is approximately three weeks (see the third numbers in the first column of Table 6.1). Among the 10 S2S models, the BoM, ECMWF, and UKMO models show relatively higher BMSE skills, as for the BCOR skills (Table 6.1).

The advantage of the BMSE metric over the BCOR metric is that it can be decomposed into the amplitude-error-dependent component, BMSEa, and the phase-error-dependent component, BMSEp, as described in Sect. 6.1. In Fig. 6.4, the time evolutions of BMSEa (red) and BMSEp (blue) are displayed for each model. Overall, BMSEp is larger than BMSEa during the 40-day period considered, suggesting that MJO phase error dominates the total error. Although BMSEa is initially larger than BMSEp in some models (i.e., ECCC, HMCR, and JMA models), the latter becomes dominant after two weeks (Figs. 6.4e, g, and h). In the CNR-ISAC, CNRM, and NCEP models, BMSEp is even twice as large as BMSEa (Figs. 6.4c, d, and i). Here, one notable exception is the ECMWF model (Fig. 6.4f), which shows BMSEp that is comparable to BMSEa during the 40-day period. Note that the results presented in Fig. 6.4 are not significantly affected by initial MJO amplitude or phase (not shown). These results suggest that BMSEp plays a more

important role than BMSEa in the growth of BMSE and MJO prediction skill. The results also imply that the improved MJO prediction in the S2S models can be effectively achieved by reducing the source(s) of MJO phase errors. As discussed later, such errors are partly associated with the model mean biases in moisture distribution.

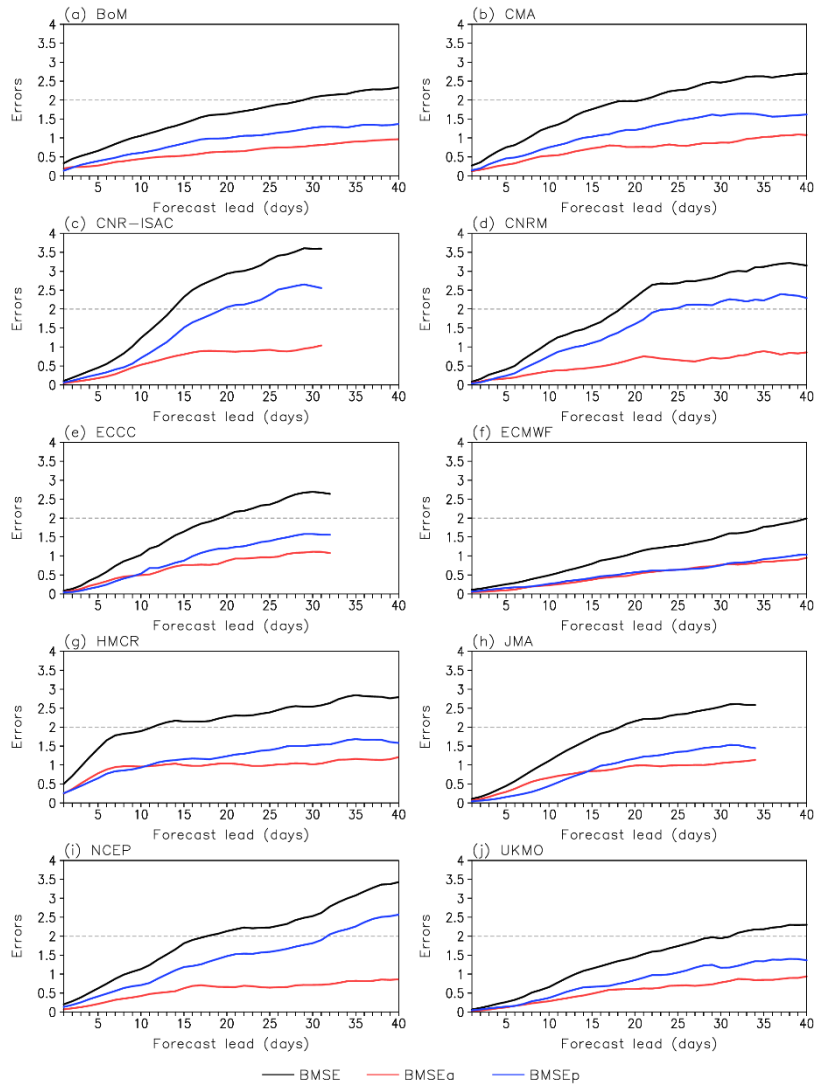

Figure 6.4. BMSE (black), BMSEa (red), and BMSEp (blue) of each model as a function of forecast lead times. Note that BMSE and BMSEa, respectively, are identical to BMSE and $\overline{AE^2}$ shown in Figs. 6.1b and 6.1e.

Figures 6.1c-f display $\overline{\mathrm{AE}}$, $\overline{\mathrm{PE}}$, $\overline{\mathrm{AE}^2}$ and $\overline{\mathrm{PE}^2}$ obtained using all available reforecasts for each model. $\overline{\mathrm{AE}}$, and $\overline{\mathrm{PE}}$ show negative values for all models throughout the 40-day period considered, indicating that most S2S models underestimate MJO amplitude and phase speed (Figs. 6.1c,d). Their temporal evolutions of $\overline{\mathrm{AE}}$s differ, although all models have negative $\overline{\mathrm{AE}}$s (Fig. 6.1c). They can be largely grouped into four categories in terms of the evolution of $\overline{\mathrm{AE}}$. The group of the CNR-ISAC, CNRM, and NCEP models has almost negligible $\overline{\mathrm{AE}}$ throughout the forecast. In another group of three models, i.e., the ECCC, HMCR, and JMA models, $\overline{\mathrm{AE}}$ grows rapidly with a minus sign during the first week and remains at approximately -0.7 afterward. The rapid development of $\overline{\mathrm{AE}}$ is quite systematic especially in the latter two models. The third group, consisting of the CMA, ECMWF, and UKMO models, shows an almost linear increase of negative $\overline{\mathrm{AE}}$ with forecast lead times. The last group is the BoM model. This model does not belong to any of above three categories. Its $\overline{\mathrm{AE}}$ is substantially high at forecast day 1 (about -0.30) as in the HMCR model. However, its temporal evolution is markedly different from any of the other models. The $\overline{\mathrm{AE}}$ of the BoM model decreases with forecast lead times until day 10 and then increases afterward consistent with Fig. 6.4c of Rashid et al. (2011). This nonlinear evolution is mainly due to the positive and negative errors in the reforecasts cancelling each other out, as it does not appear in $\overline{\mathrm{AE}^2}$ (Fig. 6.1e).

Focusing on the absolute magnitude of the errors, the mean-squared amplitude errors are illustrated in Fig. 6.1e. Unlike $\overline{\mathrm{AE}}$, $\overline{\mathrm{AE}}^2$ quasi-linearly increases with forecast lead times. Furthermore, its inter-model spread is smaller than that in $\overline{\mathrm{AE}}$, especially at later forecast lead times. As such, the models cannot be simply divided into four groups. Some models, such as the JMA and HMCR models, show a relatively rapid increase at early forecast lead times, whereas others show a quasi-linear increase. Although not distinctive, the ECMWF model exhibits the minimum $\overline{\mathrm{AE}}^2$ until forecast day 25.

Figure 6.1d presents the time series of $\overline{\mathrm{PE}}$ for each model. Unlike $\overline{\mathrm{AE}}$ which shows a large inter-model spread even at day one with respect to the maximum spread around day 20-30, $\overline{\mathrm{PE}}$ shows a relatively small inter-model spread, especially during the first five days. $\overline{\mathrm{PE}}$s in the CNR-ISAC and UKMO models are near zero, whereas the maximum $\overline{\mathrm{PE}}$s of the CNRM and NCEP models are about $-3\pi/16$. None of the S2S models show $\overline{\mathrm{PE}}$s smaller than $-\pi/4$ (about one phase in the RMM space) throughout the forecast.

Figure 6.1f illustrates the $\overline{\mathrm{PE}}^2$, which show a steady increase with forecast lead times. Unlike $\overline{\mathrm{PE}}$, the square of the phase error tends to increase linearly. Although the inter-model spread of $\overline{\mathrm{PE}}$ becomes small at forecast day 40, the spread of $\overline{\mathrm{PE}}^2$ increases continuously with forecast lead times. In contrast to $\overline{\mathrm{AE}}^2$, $\overline{\mathrm{PE}}^2$ does not saturate with forecast lead times, suggesting that the overall MJO prediction skill could be more sensitive to the MJO phase

error than to the amplitude error at longer forecast lead times. Note that the ECMWF model has the smallest $\overline{\mathrm{PE}}^2$ throughout the forecast, whereas the HMCR model has a large $\overline{\mathrm{PE}}^2$ during the first two weeks. These two models have the best and worst BCOR and BMSE skills (Table 6.1; see also Figs. 6.1a,b).

Figure 6.5 summarizes relationships among the MJO prediction skill scores in the two-week (squares) and four-week forecasts (circles). Here, the two-week and four-week forecasts are defined by averaging values over forecast lead days 8-14 and 22-28, respectively. Not surprisingly, the BCOR and BMSE values are highly correlated with each other (Fig. 6.5a). The correlation coefficient between the two in the two-week forecast (r_2) is -0.97. This one-to-one relationship indicates that the BMSE metric is comparable to the BCOR metric. Their ratio, that crosses BCOR=0.5 (dashed horizontal line) and BMSE=2.0 (dashed vertical line), further suggests that the BMSE skill can replace the BCOR skill. In fact, as summarized in Table 6.1 (see the first column), the BMSE skills are quantitatively similar to the BCOR skills in most models (approximately 21 days in MMM prediction skills). Although these two skill metrics tend to diverge at longer lead times, they are still significantly correlated at the four-week forecast (r_4=-0.8).

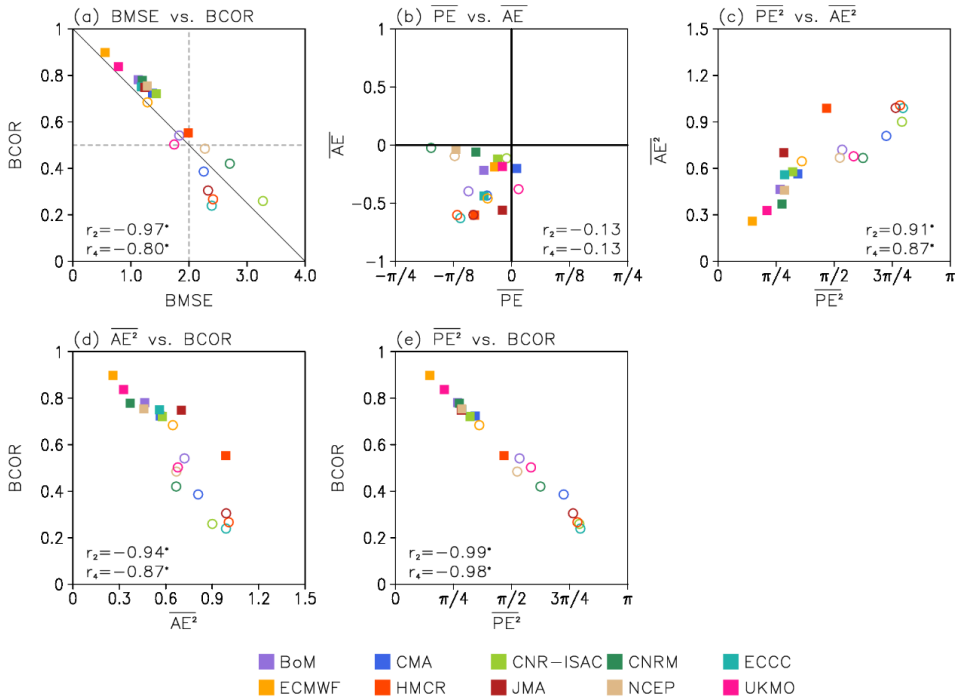

Figure 6.5. Relationships (a) between BMSE and BCOR, (b) $\overline{PE}$ and $\overline{AE}$ (c) $\overline{PE^2}$ and $\overline{AE^2}$, (d) $\overline{AE^2}$ and BCOR, and (e) $\overline{PE^2}$ and BCOR at the two-week forecasts (closed squares) and four-week forecasts (opened circles). Their correlation coefficients, r_2 and r_4, are also shown at the bottom of each panel. The correlation coefficients that are statistically significant at the 95% confidence level are denoted by an asterisk.

The two representative mean error metrics, i.e., $\overline{\mathrm{AE}}$ and $\overline{\mathrm{PE}}$, are not closely related with each other (Fig. 6.5b). This result is again due to cancellations between large positive and negative errors. $\overline{\mathrm{AE}^2}$ and $\overline{\mathrm{PE}^2}$ are significantly correlated, even in the four-week forecast (Fig. 6.5c). Models with a smaller $\overline{\mathrm{PE}^2}$ have a smaller $\overline{\mathrm{AE}^2}$. Their correlation coefficient across all 10 models is 0.91 and 0.87 at the two-week and four-week forecast, respectively, suggesting that the amplitude and phase errors are inherently related with each other.

The relationship of $\overline{\mathrm{AE}^2}$ and $\overline{\mathrm{PE}^2}$ with the BCOR is evaluated in Figs. 6.5d and e, respectively. As anticipated from Figs. 6.5a and c, both $\overline{\mathrm{AE}^2}$ and $\overline{\mathrm{PE}^2}$ are highly correlated with BCOR with a correlation coefficient greater than -0.94 in the two-week forecast and -0.87 in the four-week forecast. Between them, $\overline{\mathrm{PE}^2}$ shows a higher correlation with BCOR than $\overline{\mathrm{AE}^2}$. Their correlation coefficient remains -0.98 even in the four-week forecast. This result again suggests that the MJO prediction skill in the S2S models is more sensitive to the phase error than the amplitude error, especially at longer forecast lead times (see also Fig. 6.4).

6.3. Mean-state biases and their impact on MJO prediction skill

There is a growing body of thought that considers the MJO as a ‘‘moisture mode’’ on an equatorial beta plane (Neelin and Yu 1994; Raymond 2001; Sobel and Maloney 2012, 2013; Adames and Kim 2016; Fuchs and Raymond 2017). Under this framework, which is based on the tight coupling between moisture and convection (e.g., Bretherton et al. 2004) and the smallness of buoyancy perturbations in the tropics (Charney 1963; Sobel et al. 2001), the evolution of large-scale, low-frequency convective anomalies associated with the MJO is explained by those of moisture anomalies. The moisture mode theory has provided a framework for studying and interpreting the column-integrated moisture budget of the MJO in observations and in models. The results of the budget studies collectively indicate that horizontal moisture advection, especially the advection of the mean moisture by the MJO perturbation wind, is the key process that moistens ahead (east) and dries behind (west) the region of enhanced moisture anomalies, controlling the MJO propagation (Kiranmayi and Maloney 2011; Andersen and Kuang 2012; Adames and Wallace 2015; Wang et al. 2017).

These results suggest that, to accurately forecast the MJO, the operational models may need to represent a realistic horizontal distribution of the mean moisture. Gonzalez and Jiang (2017) showed that GCMs’ MJO simulation performances have a close relationship with their ability to represent accurately the basic state moisture distribution over the Indo-Pacific

warm pool. Kim (2017) examined the column-integrated moist static energy (MSE) budget of the MJO in the European Center for Medium-Range Weather Forecasts (ECMWF) reforecast dataset and showed that a dry bias in the mean moisture distribution caused a weakening of horizontal moisture advection, resulting in an early disruption of the MJO in the reforecasts.

The cloud–longwave radiation (CLW) feedback process has also been suggested as the key process for the MJO's maintenance (Kiranmayi and Maloney 2011; Andersen and Kuang 2012; Adames and Kim 2016). The increase of moisture and clouds during the active phase of the MJO reduces the amount of longwave cooling, causing an anomalous longwave warming in the troposphere. This anomalous warming is balanced by upward motion, which moistens the column by vertical advection of moisture (Chikira 2014; Janiga and Zhang 2016; Wolding et al. 2016). Through this moistening, the increase of cloud amounts that is caused by the enhanced convection provides a favorable condition for further development of the anomalous convection.

6.3.1. Mean moisture field

As mentioned above, previous studies of column-integrated moisture or moist static energy have shown that the CLW feedbacks and horizontal distribution of the mean state moisture are key to the MJO maintenance and propagation of the observed MJO. In this section, we investigate the relationship between the MJO prediction skills in the S2S models and model

biases in the basic-state moisture distribution and CLW feedbacks. Among the 10 S2S models, only seven models provide column-integrated wave vapor as indicated in Table 5.1 (indicated by pound). Therefore, all analyses below are performed with these seven models.

Figure 6.6a shows the NDJFM mean CWV from the satellite observations, described in Sect. 6.1. The observed CWV distribution exhibits a distinct maximum in the Indo-Pacific warm pool region, featuring large-scale zonal and meridional gradients of CWV across the Indo-Pacific warm pool region. The CWV maximum over the warm pool area is typically underestimated in the S2S models (Figs. 6.6b-h). Each model's CWV, averaged over the first 30-day forecast, exhibits a significant dry bias around the Maritime Continent. In the subtropics (poleward of 15°S/N), most models show either dry biases that are weaker than equatorial dry biases (e.g., CMA, ECMWF, JMA, and NCEP models) or wet biases (e.g., BoM, CNRM and ECCC models). This pattern of moisture biases suggests that both zonal and meridional gradients of the background moisture are underestimated in most models.

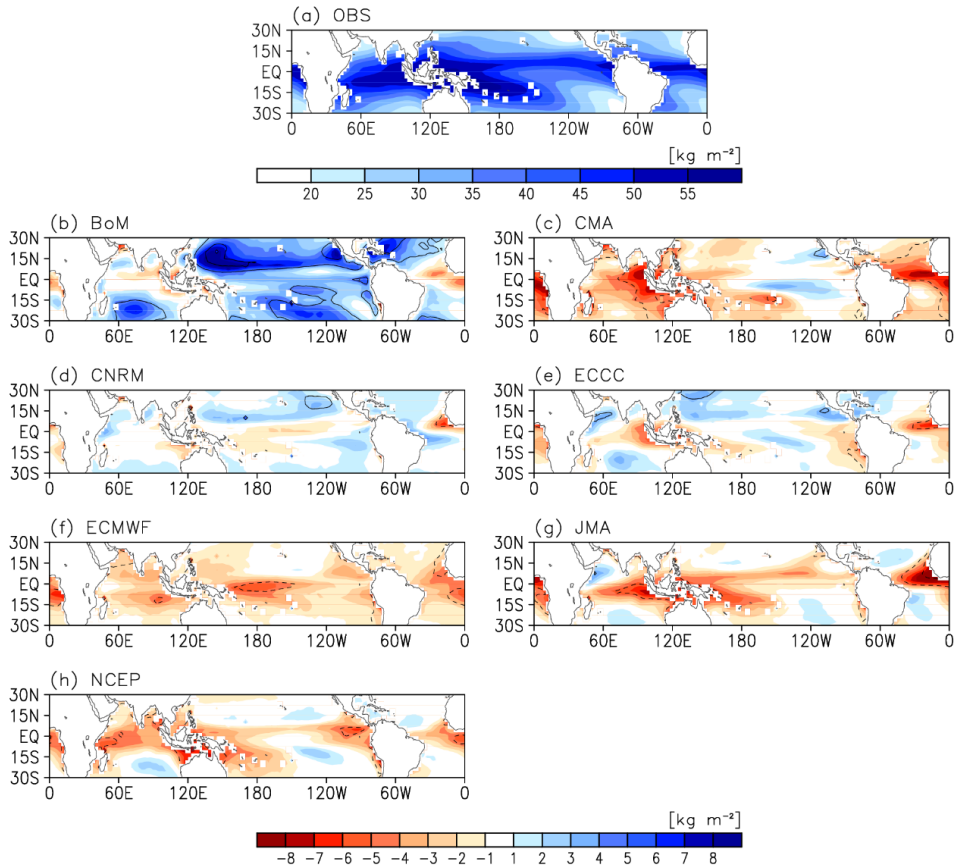

Figure 6.6. (a) Wintertime (NDJFM) climatology of CWV, derived from satellite observations, and (b-h) the model mean biases averaged over forecast lead times of 1-30 days. The model biases that are -20, -10, 10, and 20% of the observations are contoured in each panel.

If all other conditions (e.g., large-scale circulations) are equal, a weaker horizontal moisture gradient would damp horizontal moisture advection associated with the MJO. Because it is the horizontal moisture advection that dominates the moistening and drying tendencies to the east and west of the enhanced MJO convections, respectively, and thereby pushing the MJO convection anomalies to move eastward, a weaker horizontal advection would slow down the eastward propagation of the MJO. This line of consideration leads us to hypothesize that the models with a smaller moisture-gradient bias may have a better MJO prediction skill.

The above hypothesis is qualitatively tested by examining the relationship between MJO prediction skill and moisture-gradient bias among the S2S models (Fig. 6.7). In Fig. 6.7, the reforecasts initialized in initial MJO phase 2-3 (Figs. 6.7a, c) and 6-7 (Figs. 6.7b, d) with a minimum amplitude of 1.0 are used. For the reforecasts with initial MJO phase 2-3, a scalar metric of zonal moisture gradient is computed by taking the difference between the area-averaged CWV in the western Maritime Continent (100°E-120°E, 10°S-10°N) and that of the eastern Indian Ocean (60°E-80°E, 10°S-10°N). The meridional moisture gradient is defined by the difference between the area-averaged CWV over the equatorial (60°E-120°E, 5°S-5°N) and subtropical (60°E-120°E, 25°S-20°S and 60°E-120°E, 15°N-20°N) regions. For the reforecasts with initial MJO phase 6-7, slightly different domains are used when computing the zonal and meridional moisture gradients. Specifically,

the zonal gradient is defined by taking the difference between the central Pacific (170°E-190°E, 10°S-10°N) and the Maritime Continent (110°E-130°E, 10°S-10°N), whereas the meridional gradient is quantified by the difference between the equatorial (110°E-170°E, 10°S-5°S) and subtropical (110°E-170°E, 35°S-30°S and 110°E-170°E, 10°N-15°N) regions.

It is evident from Fig. 6.7 that the BCOR skills are closely related with the horizontal moisture gradient biases. The ECMWF model, which shows the highest prediction skill of MJO phase 2-3 (40-day BCOR skill; Table 6.1) has the smallest moisture gradient biases, whereas the JMA model with a prediction skill of only 17 days (Table 6.1), shows the largest moisture gradient biases. Note that the meridional moisture gradients have a higher correlation with MJO prediction skill than zonal moisture gradients (compare correlation coefficients in Fig. 6.7a and those in Fig. 6.7c). This result partly explains the different MJO prediction skills among the BoM, CMA, CNRM, and ECCC models which have similar zonal moisture gradient biases. As shown in Figs. 6.7b, d, essentially the same result is found for MJO phase 6-7. One difference from MJO phase 2-3 is that the BCOR skills are more closely related with the zonal moisture gradient biases than the meridional moisture gradient biases (compare Figs. 6.7b, d). These results presented in Fig. 6.7 are only weakly sensitive to the domain used to calculate the zonal and meridional moisture gradients.

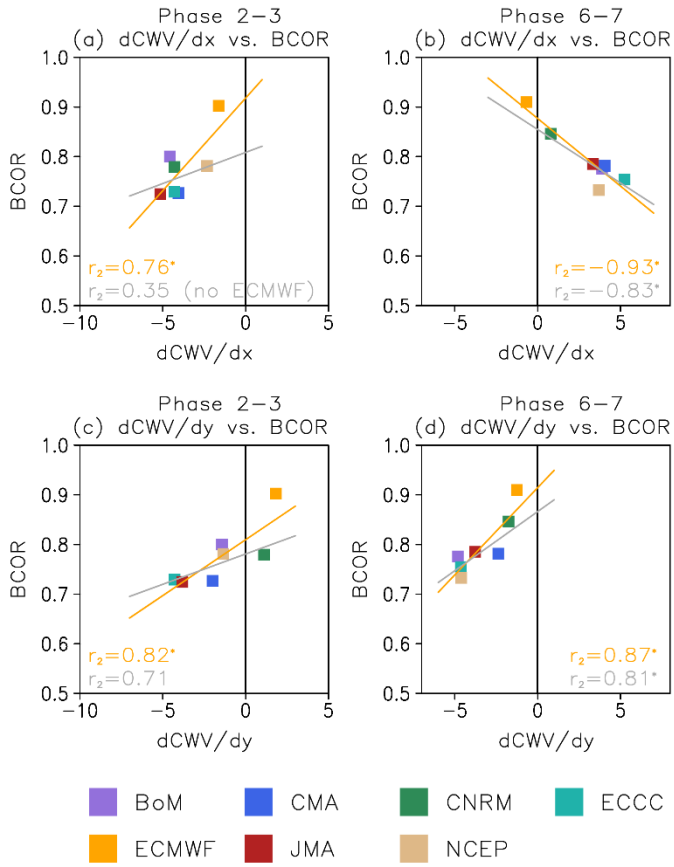

Figure 6.7. Relationship between the model mean biases in moisture gradient and the BCOR skills in the two-week forecast: (a, b) the zonal-moisture-gradient biases versus BCORs for the reforecasts initialized in MJO phase 2-3 and MJO phase 6-7, and (c-d) same with (a-b) but for the meridional-moisture-gradient biases. See the text for the definition of zonal and meridional moisture gradients. The correlation coefficient, r_2, that is statistically significant at the 95% confidence level, is denoted by an asterisk. The regression line is also added. The gray r_2 and the gray regression line indicate the analysis result without the ECMWF model.

The above analyses are repeated for the four-week forecasts (not shown). As anticipated, the linear relationship becomes weaker. For instance, the correlation of BCOR skills to the zonal moisture gradient biases is lowered from 0.76 in the two-week forecasts (Fig. 6.7a) to 0.57 in the four-week forecasts. None of the four-week correlations are statistically significant. It is however important to note that a qualitative similar relationship still holds even in the four-week forecasts. It is worthwhile to note that the correlation coefficients become lower when the ECMWF model is excluded (see gray lines in Figs. 6.7 and 6.9). This suggests that a larger number of models would be useful to better understand the factors that influence MJO prediction skills in operational models.

6.3.2. Cloud-longwave radiation feedback

Next, we examine the relationship between MJO prediction skill and model biases in the CLW feedbacks. The strength of the observed CLW feedbacks is presented in Fig. 6.8a. Here, the CLW feedbacks are quantified by regressing OLR anomalies against precipitation anomalies (both in unit of W m^{-2}) and then multiplying -1 to the resulting regression coefficients (Lin and Mapes 2004). To isolate the MJO-related feedbacks, both OLR and precipitation anomalies are obtained by subtracting the daily climatology and the mean of 120-day segment that ends on the day of interest. The resulting

values (Fig. 6.8a) indicate the ratio of anomalous longwave heating rate to anomalous condensational heating rate in the column.

Figures 6.8b-h show that the S2S models have a wide spread in their representation of the CLW feedbacks, possibly suggesting an important role of physical parameterizations (e.g., cloud microphysics, radiation). Although the bias patterns differ substantially among the models, most models exhibit negative biases in the CLW feedbacks over the Indo-Pacific warm pool region (60°E -180°E, 15°S-15°N). An exception is the ECMWF model that shows somewhat stronger CLW feedbacks over the Indian Ocean than their observational counterparts.

Figure 6.9 shows that MJO prediction skill is tightly linked to the CLW feedback bias. Here the CLW feedback bias is averaged over the Indo-Pacific warm pool region by only considering the oceanic grid points. Consistent with Fig. 6.7, only the two-week forecasts, initialized in MJO phase 2-3 or 6-7, are considered. Although not shown, the overall results are not sensitive to the MJO phase. When all MJO events are considered, the correlation coefficient between the MJO prediction skills and CLW feedback biases becomes slightly larger (0.85 for BCOR in Fig. 6.9a).

The above results suggest that the MJO prediction skills in the S2S models are closely related with model biases in the mean state moisture distribution and in the CLW feedbacks. Here it should be stated that the moisture gradient and CLW biases are not independent with each other. They

are physically related through precipitation biases in the Maritime Continent. In fact, the correlation of the zonal moisture gradient biases to the CLW biases is 0.53 for MJO phase 2-3 and -0.78 for MJO phase 6-7. This suggests that the moisture gradient and CLW biases mutually, not independently, influence on the MJO prediction errors.

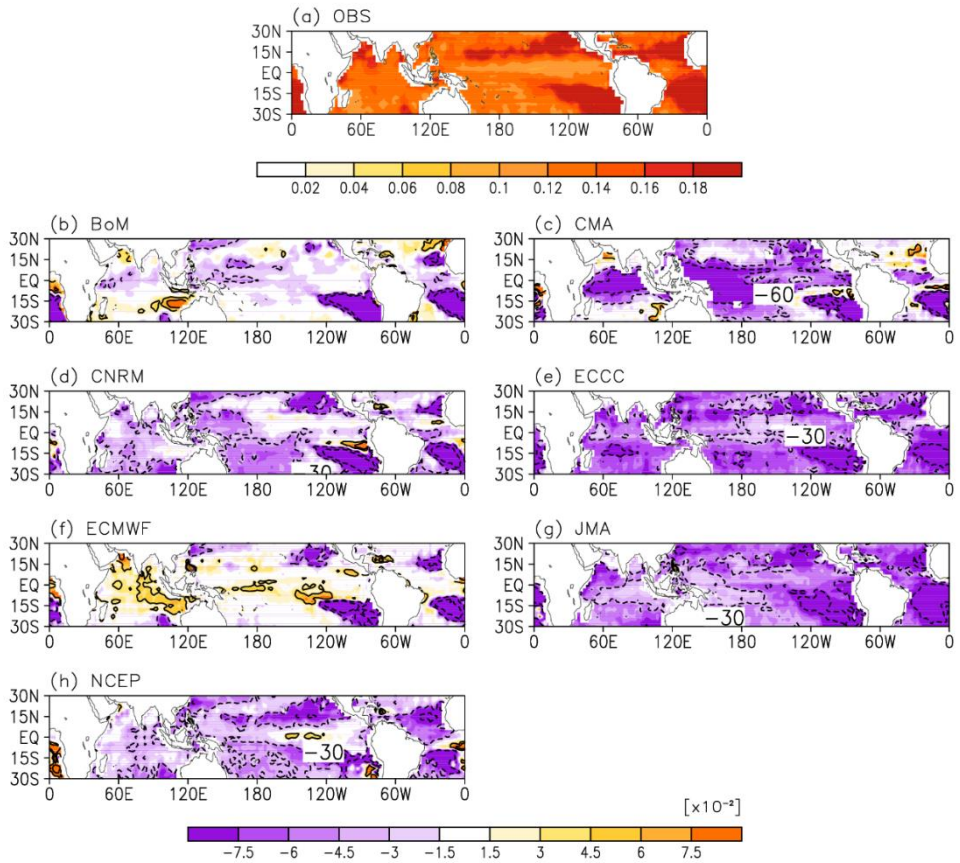

Figure 6.8. (a) Wintertime (NDJFM) average of the CLW feedbacks, and (b-h) the model biases averaged over forecast lead time of 1-30 days. The model biases that are -60, -30, 30, and 30% of the observations are contoured in each panel.

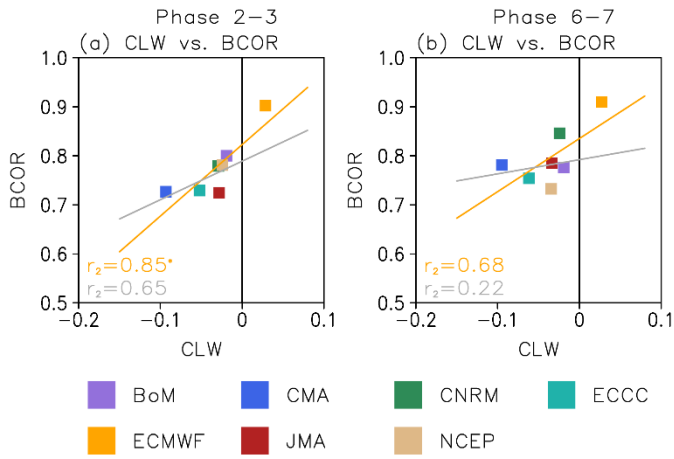

Figure 6.9. Same with Fig. 6.7, but for the relationship between the model biases in the CLW feedbacks and the BCOR skills in the two-week forecast (a) for the reforecasts initialized in MJO phase 2-3 and (b) in MJO phase 6-7. See the text for the definition of CLW feedback biases.

Chapter 7. Summary and discussions

In this thesis, the QBO impacts on the MJO are examined. Figure 7.1 summarizes the key results. Observational study presents the boreal winter MJO is systematically intensified during EQBO (Chap. 2). These QBO-MJO relationship results in the enhancement of the MJO-induced teleconnection during EQBO winters. Due to the short analysis period of the observation, various model data are used to evaluate and understand the QBO-MJO connection. Among current climate models, only one model simulates a weak QBO-MJO connection (Chap. 3). A weaker MJO activity during EQBO winters is presented with partly reproducing the QBO-induced less stable upper-troposphere and lower stratosphere. In the dynamical core model, it is found that the zonal wind QBO can dynamically change the MJO-related vertical structure, forming a more appropriate structure for developing the MJO (Chap. 4). In S2S models, all models capture the QBO-MJO connection, resulting in a higher MJO prediction skill during EQBO winters (Chap. 5). Above model outputs, however, still show a weaker relationship than the observation. To better simulate the QBO-MJO connection at least in the S2S models, it is found that the improvement of the mean moisture field biases and cloud-radiation feedback biases are important (Chap. 6).

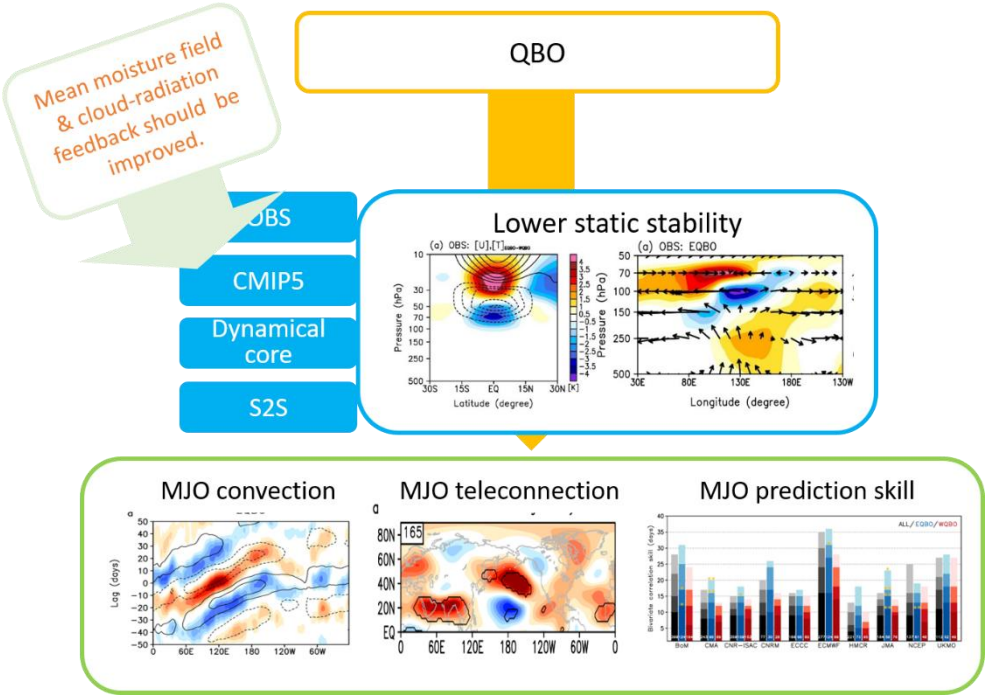

Figure 7.1. Summary of this thesis

For more detail, in the observational analysis (Chap. 2), before understanding the QBO-MJO coupling, the relative importance of ENSO and QBO on the intraseasonal variation of large-scale tropical convection is evaluated. The ENSO also affects the spatial distribution of subseasonal convective activity such as MJO. The MJO activity tends to extend farther into the central Pacific during El Niño winters and the opposite during La Niña winters. However, ENSO does not systematically change overall amplitude of the MJO. The MJO amplitude is instead highly modulated by the QBO. In terms of linear correlation, the QBO explains about 30%–40% of interannual variation of the DJF MJO amplitude. Such a link between QBO

and MJO is also found in other MJO properties (i.e., a stronger amplitude, slower propagation, and longer period of MJO during EQBO winters). The MJO-induced teleconnections are also more pronounced during EQBO winters.

This QBO-MJO relationship is revisited in the four CMIP5 models internally generating the QBO, since there is a big advantage to understand the phenomena due to its long-term dataset (Chap. 3). Three models do not show any hint of the QBO-MJO connection because of either unrealistic QBO or unrealistic MJO in the models. The only model that shows the QBO-MJO connection is the MPI-ESM-MR. This model, which qualitatively well simulates both the QBO and MJO, shows stronger MJO anomalies during the easterly QBO phase than during the westerly phase. However, the modeled QBO-MJO connection is weaker than the observation and is only significant in the western Pacific.

There are several possible reasons why a climate model fails to reproduce or underestimate the QBO-MJO connection. Firstly, the modeled QBO is weaker and narrower than the observation even in the best model. If the modeled QBO is as strong as in the observation, the QBO-MJO connection might be better captured. In this regard, a higher vertical resolution and more physically constraint gravity wave parameterization would be helpful (e.g., Schmidt et al. 2013; Geller et al. 2016). By integrating cloud resolving model, Martin et al. (2019) showed that the QBO-MJO

connection depends on the vertical location and amplitude of the UTLS temperature anomaly. The coupled chemistry model, which allows ozone transport, will help to better simulate the realistic QBO-related temperature anomalies in the lower stratosphere. Secondly, the MJO convection itself is not well organized in many models. Since the QBO may regulate only organized deep convection (Collimore et al., 2003), the less organized MJO convection might be only weakly affected by the QBO. Thirdly, the QBO-related temperature and static stability changes in the lower stratosphere are significantly underestimated in the model. More realistic cold cap simulation would be also helpful for the simulation of more realistic QBO-MJO connection (Hendon and Abhik, 2018). Hendon and Abhik (2018) proposed that the overriding cold cap induced by the enhanced convection may influence the MJO convection. Lastly, other physical and dynamical processes responsible for the QBO-MJO connection, that are not yet identified, may not work in the model.

Based on the dynamical core model, it is found that the QBO can directly change the MJO-related vertical structure. The MJO-induced cold anomaly near the tropopause becomes colder in the EQBO-like background state. The opposite is also captured in the WQBO-like background state. This result seems to be related to the Doppler shift effect by the QBO-related zonal wind, emphasizing the potential impact of the dynamical process on the QBO-MJO connection.

Although the cold cap structure in the UTLS has been emphasized as an important factor for the QBO-MJO connection, the feedback processes are not yet understood. Compared to the observation and more complicated models (Fig. 5.8), the difference of cold cap amplitude is still weaker in the model. The more extended cold cap structures, mentioned in Hendon and Abhik (2018), are not captured in the idealized model experiment (Fig. 4.3). In terms of the possible impact of the cirrus clouds (Virts et al. 2010; Son et al 2017; Tseng and Fu 2017), the radiative process may affect the feedback process. To understand their interaction between dynamic and physical processes, the thermodynamic budget analysis might be useful in the future study.

In S2S models, the QBO-MJO connection is also examined (Chap. 5). Since the QBO is an interannual variability, and the S2S models are initialized by the reanalysis data, these models have a big advantage of better simulating the QBO rather than the climate models and the dry dynamic core. Also, in terms of the application, the impact of the QBO on MJO prediction skill can be analyzed. All models show an enhanced MJO prediction skill during EQBO winters than during WQBO winters by 1-10 days, confirming the result of Marshall et al. (2017). Although the enhanced MJO prediction skill might be simply caused by stronger MJOs during EQBO winters, the overall result does not change when only MJO events with the similar initial amplitudes are examined. Instead, the difference in prediction skill is partly

associated with varying MJO persistence by the QBO (Marshall et al. 2017). The MJOs in WQBO winters are often rapidly disorganized within a few weeks. This breakdown of MJO is not well captured by the S2S models, reducing the theoretical limit of MJO prediction. It is however unclear why the observed MJO is less persistent during WQBO winters.

The EQBO-WQBO MJO prediction skill difference could be also influenced by the model deficiency. Although all models show systematically higher MJO prediction skills during EQBO winters, their differences from WQBO winters vary widely among the models. Such an inter-model difference could be associated with the model deficiency. The S2S models mostly exhibit pronounced dry biases around the Maritime Continent, and underestimate the CLW feedbacks (Chap. 6). The former results in a weak horizontal moisture gradient over the Indian Ocean and the western Pacific, which would weaken MJO organization and propagation. These results show that the model with a larger moisture gradient bias has lower MJO prediction skill. Likewise, the model with a larger bias in CLW feedbacks has relatively low prediction skill. These results suggest that MJO prediction skill could be improved by correcting these model biases, and thus the QBO-MJO connection can be better simulated. Modeling studies with varying cloud parameterizations or radiation schemes could also be useful.

References

Adames, Á. F., and J. M. Wallace, 2015: Three-dimensional structure and evolution of the moisture field in the MJO. *J. Atmos. Sci.*, **72**, 3733-3754.

Adames, Á. F., and D. Kim, 2016: The MJO as a dispersive, convectively coupled moisture wave: Theory and observations. *J. Atmos. Sci.*, **73**, 913-941.

Ahn, M.-S., and Coauthors, 2017: MJO simulation in CMIP5 climate models: MJO skill metrics and process-oriented diagnosis. *Climate Dyn.*, **49**, 4023-4045.

Andersen, J. A., and Z. Kuang, 2012: Moist static energy budget of MJO-like disturbances in the atmosphere of a zonally symmetric aquaplanet. *J. Climate*, **25**, 2782-2804.

Andrews, D. G., J. R. Holtin, and C. B. Leovy, 1987: Middle Atmosphere Dynamics. *International Geophysics Series*, **40**, Academic Press, 489pp.

Anthes, R. A., and Coauthors, 2008: The COSMIC/FORMOSAT-3 mission: Early results. *Bull. Amer. Meteor. Soc.,* **89**, 313-333.

Baggett, C. F., E. A. Barnes, E. D. Maloney, and B. D. Mundhenk, 2017: Advancing atmospheric river forecasts into subseasonal-to-seasonal time scales. *Geophys. Res. Lett.*, **44**, 7528-7536.

Baldwin, M. P., and Coauthors, 2001: The quasi-biennial oscillation. *Rev. Geophys.*, **39**, 179–229.

Bretherton, C. S., J. R.McCaa, and H. Grenier, 2004: A new parameterization for shallow cumulus convection and its application to marine subtropical cloud-topped boundary layers. Part I: Description and 1D results. *Mon. Wea. Rev.*, **132**, 864-882.

Butchart, N., A. A. Scaife, J. Austin, S. H. E. Hare, and J. R. Knight, 2003: Quasi-biennial oscillation in ozone in a coupled chemistry-climate model. *J. Geophys. Res.*, **108**, 4486.

Butchart, N., and Coauthors, 2018: Overview of experiment design and comparison of models participating in phase 1 of the SPARC Quasi-Biennial Oscillation initiative (QBOi). *Geosci. Mod. Dev.*, **11**, 1009-1032.

Cassou, C., 2008: Intraseasonal interaction between the Madden-Julian Oscillation and the North Atlantic Oscillation. *Nature*, **455**, 523-527.

Chang, C. -P., 1977: Viscous internal gravity waves and low-frequency oscillations in the tropics. *J. Atmos. Sci.*, **34**, 901–910.

Charney, J. G., 1963: A note on large-scale motions in the tropics, *J. Atmos. Sci.*, **20**, 607-609.

Chikira, M., 2014: Eastward-propagating intraseasonal oscillation represented by Chikira-Sugiyama cumulus parameterization. Part II: Understanding moisture variation under weak temperature gradient balance. *J. Atmos. Sci.*, **71**, 615-639.

Collimore, C. C., D. W. Martin, M. H. Hitchman, A. Huesmann, and D. E. Waliser, 2003: On the relationship between the QBO and tropical deep convection. *J. Climate*, **16**, 2552–2568.

Dee, D. P., and Coauthors, 2011: The ERA-Interim reanalysis: Configuration and performance of the data assimilation system. *Quart. J. Roy. Meteor. Soc.*, **137**, 553-597.

Durre, I., R. S. Vose, and D. B. Wuertz, 2006: Overview of the Integrated Global Radiosonde Archive. *J. Climate*, **19**, 53–68.

Feldstein, S. B., 1994: A weakly nonlinear primitive equation baroclinic life cycle. *J. Atmos. Sci.*, **51**, 23-34.

Feng, J., P. Liu, W. Chen, and X. Wang, 2015: Contrasting Madden–Julian oscillation activity during various stages of EP and CP El Niños. *Atmos. Sci. Lett.*, **16**, 32–37.

Flatau, M., P. J. Flatau, P. Phoebus, and P. P. Niiler, 1997: The feedback between equatorial convection and local radiative and evaporative processes: The implications for intraseasonal oscillations. *J. Atmos. Sci.*, **54**, 2373–2386.

Franzke, C., S. Lee, and S. B. Feldstein, 2004: Is the North Atlantic Oscillation a breaking wave? *J. Atmos. Sci.*, **61**, 145-160.

Fuchs, Ž., and D. J. Raymond, 2017: A simple model of intraseasonal oscillations. *J. Adv. Model. Earth Syst.,* **9**, 1195-1211.

Garfinkel, C. I., S. B. Feldstein, D. W. Waugh, C. Yoo, and S. Lee, 2012: Observed connection between stratospheric sudden warmings and the Madden–Julian oscillation. *Geophys. Res. Lett.*, **39**, L18807.

Geller, M. A., and Coauthors, 2016: Modeling the QBO-Improvements resulting from higher model vertical resolution, *J. Adv. Model. Earth Syst.*, **8**, 1092-1105.

Giorgetta, M. A., L. Bengtsson, and K. Arpe, 1999: An investigation of QBO signals in the East Asian and Indian monsoon in GCM experiments. *Climate Dyn.*, **15**, 435–450.

Gonzalez, A. O., and X. Jiang, 2017: Winter mean lower tropospheric moisture over the Maritime Continent as a climate model diagnostic metric for the propagation of the Madden-Julian Oscillation. *Geophys. Res. Lett.*, **44**, 2588-2596.

Gottschalck, J., and Coauthors, 2010: A framework for assessing operational Madden-Julian Oscillation forecasts: A CLIVAR MJO working group project. *Bull. Amer. Meteor. Soc.,* **91**, 1247-1258.

Gray, W. M., J. D. Sheaffer, and J. A. Knaff, 1992: Hypothesized mechanism for stratospheric QBO influence on ENSO variability. *Geophys. Res. Lett.*, **19**, 107–110.

Gualdi, S., A. Navarra, and G. Tinarelli, 1999: The interannual variability of the Madden–Julian oscillation in an ensemble of GCM simulations. *Climate Dyn.*, **15**, 643–658.

Gushchina, D., and B. Dewitte, 2012: Intraseasonal tropical atmospheric variability associated with the two flavors of El Niño. *Mon. Wea. Rev.*, **140**, 3669–3681.

Hall, J. D., A. J. Matthews, and D. J. Karoly, 2001: The modulation of tropical cyclone activity in the Australian region by the Madden–Julian Oscillation. *Mon. Wea. Rev.*, **129**, 2970-2982.

Hartmann, D. L., J. R. Holton, and Q. Fu, 2001: The heat balance of the tropical tropopause, cirrus, and stratospheric dehydration. *Geophy. Res. Lett.,* **28**, 1969–1972.

Henderson, S. A., E. D., Maloney, and S.-W., Son, 2016: Madden-Julian Oscillation Pacific teleconnections: The impact of the basic state and MJO representation in general circulation models. *J. Climate*, **30**, 4567–4587.

Hendon, H. H. and S. Abhik, 2018: Differences in vertical structure of the Madden-Julian Oscillation associated with the Quasi-Biennial Oscillation. *Geophys. Res. Lett.*, **45**, 4419-4428.

Hendon, H. H., and B. Liebmann, 1990: A composite study of onset of the Australian summer monsoon. *J. Atmos. Sci.*, **47**, 2227-2250.

Hendon, H. H., M. C. Wheeler, and C. Zhang, 2007: Seasonal dependence of the MJO–ENSO relationship. *J. Climate*, **20**, 531–543.

Hendon, H. H., C. Zhang, and J. D. Glick, 1999: Interannual variation of the Madden–Julian oscillation during austral summer. *J. Climate*, **12**, 2538–2550.

Ho, C.-H., H.-S. Kim, J.-H. Jeong, and S.-W. Son, 2009: Influence of stratospheric quasi-biennial oscillation on tropical cyclone tracks in western North Pacific. *Geophys. Res. Lett.*, **36**, L06702.

Holloway, C. E., and J. D. Neelin, 2007: The convective cold top and quasi equilibrium. *J. Atmos. Sci.*, **64**, 1467-1487.

Holton, J. R., and H. C. Tan, 1980: The influence of the equatorial quasi biennial oscillation on the global circulation at 50mb. *J. Atmos. Sci.*, **37**, 2200–2208.

Hong, Y., G., Liu, and J.-L. F. Li, 2016: Assessing the radiative effects of global ice clouds based on CloudSat and CALIPSO measurements. *J. Climate*, **29**, 7651–7674.

Hou, A. Y., S. Q. Zhang, A. M. da Silva, W. S. Olson, C. D. Kummerow, and J. Simpson, 2001: Improving global analysis and short–range forecast using rainfall and moisture observations derived from TRMM and SSM/I passive microwave sensors. *Bull. Amer. Meteor. Soc.*, **82**, 659–679.

Huang, B., and Coauthors, 2016: Further exploring and quantifying uncertainties for Extended Reconstructed Sea Surface Temperature (ERSST) version 4 (v4). *J. Climate*, **29**, 3119–3142.

Huang, B., and Coauthors, 2017: Extended Reconstructed Sea Surface Temperature version 5 (ERSSTv5), Upgrades, validations, and intercomparisons. *J. Climate*, 30, 8179–8205.

Huffman, G. J., R. F. Adler, M. M. Morrissey, D. T. Bolvin, S. Curtis, R. Joyce, B. McGavock, and J. Susskind, 2001: Global precipitation at one-degree daily resolution from multisatellite observations. *J. Hydrometeor.*, **2**, 36–50.

Inoue, M., M. Takahashi, and H. Naoe, 2011: Relationship between the stratospheric quasi-biennial oscillation and tropospheric circulation in northern autumn. *J. Geophys. Res.*, **116**, D24115.

Janiga, M. A., and C. Zhang, 2016: MJO moisture budget during DYNAMO in a cloud-resolving model. *J. Atmos. Sci.*, **73**, 2257-2278.

Jeong, J.-H., C.-H. Ho, B.-M. Kim, and W.-T. Kwon, 2005: Influence of the Madden-Julian Oscillation on wintertime surface air temperature and cold surges in east Asia. *J. Geophys. Res. Atmos.*, **110**, D11104.

Kang, I. -S., F. Liu, M. -S. Ahn, Y. -M. Yang, and B. Wang, 2013: The role of SST structure in convectively coupled Kelvin–Rossby waves and its implications for MJO formation. *J. Climate*, **26**, 5915–5930.

Kiladis, G. N., K. H. Straub, and P. T. Haertel, 2005: Zonal and vertical structure of the Madden-Julian Oscillation. *J. Atmos. Sci.*, **62**, 2790-2809.

Kiladis, G. N., K. H. Straub, G. C. Reid, and K. S. Gage, 2001: Aspects of interannual and intraseasonal variability of the tropopause and lower stratosphere. *Quart. J. Roy. Meteor. Soc.*, **127**, 1961-1983.

Kiladis, G. N., and Coauthors, 2014: A comparison of OLR and circulation-based indices for tracking the MJO. *Mon. Wea. Rev.*, **142**, 1697–1715.

Kim, D., M.-S. Ahn, I.-S. Kang, and A. D. Del Genio, 2015: Role of longwave cloud-radiation feedback in the simulation of the Madden-Julian Oscillation. *J. Climate*, **28**, 6979-6994.

Kim, J., and S.-W. Son, 2012: Tropical cold-point tropopause: Climatology, seasonal cycle, and intraseasonal variability derived from COSMIC GPS radio occultation measurements. *J. Climate*, **25**, 5343–5360.

Kim, J., K. M. Grise, and S.-W. Son, 2013a: Thermal characteristics of the cold-point tropopause region in CMIP5 models, *J. Geophys. Res. Atmos.*, 118, 8827-8841.

Kim, H.-K., and S. Lee, 2001: Hadley cell dynamics in a primitive equation model. Part I. Axisymmetric flow. *J. Atmos. Sci.*, **58**, 2845-2458.

Kim, H.-M., 2017: The impact of the mean moisture bias on the key physics of MJO propagation in the ECMWF reforecast. *J. Geophys. Res. Atmos.*, **122**, 7772-7784.

Kim, H.-M., P. J. Webster, V. E. Toma, and D. Kim, 2014: Predictability and prediction skill of the MJO in two operational forecasting systems. *J. Climate*, **27**, 5364-5378.

Kim, H.-M., D. Kim, F. Vitart, V. E. Toma, J.-S. Kug, and P. J. Webster, 2016: MJO propagation across the Maritime Continent in the ECMWF ensemble prediction system. *J. Climate*, **29**, 3973-3988.

Kim, Y.-H., A. C. Bushell, D. R. Jackson, and H.-Y. Chun, 2013b: Impacts of introducing a convective gravity-wave parameterization upon the QBO in the Met Office Unified Model. *Geophys. Res. Lett.*, **40**, 1873–1877.

Kiranmayi, L., and E. D. Maloney, 2011: Intraseasonal moist static energy budget in reanalysis data. *J. Geophys. Res. Atmos.*, **116**, D2116.

Lavender, S. L., and A. J. Matthews, 2009: Response of the West African monsoon to the Madden–Julian Oscillation. *J. Climate*, **22**, 4097-4116.

Lee, J. C. K., and N. P. Klingaman, 2018: The effect of the quasi-biennial oscillation

on the Madden-Julian oscillation in the Met Office Unified Model Global Ocean Mixed Layer configuration. *Atmos. Sci. Lett.*, **19**, e816.

Li, D., K. P. Shine, and L. J. Gray, 1995: The role of ozone-induced heating anomalies in the quasi-biennial oscillation, *Quart. J. Roy. Meteor. Soc.*, **121**, 937–943.

Liebmann, B., and C. A. Smith, 1996: Description of a complete (interpolated) outgoing long-wave radiation dataset. *Bull. Amer. Meteor. Soc.*, **77**, 1275–1277.

Liess, S., and M. A. Geller, 2012: On the relationship between QBO and distribution of tropical deep convection. *J. Geophys. Res.*, **117**, D03108.

Lim, Y., and S.-W. Son, 2020: A weak QBO-MJO connection in CMIP5 models, *in revision*.

Lim, Y., S.-W. Son, and D. Kim, 2018: MJO prediction skill of the subseasonal-to-seasonal models, *J. Climate*, **31**, 4075–4094.

Lim, Y. S.-W. Son, A. G. Marshall, H. H. Hendon, and K.-H. Seo, 2019: Influence of the QBO on MJO prediction skill in the subseasonal-to-seasonal prediction models, *Climate Dyn.*, **53**, 1681-1695.

Lin, H., and G. Brunet, 2011: Impact of the North Atlantic Oscillation on the forecast skill of the Madden-Julian Oscillation. *Geophys. Res. Lett.*, **38**, L02802.

Lin, H., G. Brunet, and J. Derome, 2008: Forecast skill of the Madden–Julian Oscillation in two Canadian atmospheric models. *Mon. Wea. Rev.*, **136**, 4130-4149.

Lin, H., G. Brunet, and J. Derome, 2009: An observed connection between the North Atlantic Oscillation and the Madden–Julian oscillation. *J. Climate*, **22**, 364–380.

Lin, J.-L., and B. E. Mapes, 2004: Radiation budget of the tropical intraseasonal oscillation. *J. Atmos. Sci.*, **61**, 2050-2062.

Liu, C., B. Tian, K.-F. Li, G. L. Manney, N. J. Livesey, Y. L. Yung, and D. E. Waliser, 2014: Northern Hemisphere mid-winter vortex-displacement and vortex-split stratospheric sudden warmings: Influence of the Madden–Julian oscillation and quasi-biennial oscillation. *J. Geophys. Res.*, **119**, 12599-12620.

Liu, X., and Coauthors, 2017: MJO prediction using the sub-seasonal to seasonal forecast model Beijing Climate Center. *Climate Dyn.*, **48**, 3283-3307.

Liu, Z., D. Ostrenga, W. Teng, and S. Kempler, 2012: Tropical Rainfall Measuring Mission (TRMM) precipitation data and services for research and applications. *Bull. Amer. Meteor. Soc.*, **93**, 1317–1325.

Madden, R., and P. Julian, 1971: Description of a 40-50 day oscillation in the zonal wind in the tropical pacific. *J. Atmos. Sci.*, **28**, 702-708.

Madden, R., and P. Julian, 1972: Description of global-scale circulation cells in the tropics with a 40-50 day period. *J. Atmos. Sci.*, **29**, 1109-1123.

Majda, A. J., and S. N. Stechmann, 2009: The skeleton of tropical intraseasonal oscillations. *Proc. Natl. Acad. Sci.*, **106**, 8417–8422.

Marshall, A. G., H. H. Hendon, S.-W. Son, and Y. Lim, 2017: Impact of the quasi-biennial oscillation on predictability of the Madden–Julian oscillation. *Climate Dyn.*, **49**, 1365-1377.

Martin, D. W., C. C. Collimore, and M. H. Hitchman, 2004: El Niño and La Niña in highly reflective cloud. *J. Climate*, **17**, 3470–3475.

Martin, Z., S. Wang, J. Nie, and A. Sobel, 2019: The impact of the QBO on MJO convection in cloud-resolving simulations. *J. Atmos. Sci.*, **76**, 669–688.

Matthews, A. J., B. J. Hoskins, and M. Masutani, 2004: The global response to tropical heating in the Madden-Julian Oscillation during the northern winter. *Quart. J. Roy. Meteor. Soc.*, **130**, 1991-2011.

Moon, J. -Y., B. Wang, and K. –J. Ha, 2011: ENSO regulation of MJO teleconnection. *Climate Dyn.*, **37**, 1133–1149.

Nakazawa, T., 1988: Tropical super clusters within intraseasonal variations over the western Pacific. *J. Meteor. Soc. Japan*, **66**, 823-839.

Naujokat, B., 1986: An update of the observed quasi-biennial oscillation of the stratospheric winds over the tropics. *J. Atmos. Sci.*, **43**, 1873–1877.

Neelin, J. D., and J.-Y. Yu, 1994: Modes of tropical variability under convective adjustment and the Madden-Julian Oscillation. Part I: Analytical theory. *J. Atmos. Sci.*, **51**, 1876-1894.

Neena, J. M., J. Y. Lee, D. Waliser, B. Wang, and X. Jiang, 2014: Predictability of the Madden–Julian Oscillation in the intraseasonal variability hindcast experiment (ISVHE), *J. Climate*, **27**, 4531-4543.

Nie, J., and A. H. Sobel, 2015: Responses of tropical deep convection to the QBO: Cloud-resolving simulations. *J. Atmos. Sci.*, **72**, 3625–3638.

Nishimoto, E., and S. Yoden, 2017: Influence of the stratospheric quasibiennial

oscillation on the Madden–Julian oscillation during austral summer. *J. Atmos. Sci.*, **74**, 1105-1125.

Pang, B., Z. Chen, Z. Wen, and R. Lu, 2016: Impacts of two types of El Niño on the MJO during boreal winter. *Adv. Atmos. Sci.*, **33**, 979–986.

Rashid, H. A., H. H. Hendon, M. C. Wheeler, and O. Alves, 2011: Prediction of the Madden–Julian oscillation with the POAMA dynamical prediction system. *Climate Dyn.*, **36**, 649-661.

Raymond, D. J., 2001: A new model of the Madden-Julian Oscillation. *J. Atmos. Sci.*, **58**, 2807-2819.

Reid, G. C., and K. S. Gage, 1985: Interannual variations in the height of the tropical tropopause. *J. Geophys. Res.*, **90**, 5629– 5635.

Ryu, J.-H., S. Lee, and S.-W. Son, 2008: Vertically propagating Kelvin waves and tropical tropopause variability, *J. Atmos. Sci.*, **65**, 1817-1837.

Schenzinger, V., S. Osprey, L. Gray, and N. Butchart, 2017: Defining metrics of the Quasi-Biennial Oscillation in global climate models. *Geosci. Mod. Dev.*, **10**, 2157-2168.

Schmidt, H., and Coauthors, 2013: Response of the middle atmosphere to anthropogenic and natural forcings in the CMIP5 simulations with the Max Planck Institute Earth system model, *J. Adv. Model Earth Syst.*, **5**, 98-116.

Seo, K.-H., and A. Kumar, 2008: The onset and life span of the Madden–Julian oscillation. *Theor. Appl. Climatol.*, **94**, 13–24.

Seo, K.-H., and S.-W. Son, 2012: The global atmospheric circulation response to tropical diabatic heating associated with the Madden–Julian oscillation during northern winter. *J. Atmos. Sci.*, **69**, 79–96.

Sobel, A., and E. Maloney, 2012: An idealized semi-empirical framework for modeling the Madden–Julian Oscillation. *J. Atmos. Sci.*, **69**, 1691-1705.

Sobel, A., and E. Maloney, 2013: Moisture modes and the eastward propagation of the MJO. *J. Atmos. Sci.*, **70**, 187-192.

Sobel, A. H., E. D. Maloney, G. Bellon, and D. M. Frierson, 2010: Surface fluxes and tropical intraseasonal variability: A reassessment. *J. Adv. Model. Earth Syst.*, **2**, 1-22.

Sobel, A. H., J. Nilsson, and L. M. Polvani, 2001: The weak temperature gradient approximation and balanced tropical moisture waves. *J.Atmos. Sci.*, **58**, 3650-3665.

Son, S.-W., and S. Lee, 2005: The response of westerly jets to thermal driving in a primitive equation model. *J. Atmos. Sci.*, **62**, 3741-3757.

Son, S.-W., Y. Lim, C. Yoo, H. H. Hendon, J. Kim, 2017: Stratospheric Control of the Madden–Julian Oscillation. *J. Climate*, **30**, 1909–1922.

Straub, K. H., 2013: MJO initiation in the real-time multivariate MJO index. *J. Climate*, **26**, 1130-1151.

Taylor, K. E., R. J. Stouffer, and G. A. Meehl, 2012: An overview of CMIP5 and the experiment design, *Bull. Amer. Meteor. Soc.*, **93**, 485–498.

Tian, W., M. P. Chipperfield, L. J. Gray, and J. M. Zawodny, 2006: Quasi-biennial oscillation and tracer distributions in a coupled chemistry-climate model, *J. Geophys. Res.,* **111**, D20301.

Tseng, H. H., and Q. Fu, 2017: Temperature control of the variability of tropical tropopause layer cirrus clouds. *J. Geophys. Res.*, **122,** 11062–11075.

Virts, K. S., J. M. Wallace, Q. Fu, and P. Ackerman, 2010: Tropical tropopause transition layer cirrus as represented by CALIPSO lidar observations. *J. Atmos. Sci.,* **67**, 3113-3129.

Vitart, F., 2014: Evolution of ECMWF sub-seasonal forecast skill scores. *Quart. J. Roy. Meteor. Soc.*, **140**, 1889-1899.

Vitart, F., 2017: Madden- Julian Oscillation prediction and teleconnections in the S2S database. *Quart. J. Roy. Meteor. Soc.,* **143**, 2210-2220.

Vitart, F., and F. Molteni, 2010: Simulation of the Madden- Julian Oscillation and its teleconnections in the ECMWF forecast system. *Quart. J. Roy. Meteor. Soc.,* **136**, 842-855.

Vitart, F., and Coauthors, 2017: The Sub-seasonal to Seasonal (S2S) prediction project database. *Bull. Amer. Meteor. Soc.*, **98**, 163-173.

Wang, B., 1988: Dynamics of tropical low-frequency waves: An analysis of the moist Kelvin wave. *J. Atmos. Sci.*, **45**, 2051-2065.

Wang, B., and G. Chen, 2017: A general theoretical framework for understanding essential dynamics of Madden-Julian oscillation. *Climate Dyn.*, **49**, 2309-2328.

Wang, B., and T. Li, 1994: Convective interaction with boundary layer dynamics in the development of a tropical intraseasonal system. *J. Atmos. Sci.*, **51**, 1386-1400.

Wang, B., and X. Xie, 1998: Coupled modes of the warm pool climate system. Part

I: the role of air-sea interaction in maintaining Madden-Julian oscillation. *J. Climate.*, **11**, 2116-2135.

Wang, J., H.-M. Kim, E. K. M. Chang, and S.-W. Son, 2018: Modulation of the MJO and North Pacific Storm Track relationship by the QBO. *J. Geophys. Res.*, **123**, 3976-3992.

Wang, L., T. Li, E. Maloney, and B. Wang, 2017: Fundamental causes of propagating and nonpropagating MJOs in MJOTF/GASS models. *J. Climate*, **30**, 3743-3769.

Wang, W., M.-P. Hung, S. J. Weaver, A. Kumar, and X. Fu, 2014: MJO prediction in the NCEP Climate Forecast System version 2. *Climate Dyn.*, **42**, 2509-2520.

Wentz, F. J., K. A. Hilburn, and D. K. Smith, 2012: Remote Sensing Systems DMSP SSM/I daily environmental suite on 0.25 deg grid, version 7. Remote Sensing Systems.

Wheeler, M. C., and H. H. Hendon, 2004: An all-season real-time multivariate MJO index: Development of an index for monitoring and prediction. *Mon. Wea. Rev.*, **132**, 1917–1932.

Winker, D. M., W. H. Hunt, and M. J. McGill, 2007: Initial performance assessment of CALIOP. *Geophys. Res. Lett.*, **34**, L19803.

Wolding, B. O., E. D. Maloney, and M. Branson, 2016: Vertically resolved weak temperature gradient analysis of the Madden-Julian Oscillation in SP-CESM. *J. Adv. Model, Earth Syst.*, **8**, 1586-1619.

Xiang, B., M. Zhao, X. Jiang, S.-J. Lin, T. Li, X. Fu, and G. Vecchi, 2015: The 3–4-week MJO prediction skill in a GFDL coupled model. *J. Climate*, **28**, 5351-5364.

Yang, Q., Q. Fu, and Y. Hu, 2010: Radiative impacts of clouds in the tropical tropopause layer. *J. Geophys. Res.*, **115**, D00H12.

Yasunari, T., 1979: Cloudiness fluctuations associated with the northern hemisphere summer monsoon. *J. Meteor. Soc. Japan Ser. II*, **57**, 227-242.

Yoo, C., and S.-W. Son, 2016: Modulation of the boreal wintertime Madden–Julian oscillation by the stratospheric quasi-biennial oscillation. *Geophys. Res. Lett.*, **43**, 1392–1398.

Zhang, C., 2005: Madden-Julian Oscillation. *Rev. Geophys.*, **43**, RG2003.

Zhang, C., 2013: Madden–Julian Oscillation: Bridging weather and climate. *Bull. Amer. Meteor. Soc.*, **94**, 1849-1870.

Zhang. C., and B. Zhang, 2018: QBO-MJO connection. *J. Geophys. Res.*, **123**, 2957-2967.

Zhao, C., T. Li, and T. Zhou, 2013: Precursor signals and processes associated with MJO initiation over the tropical Indian Ocean. *J. Climate*, **26**, 291–307.

국문 초록

최근 성층권 준 2 년주기진동이 북반구 겨울철에 매든-줄리안 진동에 영향을 미칠 수 있다는 가능성이 제시된 바 있다. 성층권 준 2 년주기진동이 동풍일 때, 겨울철 매든-줄리안 진동의 대류 활동이 서풍일 때에 비해 활발해지는 경향이 있는데, 이는 최근에 발표된 연구로써 구체적인 현상과 그 원인에 대한 이해가 부족할 뿐만 아니라, 현업 예측 모형의 계절내 시간 규모의 예측성 향상에도 직접적으로 연관되어 있다는 점에서 이 현상을 이해하는 것은 매우 중요하다. 이에 따라, 본 학위논문은 성층권 준 2 년주기진동이 매든-줄리안 진동에 미치는 영향과 그 원인을 다양한 방법을 바탕으로 이해해보고자 하였다.

관측 자료를 바탕으로, 성층권 준 2 년주기진동의 위상에 따라 매든-줄리안 진동의 활동 특성뿐만 아니라 매든-줄리안 진동의 원격 상관성까지 변화하는 것으로 나타났다. 성층권 준 2 년주기진동이 동풍일 때, 단순히 매든-줄리안 진동의 대류 활동 강도뿐만 아니라 대류 활동의 동진 속도가 느려지고 지속기간이 길어지는 경향이 있으며, 더 나아가, 매든-줄리안 진동의 중위도 원격상관성 강도까지 강화시키는 것으로 나타났다. 이러한 성층권 준 2 년주기진동에 따른 매든-줄리안 진동의 체계적인 변화는 현상에 대한 당위성을 높임과 동시에 이에 대한 검증 및 이해의 필요성을 더욱 높였다. 따라서, 다양한 예측 모형을 활용하여 다음과 같이 현상을 이해하고자 하였다.

첫 번째로 성층권 준 2 년주기진동과 매든-줄리안 진동을 직접 모의하는 기후 모형을 이용하여 현상이 존재하는 지 검증해보고자 하였고, 대부분의 모형에서 모의하지 못하였으나, 하나의 기후모형에서 유일하게 관측에 비해서는 약하지만 현상을 모의하였다. 성층권 준 2 년주기진동이 매든-줄리안 진동에 영향을 미칠 수 있는 원인으로 크게 성층권 준 2 년주기진동에 따른 대류권 상부와 성층권 하부 간 동서방향평균 정적 안정도의 변화, 그리고 매든-줄리안 진동의 연직 구조 변화로 인한 정적안정도의 지역적 변화가 주요 원인으로 알려져 있는데, 기후 모형에서 이를 약하지만 모의하는 것으로 나타났고 현상을 모의하는데 기여했을 것으로 추정되었다. 두 번째로는 역학코어모형을 바탕으로 성층권 준 2 년주기진동이 매든-줄리안 진동의 연직 구조 변화에 역학적으로 영향을 미칠 수 있는지 검증해보았고, 정적 안정도 이외에도 다른 역학적 영향 가능성이 있음을 확인하였다. 마지막으로 10 개의 현업 기관 예측 모형을 바탕으로 현상에 대해 검증해본 결과, 현상이 모의될 뿐 아니라 매든-줄리안 진동의 예측성에도 영향을 미치는 것으로 나타났다. 모형에 따라 차이가 있으나, 성층권 준 2 년주기진동이 동풍일 때, 매든-줄리안 진동의 예측성이 1-10 일 더 높은 것으로 확인되었다.

현재까지 여러 모형에서 두 현상의 상관성을 약하게 나타내긴 하였으나, 그럼에도 불구하고 모형에서 성층권 준 2 년주기진동과 매든-줄리안 진동 현상 각각을 모의하는 데 한계가 있기 때문에, 관측에서 나타난 만큼 두 현상의 높은 상관성을 모의하기에는 어려움이 있었다. 이를 향후

개선하기 위한 방안 중 하나로써, 매든-줄리안 진동의 주요 물리 과정을 바탕으로 구름-복사 피드백 작용과 수분의 평균적 공간 분포 모의 능력이 매든-줄리안 진동의 모의에 중요한 것을 확인하였다. 이러한 물리 과정의 모의 능력이 향상된다면, 향후 성층권 준 2 년주기진동과 매든-줄리안 진동의 상관관계를 이해하고 예측성 향상에도 크게 기여할 것으로 기대된다.

감사의 글

드디어 제게도 이 글을 적을 수 있는 날이 왔네요. 연말 시상식 수상 소감처럼 진부하게 적고 싶지 않았는데, 이제 정말 사회에 첫 발을 내딛는다 생각하니, 제가 변하지 않길 바라면서도 아마 오늘이 제 인생에 남은 날 중에서 제가 가장 순수한 날이 아닐까 싶어서요. 이 논문은 운이 좋게도 정말로 많은 분들이 도움을 주신 덕분에 완성된 것이고, 먼 훗날 이 글을 펼쳤을 때 지금의 감사함을 떠올릴 수 있다면, 제가 앞으로 살아갈 날들에 더욱 큰 힘이 되지 않을까 싶어 진부하지만 이렇게 적어봅니다.

가장 먼저, 우리 교수님. 포기하지 않고, 제가 졸업할 수 있게 지원해주시고 지도해주셔서 감사했습니다. 제가 학위 하는 동안 변함없이 인생을 정말 열심히 사는 게 무엇인지, 연구적으로나 인생을 살아가는 데 있어서 항상 모범적인 모습을 직접 보여주셨고, 내공이 부족한 제가 그 모습을 본받으려 하니 힘에 부치긴 했지만, 그 덕에 (아직도 갈 길이 멀었지만) 조금씩 성장해왔고 저는 점점 더 제 자신이 마음에 들게 되었어요. 세상이 요지경인데, 제 지도 교수님을 존경할 수 있어서 너무 좋았고, 그런 분이 제 지도 교수님이라 자랑스럽고, 감사했습니다 (물론 지금도요).

제 학위 때문에 바쁜 시간 내어 지도해주시고 심사해 주신 허창회 교수님, 서경환 교수님, 김혜미 교수님, 김대현 교수님, 유창현 교수님, 그리고 제가 고민이 있을 때 항상 들어주신 김주완 교수님께도 다시 한 번 감사드립니다. 진심으로 항상 제 연구를 함께 고민해주시고 도와주셔서 감사했습니다. 다른 사람들과 일할 때에도 교수님들께서 제게 보여주신 모습 항상 생각하면서, 그들에게 좋은 연구자이자 동료로 성장할 수 있도록 노력하겠습니다.

운 좋게도 정말 많은 분들이 제 학위에 함께 해주었는데요. 저를 너무 잘 알아서 늘 이해해주고, 먼저 챙겨준 제 오랜 친구들인 지훈이, 수정이, 필수, 서연이, 민희, 이주언니, 은동오빠, 친구들이 준 믿음과 사랑 덕분에 보잘 것 없는 박사과정생이었지만 보잘 것 없다 느끼지 못하고, 외로운 줄

모르고 20대를 보냈습니다. 받기만 한 것 같아서 미안하고, 감사합니다.

다들 힘들었을 텐데 내색하지 않고, 학위과정을 버텨준 501A호 식구들. 영찬오빠, 현성오빠, 두성오빠, 형안오빠, 상무오빠, 승언이. 그리고 진우. 제게 버티고 이겨나가는 걸 몸소 보여주시고, 힘들 때 고민을 나눌 수 있는 전우가 되어 주셔서 감사했습니다.

제게 사회 생활을 가르쳐준 주환이, 그리고 어딘가에는 좋은 세상을 만들겠다는 원대한 꿈을 갖고 사는 진실한 사람이 있다는 걸 알려준 여주와 최영돈 교수님께도 감사의 인사를 전합니다. 뒤늦게 좋은 추억 많이 만들어주시고, 뜻깊은 경험들을 할 수 있게 해준 수영 식구들과 오랜 시간 함께 해주시고 응원해주신 뉴폴더 여러분들께도 감사의 인사를 남깁니다. 함께해서 참 즐겁고 행복했습니다.

우리 실험실 식구들. 정말 고마운 일들이 너무나도 많은데, 글자 수 가지고 혹시나 서로 경쟁할 까봐 개별적인 언급은 개인적으로 하겠습니다:) 지도 교수님의 배려로 개성이 강하고 자기애가 높은 게 우리 실험실의 장점이다 보니, 정말 모든 실험실 식구들의 개개인이 가진 눈부신 장점들을 보며 많이 배웠습니다. 고난과 역경에도 그 빛을 잃지 않고 더 멋진 사람으로 앞으로도 제 곁에 함께 있어 주시길 바래요.

마지막으로 우리 가족. 학위과정동안 그간 마음 졸이며 지원해 주시고 지지해준 우리 가족들에게 그간 걱정시켜서 미안하고, 고맙다는 말을 전하고 싶습니다. 아마 아빠의 욕심과 근성이 가득한 유전자와 엄마의 책임감과 전폭적인 지원, 오빠의 장남 부심 덕분에 잘 마칠 수 있었습니다. 든든한 가족이 늘 항상 뒤에 있어서 버텼고, 여유 있지는 않았지만 마음만은 부족함 못 느끼게 키워주신 덕에 성격이 모나지 않아서 그런지, 운이 좋게도 주변에 좋은 분들을 너무 많이 만났고 학위도 잘 마무리 할 수 있었습니다. 다시 한 번 모두에게 감사의 인사를 전합니다.